Tectonic geomorphology of the Liri valley, central Apennines of Italy

Master's thesis in Geodynamics

by Mariia Pihlainen

Institute of Earth Science

Faculty of Mathematics and Natural Sciences

University of Bergen

May 2014

Abstract

This is a detailed study of hillside catchments in the Liri valley, central Apennines of Italy. Various geomorphic parameters extracted from a 20-m digital elevation model (DEM) are used to study the morphology of small drainage basins on two sides of the valley: one side exhibiting a normal fault and the other an old inactive thrust fault, both bounded by major lithological contacts. In addition, the axial Liri river is known to be incising. The area is in a highly unsteady state, therefore, the motivation behind this study is to understand the long-term evolution of channels in a tectonically active non-equilibrium landscape. The objective is to identify patterns and possible variations along strike, and try to point out possible explanations behind these changes. This is done by combining knowledge of the local geology and contrasting it against the theoretical analysis of long profiles.

Based on a method widely used in tectono-geomorphic studies, channel drainage area is extracted from a DEM, and corresponding slopes are calculated along the extracted channel, after which these data are plotted in logarithmic slope-drainage area space, which yields the concavity (and steepness indices). The extracted values are then compared to what other studies have associated similar concavities with.

The results show that the geomorphology is different between the two sides of the valley. The inactive B-side catchments are controlled mainly by lithology, showing low channel concavities (< 0.4) on the hillslopes and changing to a higher concavity where the streams reach the valley bottom sediments, and also exhibit knickpoints at the lithological boundaries. The active Liri fault side catchments seem to be responding more to catchment size: the small catchments exhibit knickpoints at the fault/ lithological boundary and have in general lower concavities, whereas the larger catchments are nonchalant to this contact and exhibit high concavities (>> 0.6). These very high values may be explained by the southern end of the Liri fault being inactive at present or that the slip rate is much lower than suggested.

Acknowledgments

First of all, I would like to thank the University of Bergen for the use of the computer lab and working place, and the group of other Master student's for the countless cups of coffee, laughs and for creating a good atmosphere. A special thanks to Anneleen Greuts for all help and ideas in the process, as well as to Alex Whittaker for introducing the methods and giving access to the data.

I would also like to thank my parents for supporting my decisions – I would not be here without you. A big thanks to Erlend, for showing me just how passionate one can become about learning something new, even if it's maths – and that it's fun! Thanks for being there and listening, and for making sure I get out in the mountains every once in a while.

However, the biggest thanks belongs to the best supervisor in the world. Patience Cowie, thank you for all the inspirational sessions we had along the way, for your *patience*, good humour, and guidance. You really have a special skill to share your knowledge, expertise and compassion with others, making even a young master student's opinions feel equal and appreciated. It has been a real pleasure to be working with you.

Table of Contents

Chapter 1 – Introduction

1.1 Background for the geomorphic studies of fluvial landscapes

In order to understand better the relative importance of tectonics and climate in controlling landscape evolution, a great deal of geomorphological studies have been made that focus on the mechanisms and rates of river incision (e.g. Whipple and Tucker, 1999; Whittaker et al., 2007a). Although rivers occupy a relatively small percentage of the total land area, fluvial channel networks set the base-level in terrestrial non-glaciated environments, and are the main controlling element behind how hillslope processes vary over an area (Burbank et al., 1996). This is why rivers are responsible for controlling the large-scale morphology of a landscape.

Most geomorphic studies start out considering the case of topographic steady state, which is achieved when the erosion rate is in balance with the rock uplift rate. This means that all streams are considered to incise at the same rate as the local uplift is happening, and as a result there is not much change in topographic elevation over the long term. Studies of river channels commonly focus on expressions of fluvial incision models in steady state and the implications of these models for equilibrium river profiles (e.g. Snyder et al., 2000). Hack (1957) was the first to notice how rivers often have a graded profile that shows a power-law relationship between channel slope and drainage area. Based on empirical studies of bedrock channels (Hack, 1957; Flint, 1974), this scaling relation can be represented as

$$S = k_s A^{-\theta} \qquad \text{(Eq. 1)}$$

where S is the local channel slope, A is the upstream contributing drainage area, and k_s and θ are parameters describing the relative steepness and concavity of the channel respectively. Based on the work of Hack (1957) and Flint (1974), graded river profiles have become a fundamental tool used widely in geomorphological analysis especially after digital elevation models (DEMs) allowed easy slope and area data extraction. Illustrations of what different concavities and steepnesses look like on a graded longitudinal profile and slope-area plot are shown in Figure 1.

There are various models for river erosion considering different processes that might effect erosion rate along the channel, but the majority of the publications work with a generalized form of the stream-power erosion law that takes into account empirical relations among discharge, drainage area and channel widths (Howard, 1994; Whipple, 2004):

$$E = KA^mS^n \quad \text{(Eq. 2)}$$

Here erosion rate (E) is a function of drainage area (A), which is also considered as a proxy for discharge, and slope (S), where n and m are positive empirical constants (usually n is 1 and m is 0.5 for rivers), and K is an erodibility constant (e.g. Whipple and Tucker, 1999; Snyder et al., 2000). This stream power-law in Equation 2 is an expression for predicting the rate of channel incision into bedrock for detachment-limited channels. The other end-member would be transport-limited conditions, which are not discussed further in this study.

Application of Equation 2 has been undertaken in landscapes where a balance between erosion and rock uplift seems to be attained (e.g. Snyder et al., 2000; Kirby and Whipple, 2001), but steady state landscapes are actually not that common. Instead, many landscapes are noticed to be in a transient state, meaning they are still adjusting to major changes caused by external factors like climate or tectonic activity.

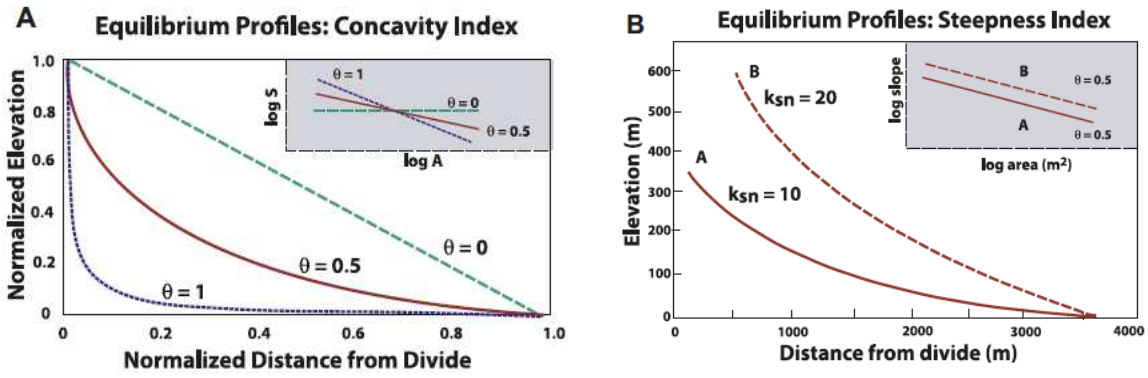

Figure 1. An illustration of channel profile form (from Kirby and Whipple, 2012; modified from Duvall et al., 2004 and Whipple and Tucker, 1999): A is explaining how concavity index (θ) influences profile shape and slope-area scaling (small grey box). B shows how two profiles with the same concavity index can still have different steepness indices (k_{sn}).

Understanding the response of non-equilibrium landscapes to external changes is a hot research topic. In particular, transient river profiles are often reported as proof of a river's response to disturbance with major knickpoints potentially providing evidence for a change in tectonic base-level fall or a change in climate regime (e.g. precipitation), although a clear distinguishion between the two may be a difficult task (Kirby and Whipple, 2012). An example of how a river profile in a transient state might look like, as well as the slope and area data extracted from this profile, are given in Figure 2. Knickpoints similar to those shown in Figure 2 can in some cases relate to changes in the erodability of the bedrock, but with good knowledge of the geology such "lithological knickpoints" can be separated from those associated with transient landscape evolution.

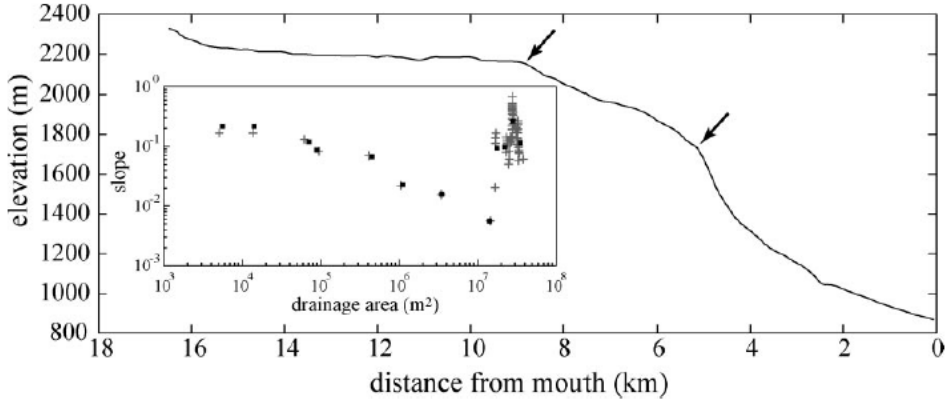

Figure 2. An example of a transient river long profile and its slope vs. drainage area logarithm plot from Ailao Shan, Yunnan, China (Schoenbohm et al., 2004). The arrows are pointing at major knickpoints on the profile.

When considering steep upland valleys, as is done in this study, much of the drainage area is dominated by hillslope processes, not by river channels (Stock and Dietrich, 2003). Stock and Dietrich (2003) combined field evidence with analysis of high-resolution DEMs, and found that erosion on slopes above ~0.10 is often happening by hillslope processes such as debris flows and landslides. They found that up to 80% of mountain valley channel networks are actually dominated by debris flow erosion. Figure 3 illustrates the network pattern of debris flow channels as a time-transgressive cartoon (Stock and Dietrich, 2006). Debris flows play a key role in landscape evolution because they potentially restrict the relief of unglaciated steep mountain ranges to a greater extent than fluvial incision (Whipple, 2004). Because of this, especially in the context of understanding how active tectonics may be affecting the geomorphology of mountainous areas, studying hillslopes can perhaps help with gaining a greater understanding of landscape evolution than what would be achieved by only studying rivers and fully fluvial processes.

Debris flows are still reasonably young field of study. There are various articles that consentrate on debris flows (e.g. Montgomery and Buffington, 1997; Howard, 1998; Stock and Dietrich, 2003 and 2006; Lague and Davy, 2003; Stock et al., 2005; Densmore et al., 2007; Lancaster, 2008). Many of them study the erosional processes of debris flows, flow rheology, sediment transport and deposition, or are trying to understand the mechanics of debris flow incision, and how well the existing fluvial power-laws apply to debris flow channels.

Studies of how debris flows' response to active tectonics are scarce. Stock and Dietrich (2003) studied debris flows in steady state conditions. Densmore et al. (2007) studied debris flow long profiles in the context of active faults in Idaho, western United States, and Lague and Davy (2003) had done the same in Siwaliks Hills, Nepal. Both articles still

concentrate on the assumption of a steady state, except that Densmore et al. (2007) suggested that catchments at fault tips may be in transient state due to fault propagation and linkage.

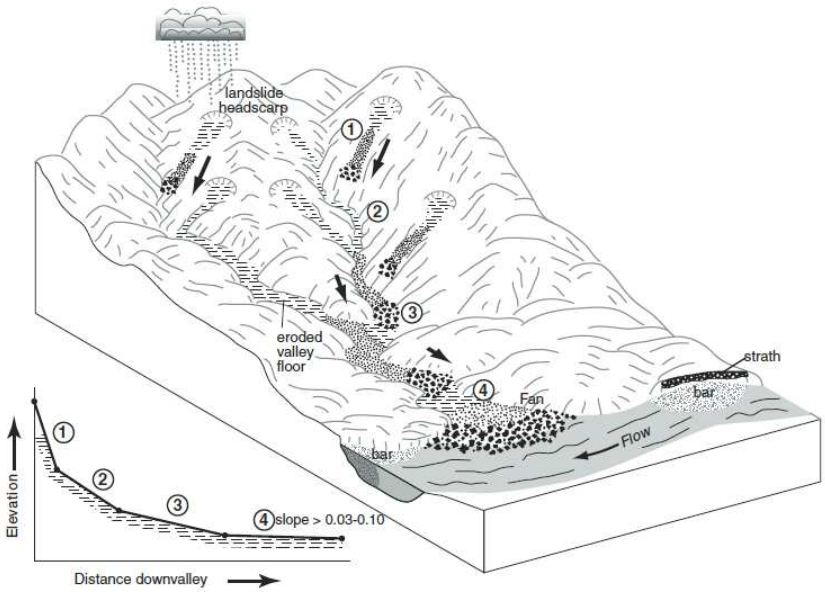

Figure 3. An illustration by Stock and Dietrich (2006) of how debris flows incise steepland valleys, with an explanation of the critical degree of slope above which debris flows are the dominating process. Rainfall triggers single landslides mobilizing debris flows that erode valley floors and gain more material as they move downstream. According to this, fast and frequent flows with granular mouths erode on slopes above 0.03–0.10, below which granular flows are rarely able to move, that marks the transition to fluvially dominated processes.

To obtain information about tectonic impacts on fluvial landscapes, it is vital to understand the erosional characteristics of fluvial systems (Whipple, 2004). Debris flow erosion is observed to be essentially different from fluvial one due to debris flows' sporadic nature (e.g. Howard, 1998; Stock et al., 2005). Unlike rivers, debris flow channels do not have flowing water in them most of the time. The erosion is therefore tightly controlled by short-term pulses of rapid delivery of water mixed with sediments. In some ways, debris flow channels may be characterised as somewhat similar to bedrock rivers as their channels are not composed of transportable sediments along the whole length, but usually exhibit a channel consisting of bare rock instead. However, unlike bedrock rivers, debris flows lack banks and other fluvial features that normally define rivers, and their valleys are often covered by coarse, unsorted material arriving from adjacent hillslopes (Stock and Dietrich, 2003). Davy and Crave (2000) explain that the long-term evolution of a river bed is driven either by detachment-limited or transport-limited conditions, or a mixture of the two. Debris flow catchments appear to exhibit such wide range of processes that influence erosion and deposition in them, from landslide-mobilized hillslope processes to colluvial channels to sometimes being more fluvial in style (Montgomery and Buffington, 1997), that it is hard to point out what

exactly is the dominant process that describes them best as there is uncertainty with understaning in what degree these processes are partitioned in debris flow channels (e.g Howard 1998; Lague and Davy, 2003).

1.2 Application of the power-law to debris flows

Because there are uncertainties in understanding all parameters that might be involved in debris flow erosion, there is also disagreement around what kind of models would be proper to use when studying them. According to some authors (Montgomery and Foufoula-Georgiou., 1993; Sklar and Dietrich, 1998; Snyder et al., 2000; Stock and Dietrich, 2003), the bedrock river incision models (e.g. Equation 2) are not applicable to debris flows because of the clear break in scale in the power-law of slope on the logarithmic plot, an example shown in Figure 4. The change in scaling can be either gradual or very clear: a profile with segments of different values of k_s and θ (or both) occurring over a drainage area that typically varies between 0.1–5 km^2. This scaling break marks a transition from fluvial processes to hillslope or debris flow processes that are claimed to be fundamentally different from those of bedrock rivers, as discussed above. These authors have suggested that for modeling debris flows, a separate model should be used, an example of which is proposed e.g. by Stock and Dietrich (2006).

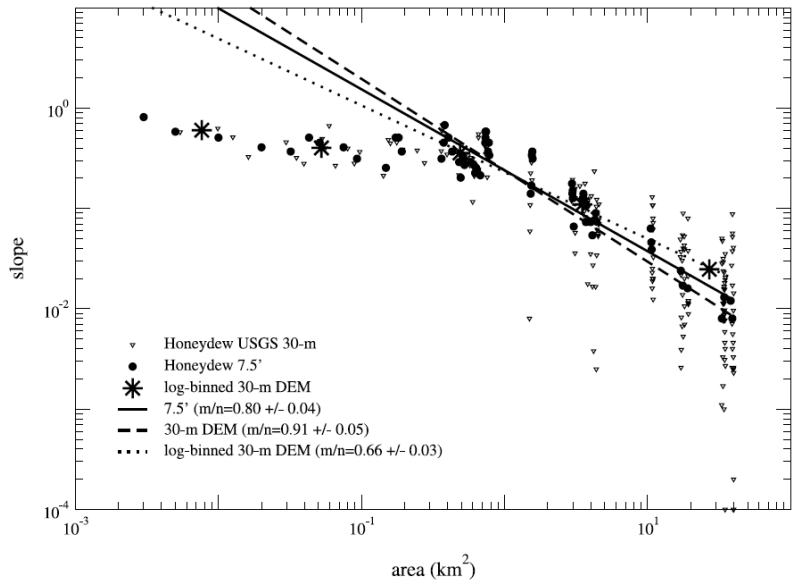

Figure 4. Slope vs. area plot from a river in Honeydew valley, California (Stock and Dietrich, 2003) showing a clear scaling break at ~0.4 km^2, marking a change in power-law from fluvial processes to debris flows.

Other authors have suggested that if valleys modified by debris flows show a curved profile when plotting log-slope against log-drainage area when data is measured from adequately high-resolution DEMs, the stream-power law can be applied to study debris flow valley network the same way as fluvial network (e.g Whipple and Tucker, 1999;

Lague and Davy, 2003). According to this method, the trend above the scaling break follows Equation 1 presenting only a lower concavity.

Whipple and Tucker (2002) tested the slope-area relationship against three different sediment transport conditions, examining them in the light of different dependencies between incision rate and sediment flux. They found that in nearly all of these models the power-law between slope and drainage area predicted by Equation 1 holds true despite the conditions being detachment or transport-limited or a mixture of the two. In this sense the power-law slope-area plot (e.g. Figure 4) can be used as a tool for examining debris flow channels, although the results may indicate a topographic signature that is essentially different than predicted by the river incision models as Snyder et al. (2000) and Stock and Dietrich (2003 and 2006) proposed.

There is still a lot of uncertainties remaining in question about how debris flows should be presented in landscape evolution models; whether some of the debris flow processes are not captured fully by fluvial models and therefore may significantly influence the conclusions (Whipple, 2004; Kirby and Whipple, 2012). Therefore, further analysis of debris flow channels and comparison to fluvial catchments is required.

1.3 Objectives of the project

This study uses a 20-m resolution DEM of the Liri valley in the central Italian Apennines, and tries to resolve how tectonics are affecting geomorphology of hillside catchments in the area. Based on the drainage area and slope measurements alone, catchments in the Liri valley are expected to be dominated by debris flows (drainage area $\leq$ 1-10 km^2). In addition, the area is influenced by active normal-faulting (e.g. Piccardi et al., 1999; Roberts and Michetti, 2004) and Holocene climate change (e.g. Zolitschka and Negendank, 1996; Allen et al., 1999 and 2000), which are also reasons why the Liri valley is interesting.

The project uses the power-law approach (Equation 1), discussed above, to analyse these catchments in a similar way as previous studies have done in different parts of the world, e.g. by Lague and Davy (2003), Schoenbohm et al. (2004), Densmore et al. (2007) or Hobley et al. (2010). The above mentioned papers are examples of tectono-geomorphic studies made on debris flow catchments, or tributary catchments rather than large rivers. This thesis differs from these previous studies by taking place in an area that is known to be in a non-steady state (Whittaker et al., 2007b), and by concentrating on catchments that are mostly quite a lot smaller than studied by these previous authors.

The deeper understanding of debris flow channels in relation to tectonics is still lacking, since there has been relatively little research on them. Therefore, one of the objectives of this study is to cast more light on the characteristics of catchments that can be expected to be dominated by debris flows, comparing catchments that are bounded by a normal fault to ones that do not cross an active fault. The purpose is not to interpret the results in terms of erosion processes in detail, but rather to describe the patterns of the long profiles of these catchments, and reflect the results against what is known from similar studies made on fluvial channels.

More profoundly, the aim of this thesis is to try and find out whether the active Liri fault (discussed in more detail in the next chapters) is affecting the geomorphic processes, and if it is, what is the evidence. Is it related to the segmentation of the fault, or does it vary within the suggested slip rate? This is done by making a detailed comparison with long profiles of adjacent channels in the Liri valley.

1.4 Study area

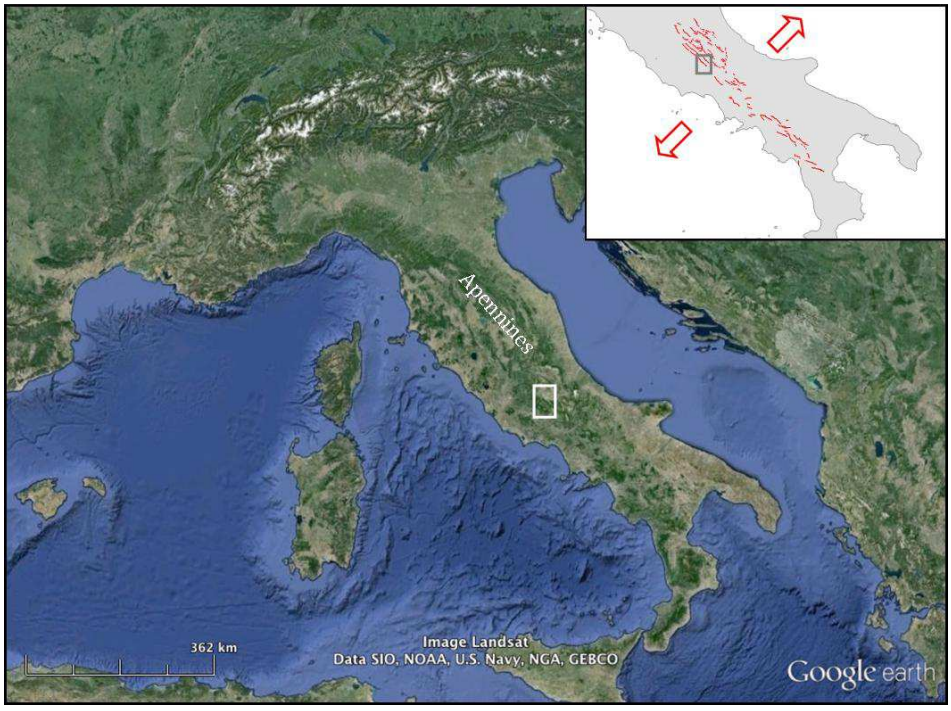

Figure 5. General map of Italy showing the Apennines mountain chain (from Google Earth), and the general tectonics with extensional faults drawn in red (inset). The small boxes indicate the location of the study area.

The locality examined in this study is situated on the border between the provinces of Lazio and Abruzzo, central Apennines (Figure 5). It is an area of high mountains with elevations reaching above 2000 m, and intersecting valleys with mean bottom elevations around 500 m. Italy is an ideal place for examining geomorphological processes in relation to tectonics, because the long-term displacement rates are well documented (Roberts and Michetti, 2004).

In the next few pages, the tectonic settings and geology of the western Mediterranean, and more closely the central Apennines will be discussed. The main study locality, Liri valley, will also be introduced in this context.

1.4.1 General tectonic setting

The geodynamic evolution of the Mediterranean region is complex. Although it is generally accepted that the Mediterranean geology has been shaped by the interplay between the African and Eurasian plates, reconstructions are not easy due to number of intervening microplates involved and complicated tectonic patterns creating a jig-saw puzzle that is still debated in many parts.

In a larger context, the area of interest in this study is located in the western Mediterranean. The commonly accepted model that resulted in the present structures in this region (established by the geophysical studies of Malinverno and Ryan, 1986; Patacca et al., 1990; Doglioni 1995; Gueguen et al., 1998) is the opening of the Tyrrhenian Sea and the contemporary eastwards retreating migration of the westward-directed Apenninic subduction zone since the Late Cenozoic. The extension that is characteristic of most of the western Medritterranean seems to contradict the context of relative convergence between Africa and Europe. However, the relative N-S motion between Africa and Europe appears to be much slower compared to the migration of the Apenninic arc towards the east (Patacca et al., 1990; Lavecchia et al., 1994; Gueguen et al., 1998). The migration is considered to be a consequence of the Apennines subduction rollback, which is driven by slab-pull or the eastward flow of the mantle relative to the lithosphere, depicted in Figure 6 (Cavinato and DeCelles, 1999). The rollback is suggested to be the cause of the extension, but mantle upwelling under the Apennines is also regarded as a possible explanation (D'Agostino and McKenzie, 1999).

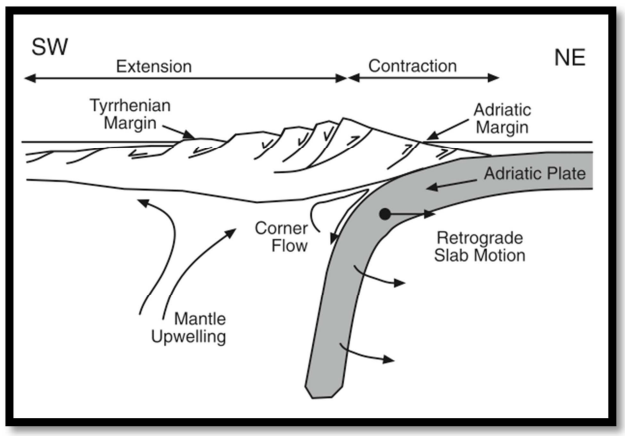

Figure 6. A schematic picture of the dominating forces in the Apennines, showing the interpreted causes behind the extension (Cavinato and De Celles, 1999).

The Apennines are a mountain belt extending through the narrow Italian peninsula, that has developed along the the margin of the Adriatic microplate (Malinvero and Ryan, 1986; Doglioni et al., 1998), and are one of the most seismically active regions in the Mediterranean. The older formations in the Apennines record thrust faulting starting from early Miocene, that has since slowed down and extensional deformation has become more dominant (Patacca et al., 1990). Some compressional activity can still be found in the outer parts of the northern Apennines (Frepoli & Amato, 2007), but in general the NE-directed thrusting in the central parts of Italy came to an end in the Pliocene (Patacca et al., 1990). Based on GPS measurements by Piccardi et al. (1999), the extension across the Apennines happens at a rate of ~6 $mmyr^{-1}$. It takes place over an 800 km long system of segmented normal faults in the central and southern Apennines (see inset in Figure 5), that has experienced several large earthquakes with magnitudes from 5.5 to 7 (Papanikolau et al., 2005).

1.4.2 Geology of the central Apennines

The bedrock of the central Apennines consists mainly of Mesozoic carbonate platforms that have been uplifted by faults and create the high topography in the area, while the bedrock in the half-grabens is Miocene flysch (Vezzani and Ghizetti, 1998; Centamore and Nisio, 2003). Many of the larger intramontaine basins have been filled with synrift fluvial and lacustrine deposits with ages older than 2.5 Ma in some places (Cavinato et al., 2002). The smooth hillsides in the central Apennines represent a typical landscape created by periglacial processes (Giraudi and Frezzotti, 1997).

There is stratigraphic evidence that some of the basins in the area were at sea level in the beginning of the Pleistocene (Gliozzi and Mazzini, 1998; Centamore and Nisio, 2003), but they have been later uplifted. D'Agostino et al. (2001a) display the indications of widespread Quaternary surface uplift, that can be seen from the well exposed Pleistocene shoreline in the Tiber river valley locating nowadays at elevations of 200–400 m. There are also numerous geophysical studies that indicate the central Apennines are still being uplifted on a long-wavelength topographic bulge, vertical GPS measurements show an uplift rate up to 2 mm/ year (Serpelloni et al., 2013), that is suggested to be maintained dynamically by mantle convection (D'Agostino and McKenzie, 1999; D'Agostino et al., 2001a).

Cavinato and De Celles (1999) explain how a sequence of basin evolution since the initiation of extension can be seen in different locations in the central Apennines: the basins grow larger, deeper, and the depositional environments change from alluvial to

fluvial to lacustrine to shallow marine. They connect these changes to the decreasing elevation and extensional subsidence that is still in progress. They name the Fucino basin – the largest intermontane basin of the Apennines located in the vicinity of Liri valley (Figure 8), as an example of an extensional basin in a mature stage with the lowest elevations (0–700 m) combined with a large area (> 250 km^2), partially marine fills, and well-integrated catchment area.

The normal fault systems in central Apennines is around 155 km long, segmented at a length scale of ~5 to 15 km, with transfer zones or relay ramps separating them (Roberts and Michetti, 2004). The faults strike mostly NW-SE, parallel to the mountain chain as shown in the inset to Figure 5. It is a system of high-angle, usually west dipping normal faults that are in many cases superimposed on older thrust faults (Cavinato and De Celles, 1999). The deformation rates in the area have been constructed by Roberts and Michetti (2004) using paleoseismological publications and geomorphic observations of displaced glacial features. Papanikolau et al. (2005) have later done further studies of the same faults, and revised the throw-rates using GPS measurements. They have derived total throw rates, as well as throw rates and offset for the past 18 ka, that corresponds to the time since the last major glacial retreat in the central Apennines (Giraudi and Frezzotti, 1997). Papanikolau et al. (2005) propose the extension rate across strike in Lazio-Abruzzo to be at maximum 3.9±0.8 mm/ year assuming a planar fault geometry and a 45° fault dip.

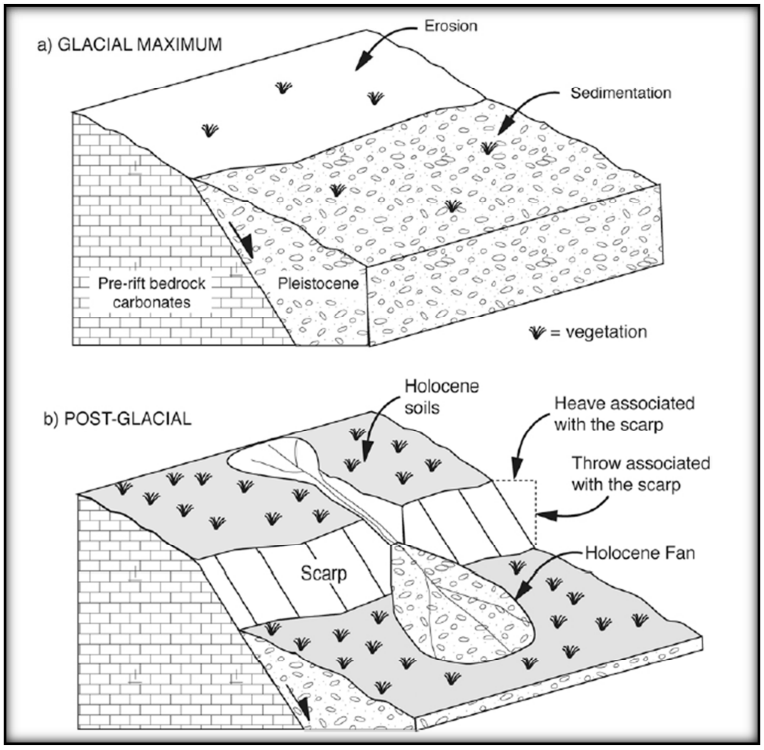

Figure 7. Development of post-glacial fault scarps in the study area (Roberts and Michetti, 2004): a) During the Last Glacial Maximum (LGM) fault scarps become buried because erosion and sedimentation rates are higher than throw rates. Cold climate inhibits vegetation's ability of stabilizing the slopes. b) Throw rates exceed sedimentation rates during the Holocene creating a successive offset of the previously gentle slopes. Datable organic and volcanic richsediments are accumulated on the slopes, and milder temperatures allow vegetation to stabilize the slopes. Holocene erosion rates are disintegrating the scarps, therefore throw rates are measured elsewhere.

Giraudi and Frezzotti (1997) have studied the glaciation in Lazio-Abruzzo Apennines. Moraines and glacial landforms reveal the presence of mountain valley glaciers during the last glaciation, and periglacial conditions were found in ice-free areas experiencing strong freeze-thaw action that provided large amounts of debris. Alluvial fans were deposited along the mountain valleys and slopes during the high erosion and sedimentation rates that sometimes even outpaced fault throwing rates during the last glacial maximum (LGM), as can be seen from the hanging wall surfaces and colluvial slopes along the active faults that are graded to the same gradient on both sides of the fault scarp, depicted in Figure 7 (a) (Roberts and Michetti, 2004).

Tucker et al. (2011) have calculated that erosion rates on fault scarps in the central Apennines show a strong reduction with Pleistocene average erosion being at least an order of magnitude higher than the Holocene rates (reduction from 0.22–0.28 mm/ year to 0.016 mm/ year). After the glaciation, the LGM fan surfaces and mountain slopes have become stabilised by vegetation as the stream discharge diminished. The late glaciation slopes and deposits have been extensively dated using paleo-vegetation and tephrachronology, revealing the absolute and relative ages of these deposits (Giraudi and Frezzotti, 1997). The vertical offset of these glacial surfaces have a close similarity

to the throw of the fault since the last glaciation, therefore it was possible to use scarp profiling to obtain mean throw rates for the last 18 ka (Papanikolau et al., 2005). An example of the method for doing this is presented in Figure 12 in the next section.

1.4.3 The Apennines – a transient landscape

Drawing together the last few sections explaining the geodynamical setting and geological history of the Apennines, one could state the area of study being in a highly non-steady state. There are strong tectonical forces: it has gone through a change in the tectonic regime from thrusting to extension that is largely shaping the area to date, with large parts of the central and southern Apennines being actively uplifted at the same time (e.g. Patacca et al., 1990; Piccardi et al., 1999; D'Agostino and McKenzie, 1999; Roberts and Michetti, 2004; Serpelloni et al., 2013). In addition, the central Mediterranean has also gone through a major change in climate during and after the last glacial period (e.g. Zolitschka and Negendank, 1996; Allen et al., 1999 and 2000). Taking into account that transient landscapes can take millions of years to find the new steady state (e.g. Whittaker et al., 2008), all this indicates that the Apennines are still readjusting to a change in external boundary conditions.

1.4.4 The Liri Valley

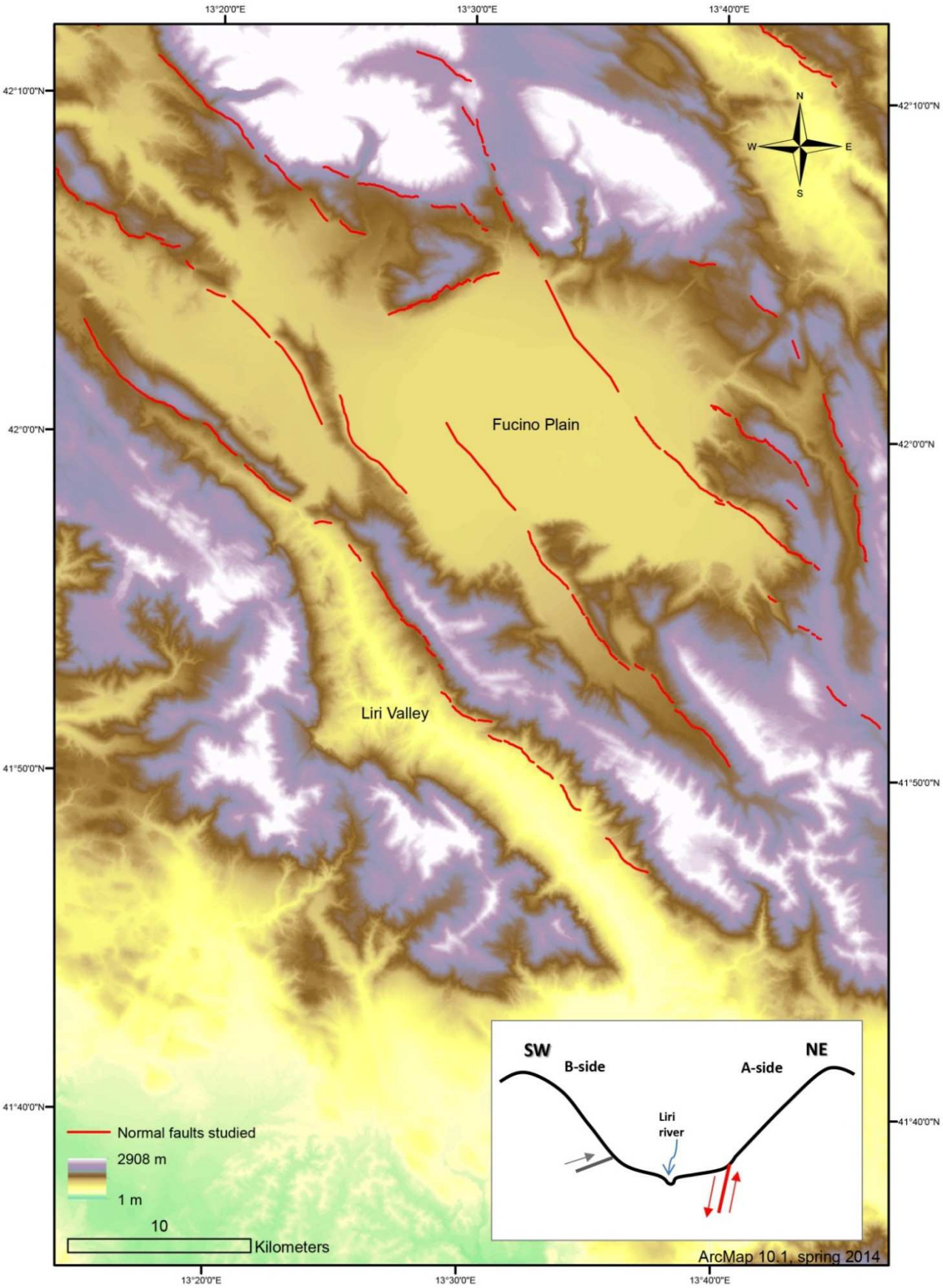

Figure 8. Elevation map over Liri valley and the surroundings, showing normal fault traces mapped by Roberts and Michetti (2004). The simplified cross-cut of the valley (inset) explains the two different sides of the valley that are studied in this thesis: the active normal fault side (A-side) and the inactive B-side with an old thrust fault.

This study is concentrating on the Liri valley, shown in Figure 8. The ground elevation ranges from around 300 m at the banks of the Liri river in the centre of the valley to above 2000 m on top of the highest surrounding peaks. The climate is Mediterranean with relatively low annual rainfall concentrated mostly in the winter season.

The geomorphology of Liri valley is marked by the wide half-graben created in the extensional tectonic setting, later deepened by fluvial activity. The topography can be described by gently sloping relief that is mostly covered in vegetation, with a few exceptions in the higher parts along the drainage divide on both sides of the valley, or on steeper sections of the slopes, showing clear signs of some type of earth flow.

The valley sides show stream deepening that cut through the calcarous slopes (Figure 9), with a few clear features of old fan deposits also visible in the satellite photos from Google Earth. Previous field excursions in the area revealed that many of the small catchments exhibit channels typical for debris flows (Figure 10 and Figure 11).

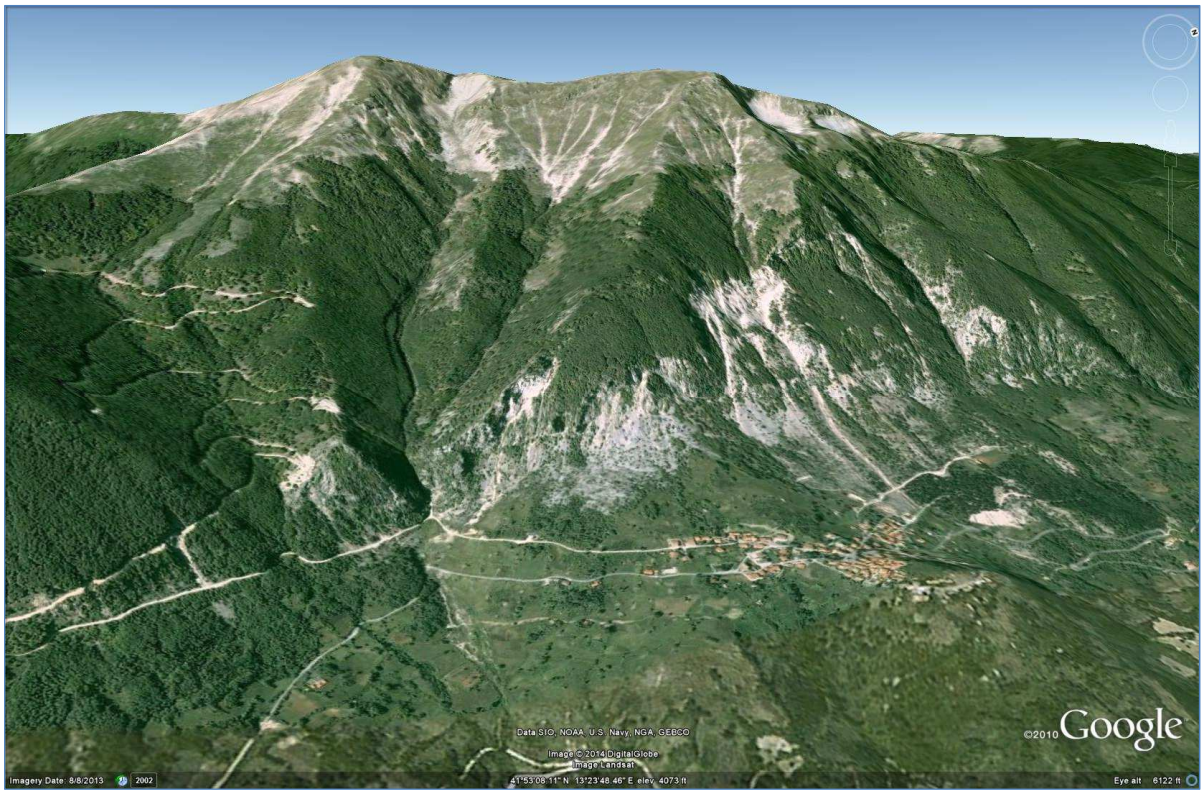

Figure 9. Examples of debris flow activity on the hillslopes. Picture taken from Google Earth, facing towards the unactive side of the valley (later on referred to as catchment B3). See the settlement for scale.

On the western side, an old remnant from the earlier tectonical regime is represented by an exhumed thrust fault that is visible in many parts at the contact between the valley fill and carbonate. The 40-km-long Liri fault is located on the eastern part of the valley. It is characterized by bedrock fault scarps that position the carbonate bedrock in contact with the flysch (Carrara et al., 1995). The history of the Liri fault appears to be quite

complex, with both strike-slip and normal movements (Serafini and Vittori, 1995). Based on the kinematic indicators collected along the fault, the youngest deformation is governed by normal movements (Serafini and Vittori, 1995). According to the observations of Carrara et al. (1995), the extensional tectonics in Liri valley and surrounding areas started in Late Pliocene.

Figure 10. Standing inside a debris flow path in one of the southern end catchments on the fault side, facing towards the inactive side of the valley seen in the far distance. Photo courtesy of Alexander Whittaker.

Figure 11. Higher up in the same catchment as in the previous picture, now facing towards the top of the fault side, a clear channel is cutting through the regolith. Photo courtesy of Alexander Whittaker.

1.4.5 The Liri fault – active or not?

There are disagreements about whether the Liri fault at present is actually active. Some of the normal faults in the area that have been active in the past divide opinions if they exhibit activity in the late Quaternary or if they have become inactive. There has been strong discussion about the reliability of some bedrock scarps taken to be representatives of active fault planes, but these might also be a misleading sign of activity if the scarps have been exposed by landsliding (Galadini and Galli, 2000). According to this some bedrock scarps, like the ones in Liri valley, could be a result from differential erosional exhumation between carbonate and flysch, and not a sign of an active fault (Galadini, 1999). The Liri fault is located in an area where GPS studies have shown extension, but the presence of major active normal faults is missing according to some publications (Galadini, 1999; D'Agostino et al., 2001b), mainly basing their criticism on that they lack signs of displaced Late-Pliocene–Holocene lacustrine, fluvial and slope deposits (Galadini and Galli, 2000). In contrast, Roberts and Michetti (2004) find it strange that the scarp height variations, as well as the similar throw and slip-direction variations along strike could be result of exhumation and not active tectonics. Roberts and Michetti (2004) claim there are also other authors (referenced in their paper) who have come to a conclusion that there are more active faults in the central Apennines than presented by Galadini (1999) and D'Agostino et al. (2001b). Therefore Roberts and Michetti (2004) consider the Liri valley fault to be active because post-glacial scarps with throw rate and height variations along strike are present.

The throw heights and rates for the Liri fault are constructed by Roberts and Michetti (2004) and Papanikolau et al. (2005). The last referred publication measured the throws from the Holocene fault scarps as shown in Figure 12, yielding slip rates averaged over the last 18 ka. The total throw profiles were also constructed by Roberts and Michetti (2004). This was done by drawing cross sections based on geological and topographical maps, tracing pre-rift horizons across the valley as described in Figure 13. These horizons express the total extension across the structures, representing the size of the total fault throw in the area, which they suggest to be around 2000 m at the maximum displacement. Roberts and Michetti (2004) note that there might be many errors as they were correlating the lithological elements that nowadays exist both above and below the current ground level, even though they tried to use structural styles that are compatible with what was exposed in the outcrops on both sides of the valleys. They further mark the possibility of errors in these throw values to be somewhat lower than ±200 m. The throw rates re-measured by Papanikolau et al. (2005) cover only the NW half of the Liri

valley (Figure 12), the last measurement located roughly half-way between the towns of Capistrello and Bolsorano, and do not extend further along the fault to the SE.

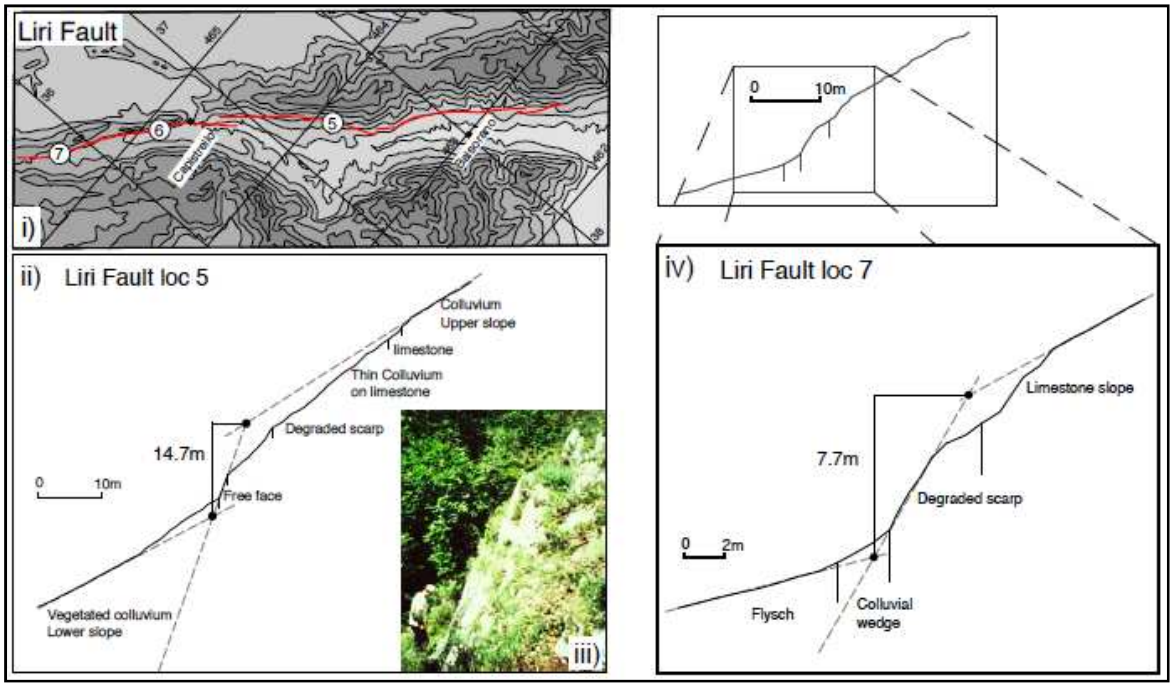

Figure 12. From Papanikolau et al., (2005), showing how they measured the fault throws in the study area. i) topographic map of the Liri fault with measurement locations, ii) profile from location 5 with iii) a close-up photo of the scarp. iv) profile at location 7.

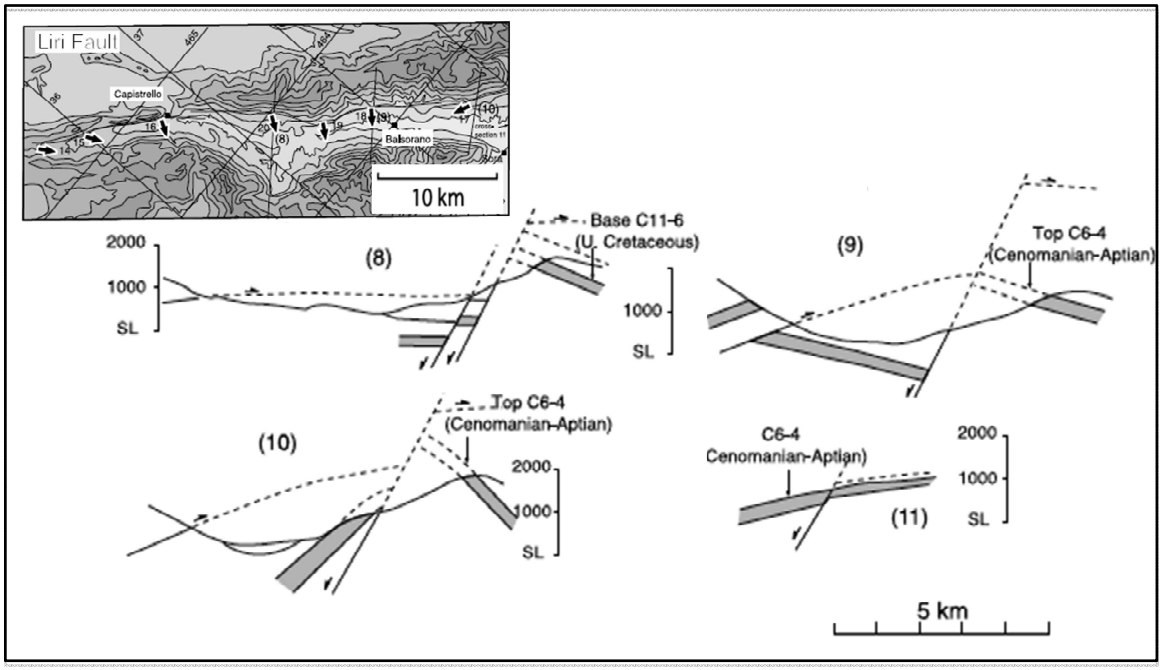

Figure 13. Constructing the total throw for Liri fault by Roberts and Michetti (2004). The labelled strata are presenting the pre-rift stratigraphy and interpreted as recorders of the total throw across the faults. The small map in the upper-left corner shows the locations of the cross sections.

A great deal of the study area is nevertheless concentrated exactly on the part where throw rates are less well constrained. Roberts and Michetti (2004) measurements from this part are not regarded as very reliable since they are only based on visual evaluations of heights of post-glacial scarps instead of accurate measurements by

construction of scarp profiles. Therefore, the throw rates at the southern part of Liri fault are referred to with caution.

Chapter 2 – Methods

The main instrument used in this study was ArcGIS, in which the catchments were first created and information extracted for further analysis. The longitudinal profiles were created through a combination of ArcGIS and Matlab. A more detailed explanation of these procedures, as well a description of the analysis and accessory work, are given in this chapter.

2.1 ArcGIS

A 20-m digital elevation model (DEM) of Lazio-Abruzzo was used to study the geomorphology in ArcMap 10.1., which is the latest version of ArcGIS (Geographical Information System). Slope and area data of the catchments along the Liri valley were extracted in ArcMap, which also allowed the results to be visualized in an effective way.

It is important to keep in mind that the data in GIS is only a generalized expression of the real world, not able to fully cover the complexity of the actual geomorphology of the studied location in detail. A lot of information is missing to begin with due to required simplifications when creating the spatial data structure. As an example, in this thesis, the data used to study the Liri Valley is based on a 20-m DEM, which sets the limits for information being tied to grids of 20x20 m cells that have only one value or attribute each. This resolution is too coarse for acquiring knowledge of any features smaller than 20 x 20 m. Nevertheless, for examining how tectonical processes influence geomorphology, this resolution is thought to be good enough, since the changes in features are relatively large in scale. Some artifacts that occurred in this project will be discussed in the following chapters. The working steps for creating the long profiles are explained next. Note the illustration on page 20 which summarises the main working steps in a nutshell.

ArcGIS 10.1 was first used for preparing the 20-m DEM by filling possible gaps (raster cells with no data) and clipping the DEM to a smaller study area to speed up the analysis. After this, rasters of flow direction and flow accumulation were created.

For defining the stream network, the flow accumulation grid was conditioned to take into account only pixels with flow accumulation values > 200, which represents a drainage threshold for a stream to form. All other grid cells are assigned a null value.

"Larger than 200" was thought to be enough for taking into account also larger debris flow channels with this resolution of the DEM. This threshold corresponds to catchments with a drainage area ≥ 0,08 km^2. A higher threshold value would take only larger rivers into account. A smaller threshold value of > 50 was also considered (see Figure 14) since it would have allowed streams that reach the upper slopes to be extracted that could be regarded as the initiation points of potential debris flows. However, a threshold value > 50 does not change the extracted long profiles to a significant degree, and just makes the stream network more complicated by adding tiny tributaries that in most places seemed to be very artificial. For being able to examine small active debris flow channels for purpose of hazard assessments one would, in any case, need a much more detailed DEM of 10 or 5 m. As the aims of this project were to investigate geodynamic processes affecting the streams over a range of scales, a larger threshold value was therefore chosen.

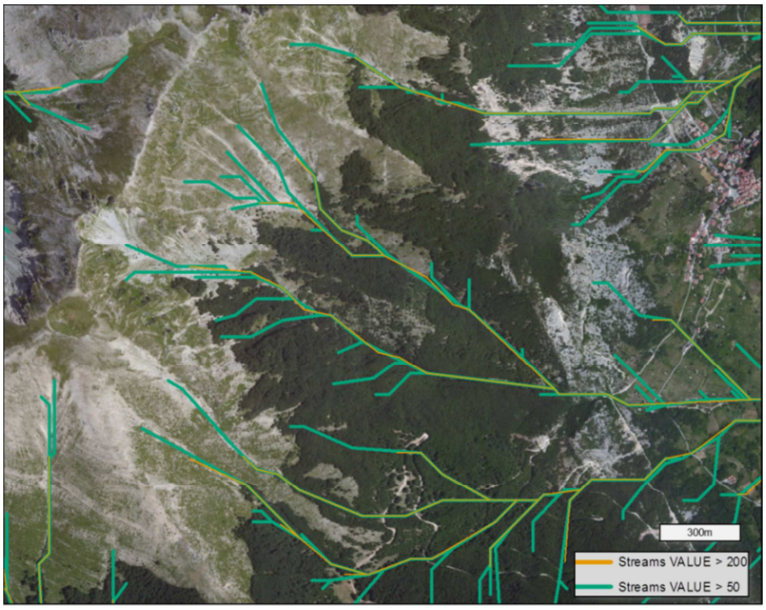

Figure 14. Representing streams with different threshold values (orange > 200; green > 50), and how this changes the extent of the streams when overlaying them on a basemap in ArcGIS.

For describing the stream network, stream order was defined after the Strahler method. This characterizes the streams by how many tributaries they have: first order streams have none, and order increases downstream when two streams of the same order meet each other (Strahler, 1957). This stream order raster was afterwards converted into a vector stream line.

From the layers created in the previous steps, catchment boundaries were defined next. This was started by defining pour points, which mark the downstream limit of the watersheds located as close to the Liri river as possible. The pour points calculate all the drainage to that point from the adjacent pixels, in other words the number of pixels

flowing in to that pixel. In addition, the pour points were snapped to accumulation grid to ensure that they are located on it. Then watersheds were created by using the flow direction raster and the snapped pour points, and the result was converted into a vector. These pour point and watershed extraction was done by systematically choosing adjacent catchments with streams that reached above the Liri fault trace and/ or the main lithological contacts (see section 3.1).

Once the watersheds were created, the original DEM and flow accumulation DEM were clipped using the watersheds as boundary lines, as these are needed when drawing the long profiles. Slope maps, hillshades and contour lines were also created for the new watersheds (see the work flow below).

2.1.1 Work flow for creating watersheds in ArcGIS

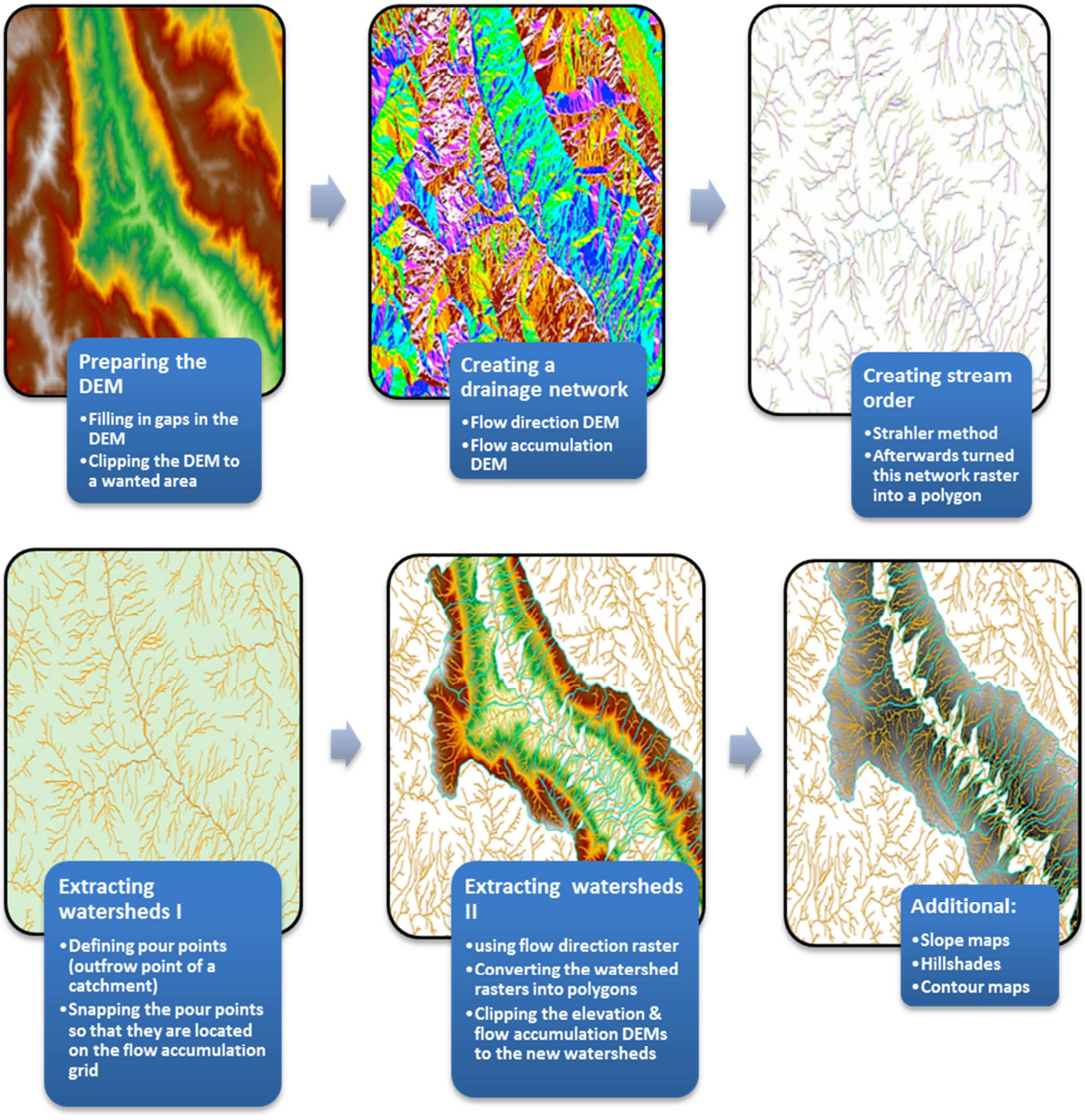

2.2 Working steps behind extracting long profiles created in Matlab

After creating the watersheds in ArcMap, the next step was to export the flow accumulation grid and the original elevation DEM to ASCII files. These are *.txt* files that can be further converted into *.mat* data files, which are readable in MATLAB.

The Stream Profiler toolbar (provided by http://geomorphtools.org) was used in ArcMap to select headwater points. Matlab uses these as starting points and traces them down the stream creating a long profile for each channel using the flow accumulation and elevation grids. In Matlab, long profiles and log-slope vs. log-drainage area plots were extracted (see e.g. Figure 15), and used further to extract the values for channel concavity and steepness, which were introduced in the previous chapter (Equation 1).

First step was to extract the long profiles for all of the catchments, from as close to the drainage divide as possible down to the Liri river. From these elevation vs. distance plots, a few channels with the smoothest profiles were chosen, to start the analysis with the simplest and clearest ones before having a closer look at the other, more complicated channels.

2.2.1 Channel steepness and concavity indices

The analysis of the long profiles starts with specifying linear regression limits on the log-log plot of slope against drainage area, in order to determine the concavity index (θ) and steepness index (k_s) from Equation 1 (Wobus et al., 2006). Figure 15 and Figure 16 show examples how the regression limits for calculating these indices were chosen from the slope-area log-log plot. This was done with the mindset of finding clear linear trends on the log-log plot with as many points on the line as possible. It also allows the best fit for concavity when separating individual linear segments that were a common feature on most of these plots (e.g. Figure 15 and Figure 16). The process was started with the ten smoothest profiles mentioned above, that gave an insight to how the dataset works and how the concavities reflect to different regression limits.

Because channel slopes are dependent on basin shape, or variations in how discharge is accumulating downstream, small differencies or uncertainties in the concavity index (θ) can cause great variations in the steepness index (k_s) in Equation 1, therefore a normalized index is often presented for the purpose of comparison. There are a couple of methods for doing this, for example as reviewed in Kirby and Whipple (2012). The one used in this study starts out from a general view that fluvial channels in steady state should have quite a narrow range of concavity indices ($0.4 \leq \theta \leq 0.6$) (Whipple and Tucker, 1999). With this in the background, a normalized steepness index (k_{sn}), that

suits for comparing stream profiles from different sized catchments, can be determined by evaluating slope-area regressions using reference concavity index (θ_{ref}) (Wobus et al., 2006):

$$S = k_{sn}A^{-\theta_{ref}} \quad \text{(Eq. 3)}$$

This method does take into account the dependency of profile gradient on drainage area (Wobus et al., 2006). It has been found out from experiments that values for reference concavity between 0.4 and 0.5 describe well most mountain streams (Kirby and Whipple, 2012). Most literature until now use θ_{ref} of 0.45, which was also used in this study.

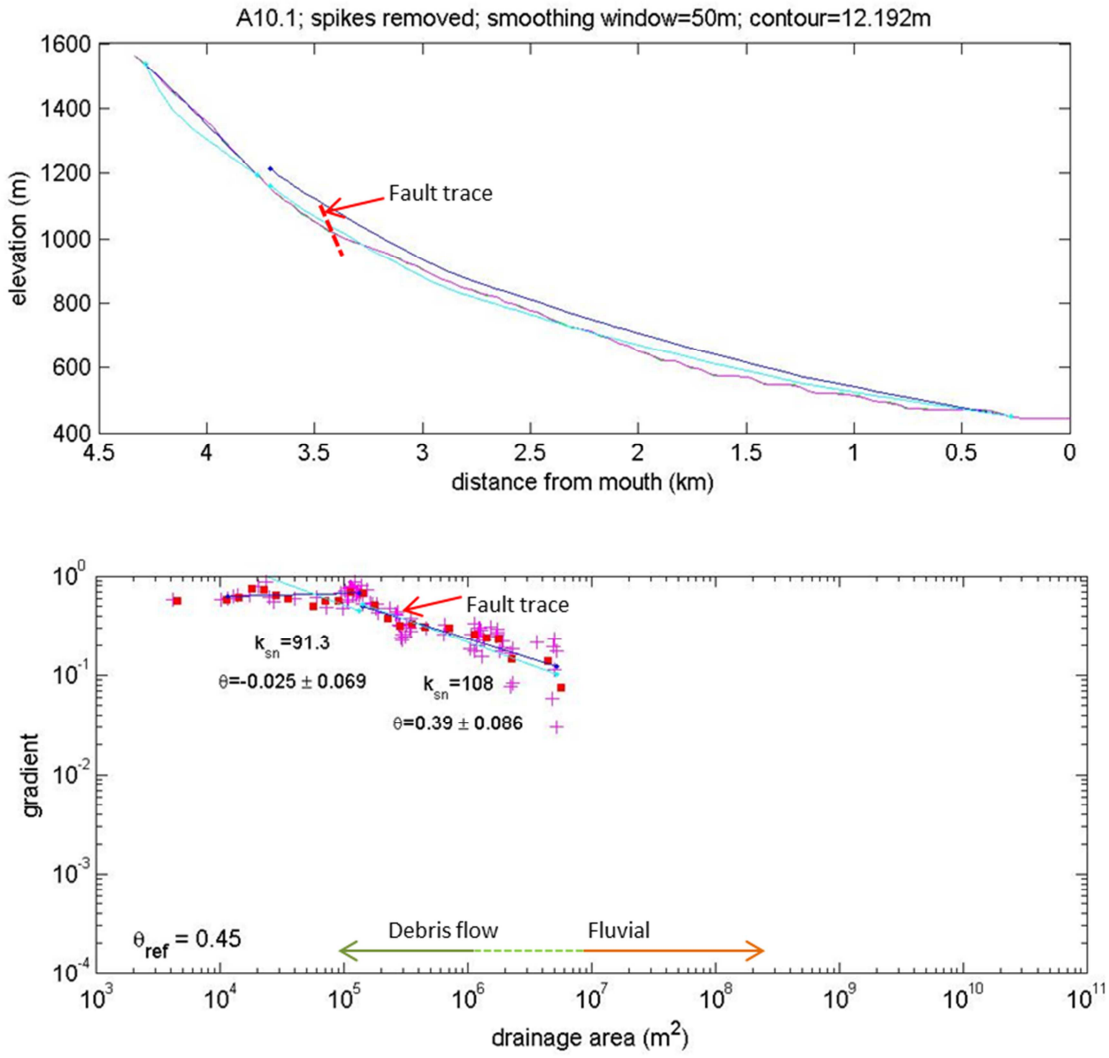

Figure 15. An example of long profile and log-of-slope vs. log-of-drainage area plot created in MATLAB from the Liri fault side, located NE in the Liri valley (A-side). The pink colour represents data extracted from the DEMs. The dark blue colour shows profiles and trends predicted by the regressed channel concavity, θ, and the cyan ones represent the specified reference concavity, θ_{ref} = 0.45. Red squares are log-bin averages of the slope-area data. The red dashed line indicates the position of the Liri fault. Note the typically assumed fluvial-debris flow transition (e.g. Stock and Dietrich, 2003) marked on the log-log plot.

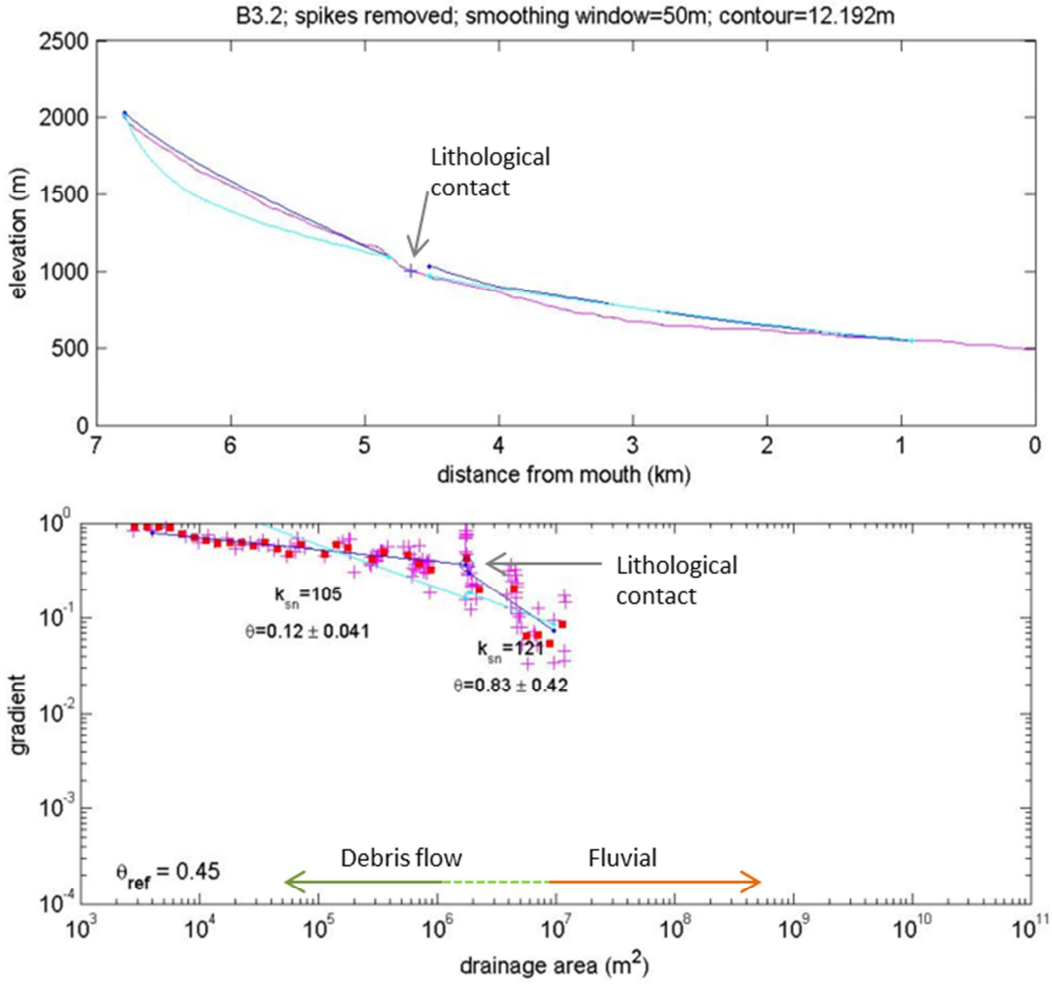

Figure 16. An example of a channel long profile and log-of-slope vs. log-of-drainage area plot from the inactive side of the Liri valley (SW side; B-side). The plus mark along the profile points out the location of a knickpoint, or any other user specified point that is wanted for further examination, appearing in the lower plot as a circle. Other explanations as in Figure 15.

2.2.2 Background noise and data scatter

The channel gradient analysis is dependent on digital elevation models (DEMs), that can have random fluctuations obscuring the data. Different data handling methods have been developed for reducing the background noise from pixel-to-pixel slope estimates from DEMs (Wobus et al., 2006). Often some insignificant noise in the long profiles extracted from DEMs can result in large scatter in channel slope estimates, and when taking the spatial derivative, the noise becomes even greater. There are various procedures for trying to reduce this noise, explained e.g. in Wobus et al. (2006) and Kirby and Whipple (2012), but the one used by Matlab in this study involves averaging the logarithm of the slope values and using logarithmic binning of the drainage area data (Figure 15).

A positive outcome of log-bin averaging is that the smoothing window size grows the further downstream you go. In addition to that it does not create any averaging of slope values that are very different from each other across tributary stream junctions where

there may be a large change in drainage area (Wobus et al., 2006). But log-bin averaging has its weaknesses too, since the it is likely to be influenced by outliers that might draw the result in one way or the other significantly, a problem often faced when using rough data from low-resolution DEMs (Wobus et al., 2006).

Results of all long profiles and log-log plots in are presented in the Appendix A. All analyzed long profiles and concavities are visualised in graphs and figures in the next chapter, where they are also discussed in more detail.

Some of the log-log plots were extremely scattered, which made the extraction of a reliable concavity index really difficult. These are presented in Appendix B. The scatter is distorting the concavity measured, especially when there are not enough data points (needs minimum three) for it to function properly. This appeared to be a problem expecially in some of the smallest catchments (e.g. A2, A18, see Appendix B). There was a lot of scatter in some bigger catchments as well, especially when the profile was very terraced. Sometimes it would have involved taking more than three different regressions (e.g. catchments B1, B5) due to the bumpyness of the profile. These kind of catchments, or parts of the profiles that were too complicated or had something suspicious with the data, were either left out of the slope-area analysis, or presented in grey in the final figure presenting concavity measurements (see Figure 34).

2.2.3 Explanations of the used concavity groups and quality check on the regression limits

Figure 17 shows how the concavities were grouped in this study, with indications to the position of the linear line on a log-log plot representing negative (pale blue), low (blue), moderate (yellow) and high concavities (purple).

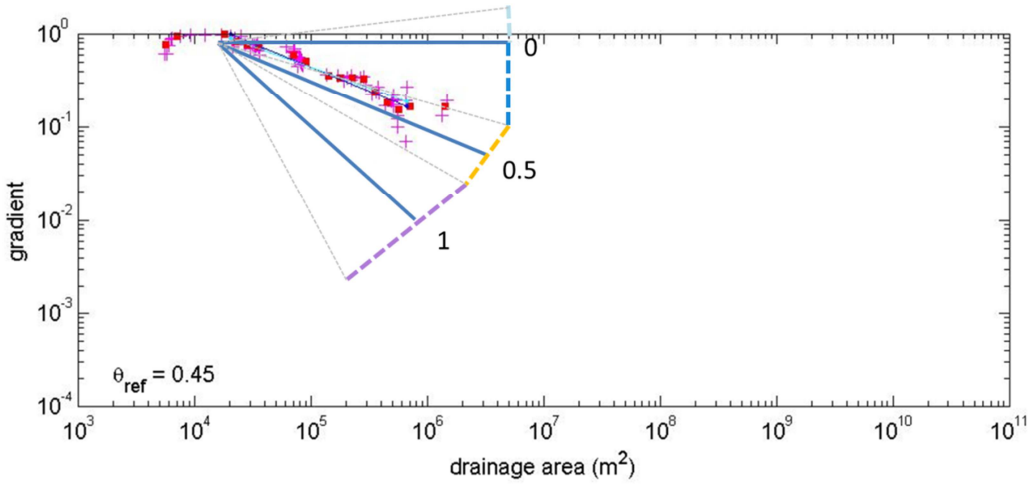

Figure 17. An example of a log-slope vs. log- draiange area plot with indications of the concavities in Figure 34 (in the Results), how they look on a log-log plot. The blue lines indicate the concavities for 0, 0.5 and 1 respectively. The coloured dashed lines show the margins for high, moderate, low or negative concavities, coloured as in the final concavity map (Figure 34) .

How the catchments were defined and how the regression limits were chosen in this project differ slightly from other studies. Therefore, a quality-check of extracted concavities was performed on the channels on the the faulted side of the Liri valley (A-side).

The chosen regression limits differ from previous studies (e.g. Densmore et al., 2007), which defined the catchment areas only upstream of the active fault traces, the assumption being that downstream of a fault there may be a change from erosion to deposition. However, in this study the extracted catchments have been defined all the way down to the Liri river as it is not obvious where the change from incision to deposition occurs in this area. Nevertheless, it does not necessarily mean these two approaches give completely different results. In this study, the catchment area is slightly bigger than it would be if it was limited only to upstream of the fault, but it does not seem to change the concavity values significantly. A check-up of concavities were taken choosing the regressions on the long profiles limiting only upstream of the Liri fault trace. An example of this is represented in Figure 18, which shows how the concavity changes (from 1.7 to 0.96), but can still be regarded to be in the same classification of high concavity (> 0.7, see Figure 17).

One big effect of the catchment area extending so far down is that effects of the valley bottom sedimentation may also be recorded in the concavities. This is noted here to demostrate the awareness of this effect already at this early stage, but it is discussed further in the sections 4.2 and 4.3.

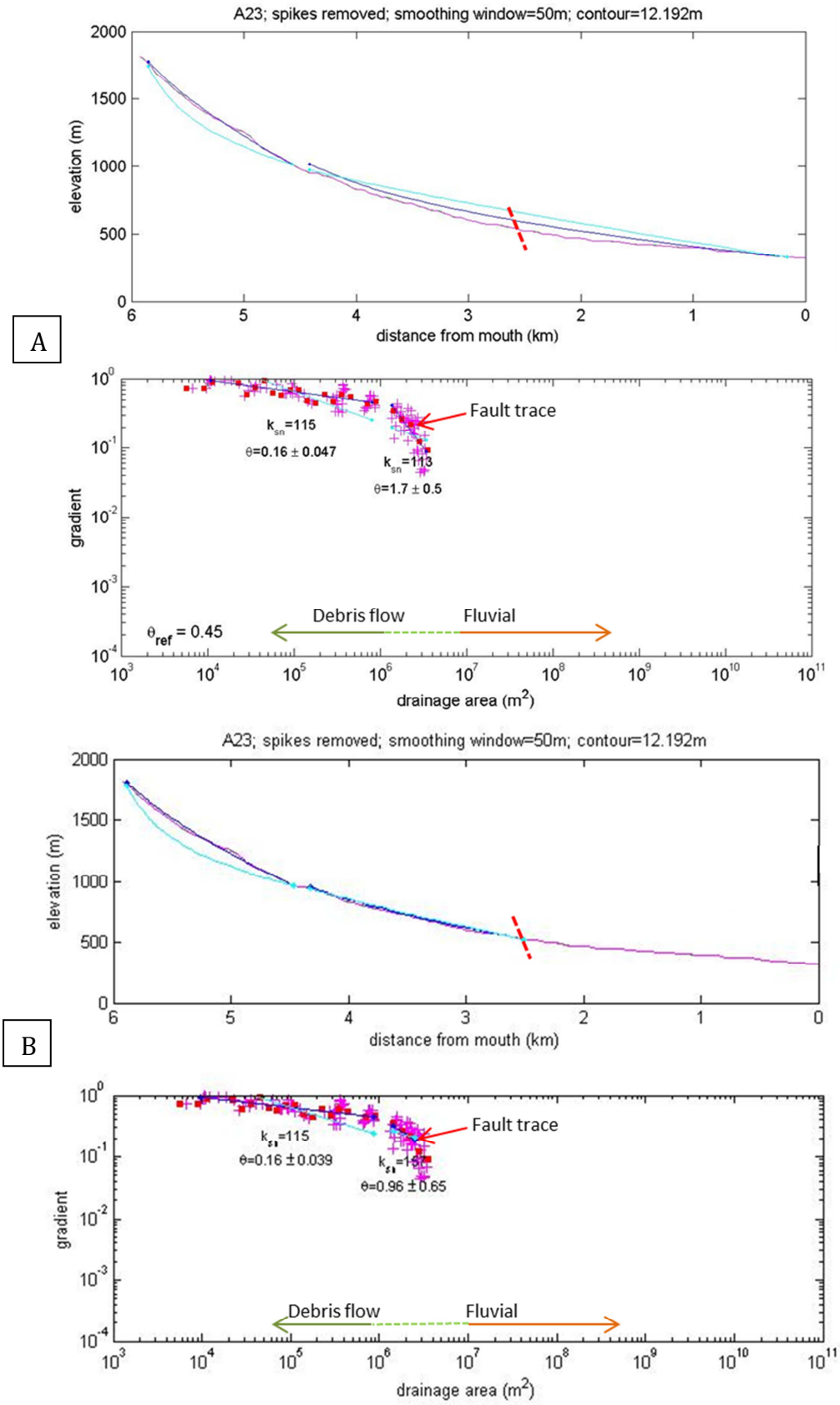

Figure 18. Displaying the long profile and log of slope vs. log of drainage area plot of stream A23 that is used as an example of how different regression limits change the concavity value. Colours and explanations are the same as in Figure 15. A. shows the results when choosing as many points as possible inside the regression limits, covering more or less the total length of the profile. B. shows the regression limits if the calculation was done only to where the stream crosses the fault trace. Note how quite a large portion of the long profile is actually recorded as few data points in the log-log plot (rest of the profile after the fault).

2.2.4 Challenges considering long profiles and log-log plots

The log-log plot is highly sensitive to small variations in how the regression limits are chosen. While working extracting the long profiles, it was necessary to return to some of the catchments multiple times to reconsider the defined regression limits. It was noticed that when choosing the regression limits it was difficult to repeat the same regression of the same catchments again and get same results, i.e. same value for concavity. For example, a concavity could change from 0 to 0.12 to 0.35 in the same catchment depending on exactly which regression limits were specified. The k_{sn} values were fluctuating more persistently (see e.g. Figure 18 values). These changes in θ and k_{sn} were more apparent the fewer points there were within the regression limits. In the stream profiler tool, it is not possible to choose individually which points the regression calculation should include, only an approximation of group of points can be selected based on visual examination of the graphical data. Therefore, the program can output quite different regression results, that are changing depending on small variations less than a millimeter on the graphical images, and thus which points are included to define the line for the power-law fit, which is the output of the regression calculation. The scatter in the data increased this phenomenon even more.

Despite this phenomenon, the concavity values were still inside the group they were originally defined belonging to. A change of representative concavity group was only noticed to happen in two of the catchments studied here, and this hardly affects the overall concavity trends that were observed (see section 3.6).

The regressed channel concavity (i.e. the dark blue lines in the examined elevation vs. distance plots in Figures 15, 16 and 18, and in the Appendix A) in most of the channels do not always sit perfectly on top of the long profile extracted form the DEM (the pink lines in the same plots), meaning the concavities measured might not be as representative as first thought when choosing as many points on the log-log plot as possible to cover as much of the profile in the regression calculation as possible. While making a quality-check for some channels and choosing shorter regression limits extending only to the fault, it was noticed that these regressions sit better on the actual profile, as in Figure 18 (b). However, this quality check also shows that although the concavities changed to some degree, they were still representatives of the same concavity group (i.e. negative, low, moderate, high) as obtained using the first method described above. Thus, as this study was interested in showing the overall patterns rather than finding exact concavity values, these minor changes in the concavity values

depending on the fit between the profile and regressions are not considered very important.

2.3 Accessory work

All the watersheds were given names to help to identify them later on. A number of characteristics of the newly created watersheds were collected and noted down. These include drainage area, elevation of the drainage divide, and stream order that could be plotted to compare the differencies. Based on the characteristics of the watersheds, they were divided into groups to make the further comparison clearer.

Aspect ratios were also calculated for each catchment by dividing the length of the catchment by the width. These were measured in ArcMap, taking approximately the longest dimension parallel to mainstream channel for the length and the widest part of the catchment to obtain the width. An aspect ratio expresses the form or shape of the catchment with respect to a circle that has an aspect ratio value of 1. The bigger the aspect ratio is, the longer and thinner the catchment form is, and vice versa, smaller number indicates shorter and wider form.

To help understand what might be causing changes in the channel long profiles and topography, a simplified map of the basic geological elements in Liri valley were drawn in ArcMap. The result was a map representing structural and lithological variations in the area, based on the geological maps of Vezzani and Ghisetti (1998) and Carta Geologica d'Italia (1967; 151 & 152) with scales of 1:100 000. The locations used for the normal fault segments in the Liri valley on A-side (NE-side) are based on the field mapping done by Roberts and Michetti (2004). In this study, some of these fault segments were linked in ArcMap by freehand drawing, simultaneously comparing it to the geological map provided by Vezzani and Ghisetti (1998), who presented a more continuous, but perhaps not as detailed fault trace in their map. The old thrust fault that is visible in the inactive side was also drawn in based on the map of Vezzani and Ghisetti (1998)

The fault location on the active A-side (and lithological contact on the inactive B-side) was measured from the DEM in ArcMap by taking the elevation where extracted streams cross the fault trace, and then plotting a point at this elevation on the long profiles in Excel. On the active side, the freehand-drawn fault locations were used in places where the fault trace might be suspected to be present but had not actually been mapped by Roberts and Michetti (2004). This was done in order to check whether long profiles of such channel crossings included knickpoints that could indicate the trace of the fault.

Also a slope map representing the changes in the degree of topographic slope was created in ArcMap. Finally, all the abrupt slope changes or knickpoints in the channel long profiles were individually compared to these geological and slope variation maps.

Because the Liri river is the primary controlling factor over the smaller catchments in the valley, a short analysis of the river profile was carried out. This included also examining the largest cemented fan in the southern part of the valley, that shows clear incision on its edges.

Chapter 3 – Results

In this chapter, maps and plots from the project will be layed out in the following order:

- starting from the working names of the catchments
- comparing their geomorphological features extracted from the DEM
- examining the geology of the area from the constructed geological map
- examining the changes in the slope steepness
- showing the long profiles and examining them in the light of the local variations in geology
- presenting final maps where the channel concavity and steepness indices are overlain on the previously explained geological elements
- examining the long profile and evidence for incision along the Liri river

At the end of this chapter, the reader will hopefully have a better idea of the differencies between the catchments and the data extracted from them, thus giving background for the discussion of what might be the causes behind these differencies.

3.1 Working names for the catchments

A total 30 catchments on the NE side, supposed active Liri fault side (referred to as A-side) and 22 catchments on the old thrust fault side, the SW side (referred to as B-side) of the Liri valley were extracted in ArcMap. Each of these catchments was given a name to help locate them as well as to help the future referencing.

Drainage area seemed like a natural way of dividing the catchments into groups. The grouping helped to manage the data for further queries and made visualizing of the catchments easier. This categorization was made between *big* (drainage area > 3 km^2), *small* (drainage area < 3 km^2) and *tiny* (~1 km^2) respectively. The names and grouping

of the catchments are shown in Figure 19. This is the basic figure that helps identify the catchments in the following results.

The Liri fault side is also divided into two different sections for the purposes of this study, pointed out with arrows in Figure 19: Section 1 and Section 2. This division comes mainly from the distinct differencies between the long profiles, as shown below, but also the morphologies of the catchments are quite different in these two sections (see section 3.5.1).

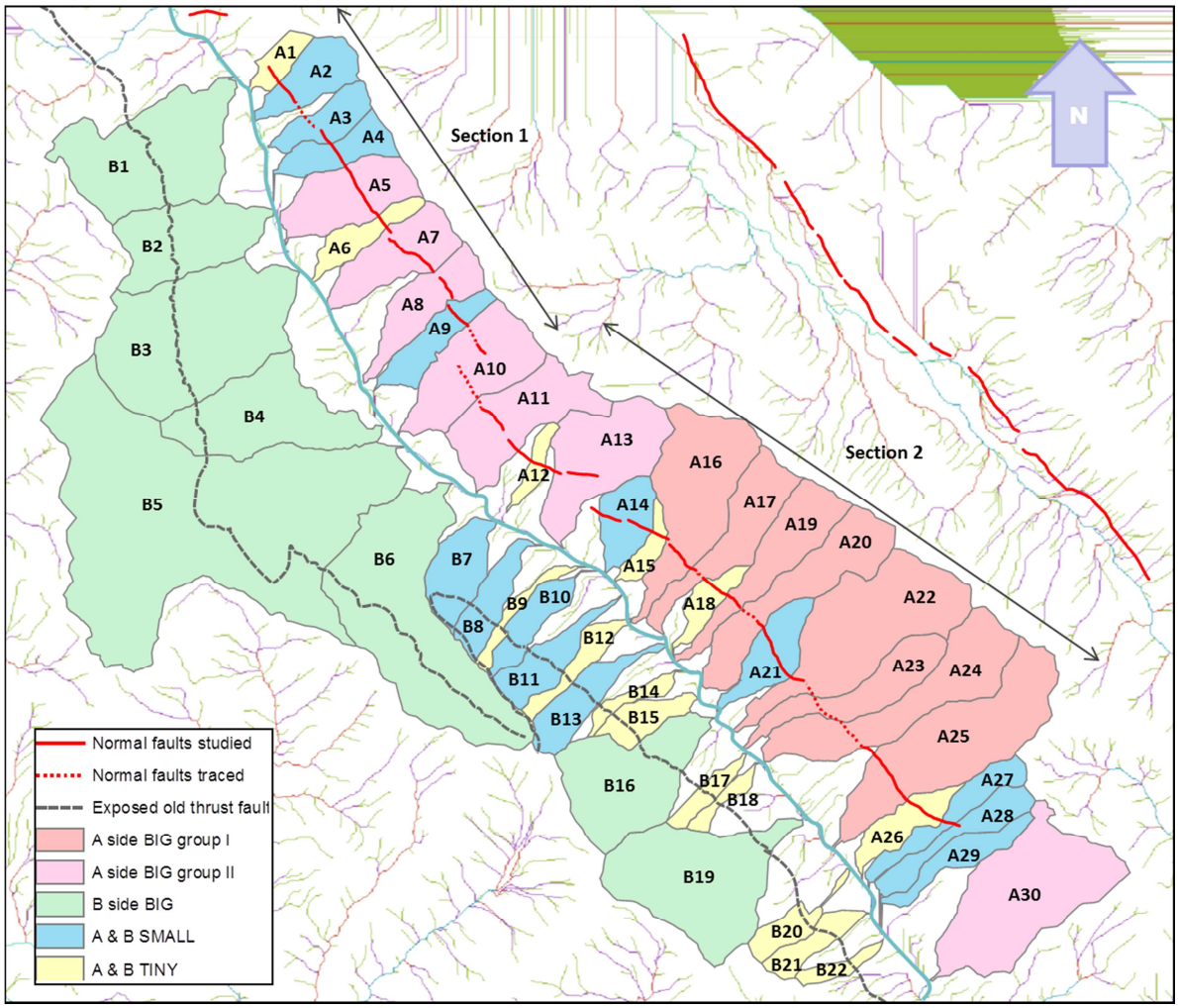

Figure 19. Showing the working names of the catchments with colour indicating the drainage area size. The thicker blue line depicts the Liri river, and the Liri fault is the one cutting across the A-side catchments. The division of big watersheds on the active Liri fault side (A) in to group I and II was made because of the clear difference in catchment shape and longitudinal profiles.

3.2 Variations in catchment characteristics along the Liri valley

The graphs in Figure 20 and Figure 21 show the elevation change along the drainage divide and drainage area variation from watershed to watershed when moving from north to south along both sides of the Liri valley. In these graphs only catchments that reach the drainage divide are displayed for revealing a clearer trend. This means that some of the tiniest catchments (~1 km^2) are excluded from these plots.

These graphs show quite clearly how the inactive side (B-side) has a higher drainage divide elevation and larger drainage areas in the catchments in the northern end of the valley compared to the active Liri fault side (A-side). The huge catchment B5 exaggerates this drainage area pattern to some degree. Towards the southern end, the drainage divide elevation increases in the active side compared to the inactive side, whereas the drainage area variations become more similar.

Figure 22 and Figure 23 represent the aspect ratio and stream order in all catchments on both sides of Liri valley. The catchment form appears quite equally mixed on both sides when looking at the length-width ratio, but the inactive side (B-side) has overall more rounder catchment forms compared to the active side (A-side). In addition, both sides of the valley seem to be dominated by 2nd and 3rd order streams, although the bigger catchments in the northern end of the inactive side naturally have higher order than the small catchments on the active side. The active side catchments have some higher order catchments (order 4) towards the southern end of the valley.

The drainage area and stream order are considerably larger in the inactive side, especially in the northern end. This is mainly a result of choosing the outlet point of the catchments to reach the junction with the Liri river, since the river is located closer to the active side of the valley.

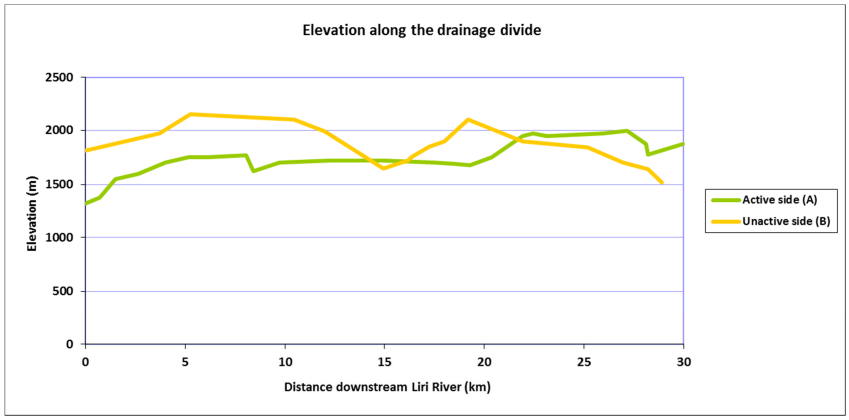

Figure 20. Plot showing the elevation change along the drainage divide on both sides of Liri Valley. Only the catchments reaching up to the main divide are included in the graph.

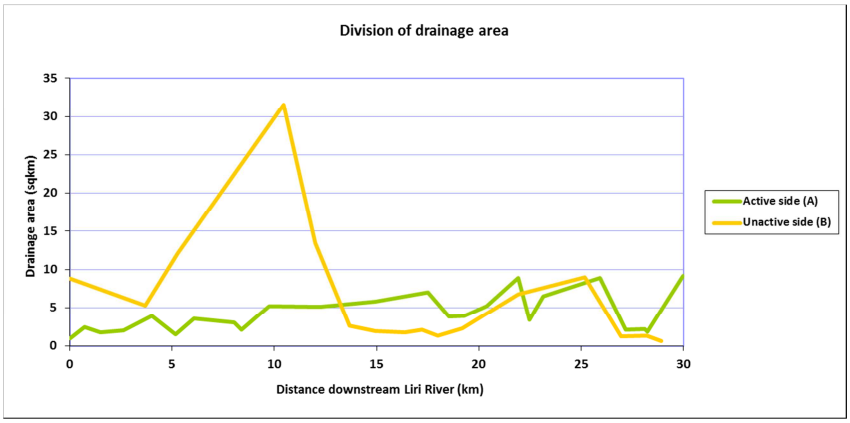

Figure 21. Plot showing the same catchments as in the previous graph, but this time showing the drainage area of those catchments.

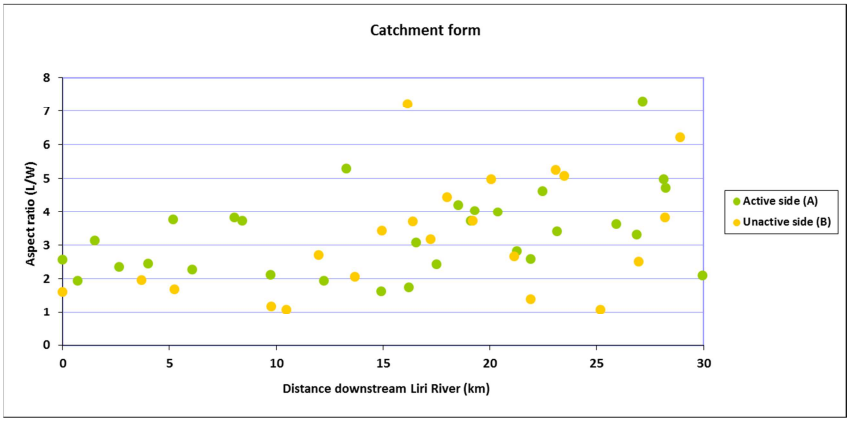

Figure 22. Showing the variation in the catchment form, measured as an aspect ratio (length divided by width). All catchments are plotted. Higher number indicates longer and thinner catchments related to its own form, and vice versa.

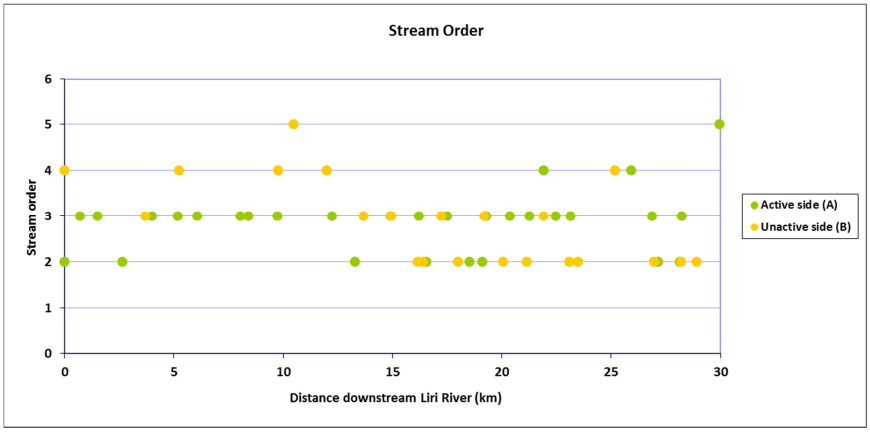

Figure 23. Depicting the stream order of all the catchments at the point where they meet the Liri river, based on method by Strahler (1957).

3.3 Geological map of the Liri valley

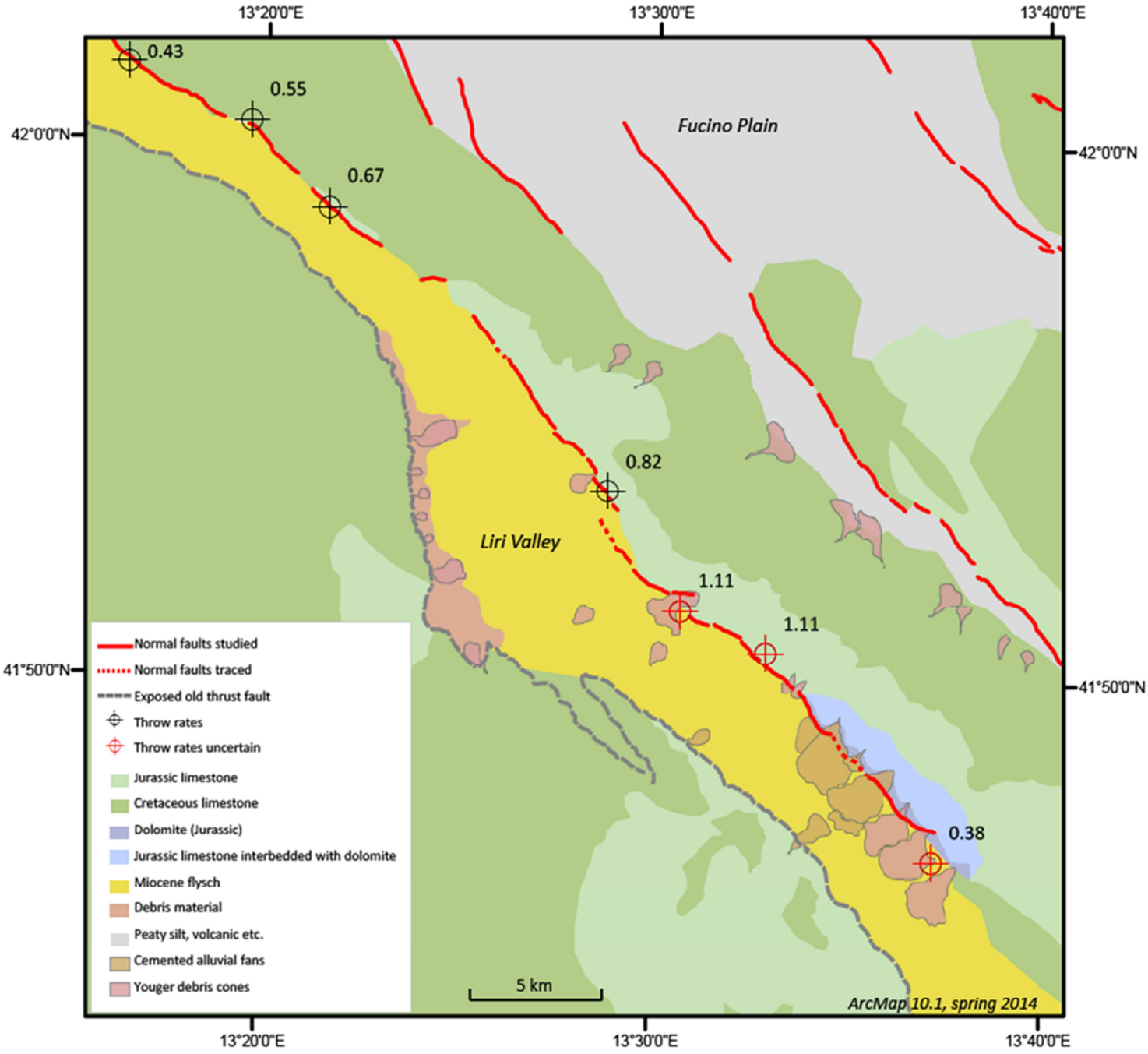

Figure 24. A schematic map of the geological elements in Liri valley and surroundings. Note especially the measured throw rates in Liri fault, starting from the north-west corner and growing towards the center of the study area. 0.82 mm/ year in the center of the map is indicating the last re-checked throw-measurement, after which the red signs show the area where the rates are not as well constrained (as will be explained in the text below).

Figure 24 shows the main geological elements in Liri valley. The lithology is based on the geological maps provided by Vezzani and Ghisetti (1998) and Carta Geologica d'Italia (1967; 151, 152) with scales of 1:100 000. Dark green colour represents Cretaceous granular limestone. The lighter green is also limestone, but more massive and from the Jurassic period, and is in general more dolomitic in consistence. Exposures in the bottom of the Liri valley in the map is filled with Miocene flysch, indicated by yellow. The southern part of the Liri fault side is also highly dolomitic, indicated by bluish colours.

Some relatively young (Holocene) alluvial fans and loose debris material at the foot of the hills is also drawn on the map, represented by reddish-pink colours. These consist mainly of calcareous scree. There are also a couple of older (Pleistocene), cemented alluvial fans depicted on the map with brown. Light grey shows the Fucino plain which is filled mostly with peaty silt interbedded with sand and volcanic products.

The locations used for constraining the location of the normal fault segments in Liri valley were published by Roberts and Michetti (2004), who checked the locations of faults given in older geological maps of Italy (Robets and Michetti, 2004 and references therein). They note that there might be errors in these fault traces, because vegetation covered the actual locations of the faults in some places. Due to this they used geomorphic features and the older published maps, that might contain errors as well, to construct the fault traces. According to them this error is within around 100-200 m perpendicular to the fault strike. They also explain that recognizing the lengths of individual fault segments was even harder.

Connected segments of the faults are shown in dashed lines. These dashed lines are meant only for *estimating* where the actual faults could be located. This was done to help identify where the channel long profiles are crossing the potential faults, and to see if the profiles show any changes, even if the faults have not been actually mapped there. The old thrust fault on the SW side of the valley (B-side), as well as the lithology in the study area were constructed using a geological map of Italy with a scale of 1:100 000, provided by Vezzani and Ghizetti (1998). The old thrust fault is inactive, exhumed, and represents a major lithological boundary between the valley fill and carbonate rocks. These lithological boundaries are also clearly visible in the slope map (Figure 25) which emphasises where steepest slopes end and gentler valley bottom slopes begin on both sides of the Liri valley.

Due to the complexity and poor resolution of the geological reference maps — with no georeferenced and projected form of them available, it was difficult to visualize the *exact* locations of the faults in relation to the examined streams and watersheds. The same problem was faced when examining lithological changes in the valley. Therefore, the lithological change, as well as fault traces depicted in this thesis are considered to be where a clear change can be seen in the DEM in the degree of slope on the valley sides, coinciding with the mapped fault traces of Roberts and Michetti (2004). Additional fieldwork for mapping the faults and bedrock was beyond the scope of this project. It is thus highlighted that these elements depicted in the resulted geological map of Liri

valley are simplifications and should be considered as a guidlines with an uncertainty of up to a few hundred meters.

The fault throw rates in Figure 24 for the active NE side of the Liri valley are based on the work by Papanikolau et al. (2005) who revised the observations made by Roberts and Michetti (2004). These new measurements given in black indicate 30–40% lower values of throw rates in the locations they covered, e.g. 0.82 mm/ year instead of 1.11 mm/ year (Papanikolau et al., 2005). The throw rates given in red are taken from Roberts and Michetti (2004). As mentioned before, these throw rates shown in red are not regarded as totally reliable since they are only based on visual evaluations of heights of inferred post-glacial topographic breaks in slope instead of accurate measurements by construction of fault scarp profiles.

3.4 Slope map

The slope map presented in Figure 25 was the most practical map when analysing the channel long profiles in addition to the geological map. This map helps explain the sudden changes in the elevation, i.e. knickpoints on the long profiles, coinciding with the sudden changes in slope gradient. A really interesting aspect of this map is how in some of the larger catchments you can clearly see incised channels, e.g. A-side BIG group I catchments. Also the flatter top part of those A-side BIG group I catchments is visible, marking the change from Jurassic to Cretaceous limestones. Some of the old alluvial fans are also visible, i.e. between the catchments of A24 and A25.

The map also shows how the Liri river is changing its course along the valley. The location of the river seems to change when moving from the northern end of the valley towards the south: in the north it is located closer to the active fault side (A-side), where the catchments are smaller making the inactive side catchments look large in comparison, even though the parts of the catchments that are on the steepest slopes are not that different in comparison. The river changes its path the further down south, moving further from the active fault side (A-side) towards the inactive side (B-side). The inactive side catchments towards the southern end of the valley are small and skinny and mostly restricted by the one big catchment (B6), with the exception of two the big round ones (B16 and B19). In comparison, the active side catchments become more longitudinal in form (aspect ratio >> 1), and many of them have a flat part at the top, indicated with arrows in Figure 25. In the following paragraphs where the long profiles and concavities are discussed, this map is also very useful to have at the side.

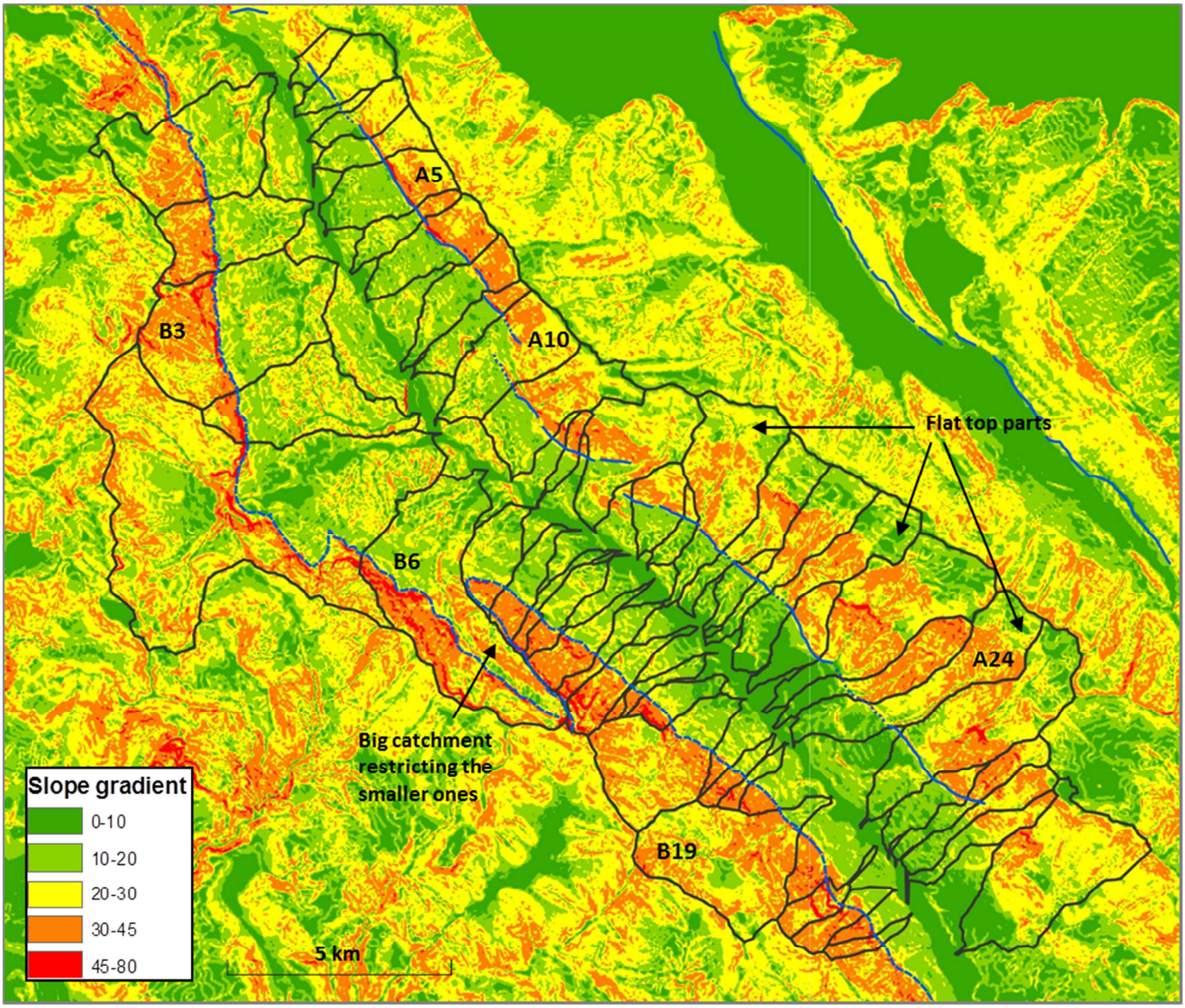

Figure 25. Visualizing steepness of the slopes and the surrounding areas, given in degrees. The black polygons represent the catchment boundaries, and blue lines are the fault traces (both the active side faults and the old thrust fault on the other side) respectively. Comparing this to the long profiles of each watershed helped to further understand the changes in the profile. Note how some of the streams are visible in this map as incised channels.

3.5 Long profiles

The two sides of the valley will be discussed separately. The Liri fault side (A-side) is divided into two sections that had distinctly different long profiles along the tributary channels.

3.5.1 The Liri fault side

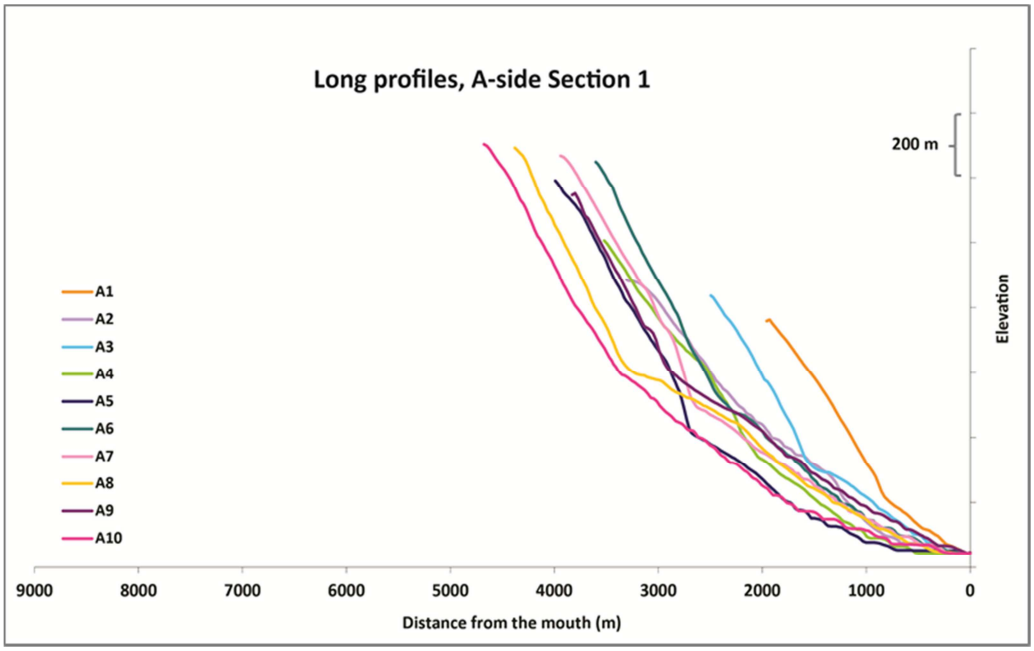

Figure 26. Long profiles of the streams from the northern part of the Liri fault side.

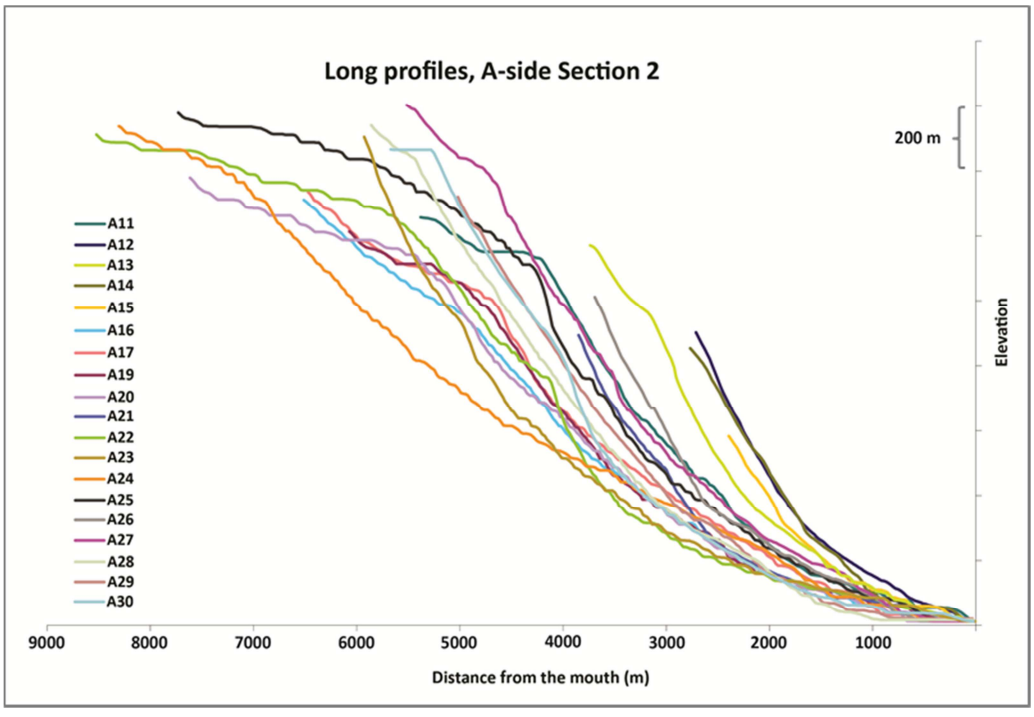

Figure 27. All the long profiles further south on the Liri fault side.

The Liri fault side is dominated by shorter channels in the northern end, referred to as A-side Section 1, compared to the channels further south, referred to as A-side Section 2.

Figure 26 and Figure 27 show all the long profiles studied on the fault side. The major differencies in the profile shapes between these two sections are visible in these figures.

Figure 28 and Figure 29 show the long profiles and where the active segments of the Liri fault are located, in catchments that are crossing or are suspected to cross faults. The freehand drawn dashed lines in the geolgical map indicate what is meant by the latter.

The first ten channels on the active fault side (A-side Section 1) seem to have an obvious knickpoint at the fault (Figure 28). The long profiles are also relatively linear or even convex above the fault. These catchments are either < 3 km^2 in terms of their drainage area with a few bigger ones (A5, A7, A8 and A10), but the drainage area before crossing the fault is small in all of them (< 2 km^2).

The rest of the channels crossing the fault on this side (Figure 29, Section 2 channels) do not show an obvious knickpoint at the fault, marked again by the red dashed line. Instead, all the longest ones of them show a clear convex or flat part at the top with more or less abrupt change to a curve that becomes highly concave further downstream. These streams appear to be indifferent to the fault, i.e. no knickpoints are observed. Furthermore, they are incising downstream of the mapped fault because previously deposited hanging wall fans show evidence for erosion (see Figure 37).

The smaller ones (A12, A14, A15, A21, A26) in the same Figure 29 are also concave in form, but do have a subtle change in the long profile somewhere around the elevation for the marked fault (except for A12 that does not show any change). This change is not perhaps as visible in this figure because the bigger streams distort the smaller profiles. When looking at the original plot extraced from Matlab the knick is clearer. The fault location does not necessarily sit perfectly on the knickpoint, but this could be due to the uncertainty of the fault traces since the knick lies within 100–200 m from the fault, which is inside the error range that Roberts and Michetti (2004) announce in their paper. Considering this, also the lithological change from limestone to flysch would sit on the same elevation as the, since the fault traces coincide with the lithology boundary in the geological map.

The common feature for the bigger streams in Figure 29 is that they also gain a larger drainage area (> 2 km^2) before reaching the fault compared to the streams in the Section 1. This is obvious when looking at Figure 19 and comparing the drainage area of the catchment above the fault. The smaller streams in Section 2 (Figure 29) have smaller drainage area above the fault similar to the streams in the Section 1.

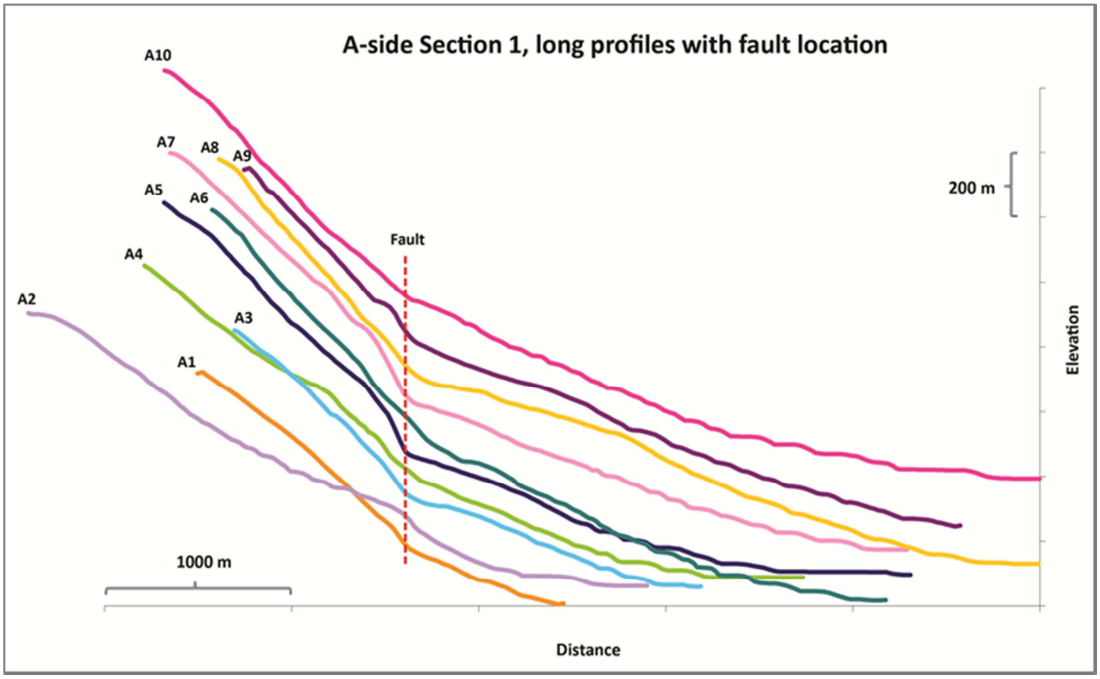

Figure 28. Showing the long profiles of the cathcments A1-A10 on the active Liri fault side (see Figure 12) with the fault crossing elevation indicated by the red dashed line. The profiles have been shifted both vertically and laterally to align the position where each channel crosses the active fault.

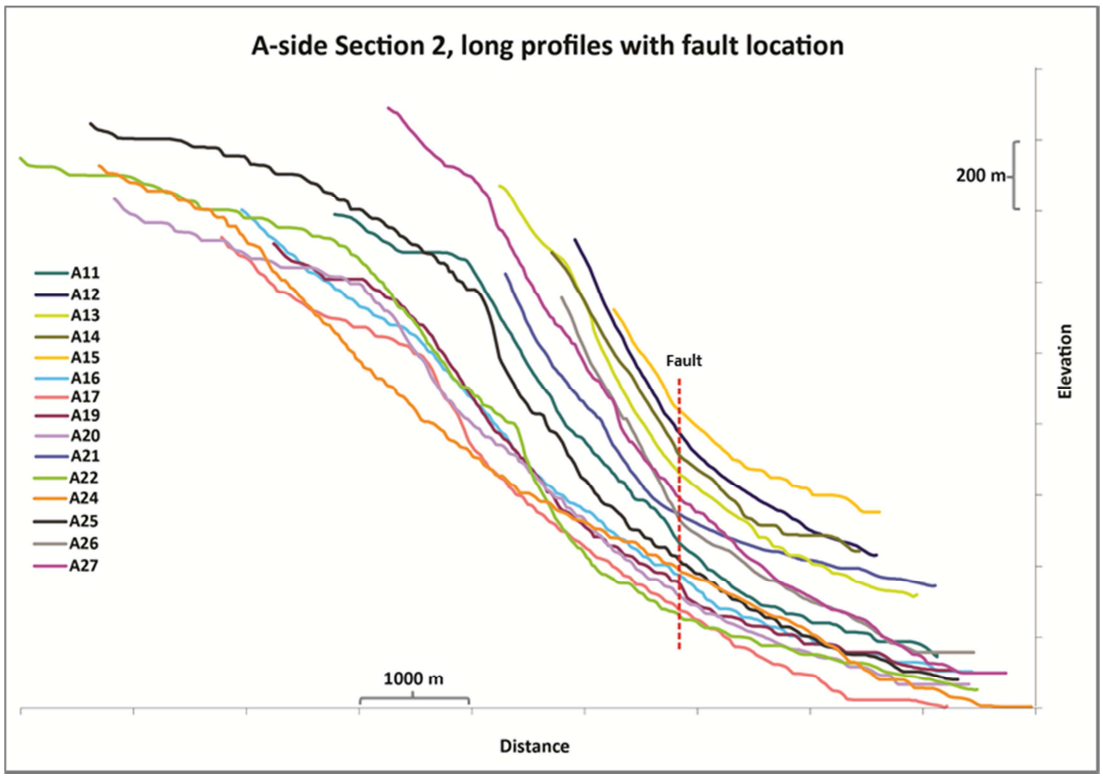

Figure 29. Further down the Liri valley on the active side, majority of the catchments grow in lengthand appear to be unresponsive to the fault (indicated by the dashed red line). Smaller channels do show a slight change around the fault, but exhibit still higher concavities than channels of similar length in the first section (see previous figure).

Figure 30 summarizes the observations from the active fault side (A-side) by comparing two different long profiles to the bedrock geology. As previously described, Section 1

streams (Figure 28), represented here by long profile A5, have a clear knick at the fault that also coincides with the lithological boundary between Jurassic limestone and Miocene flysch. These streams are also steeper above this contact in general, and shorter in length, similar to the shorter streams in Section 2. The longer streams from Section 2 (Figure 29), here represented by A17, extend further up into the Cretaceous limestone and have a knickpoint at this contact between the two limestones. These streams are more concave downstream from this point, and do not show any change in slope when crossing the fault at the boundary between limestone and flysch.

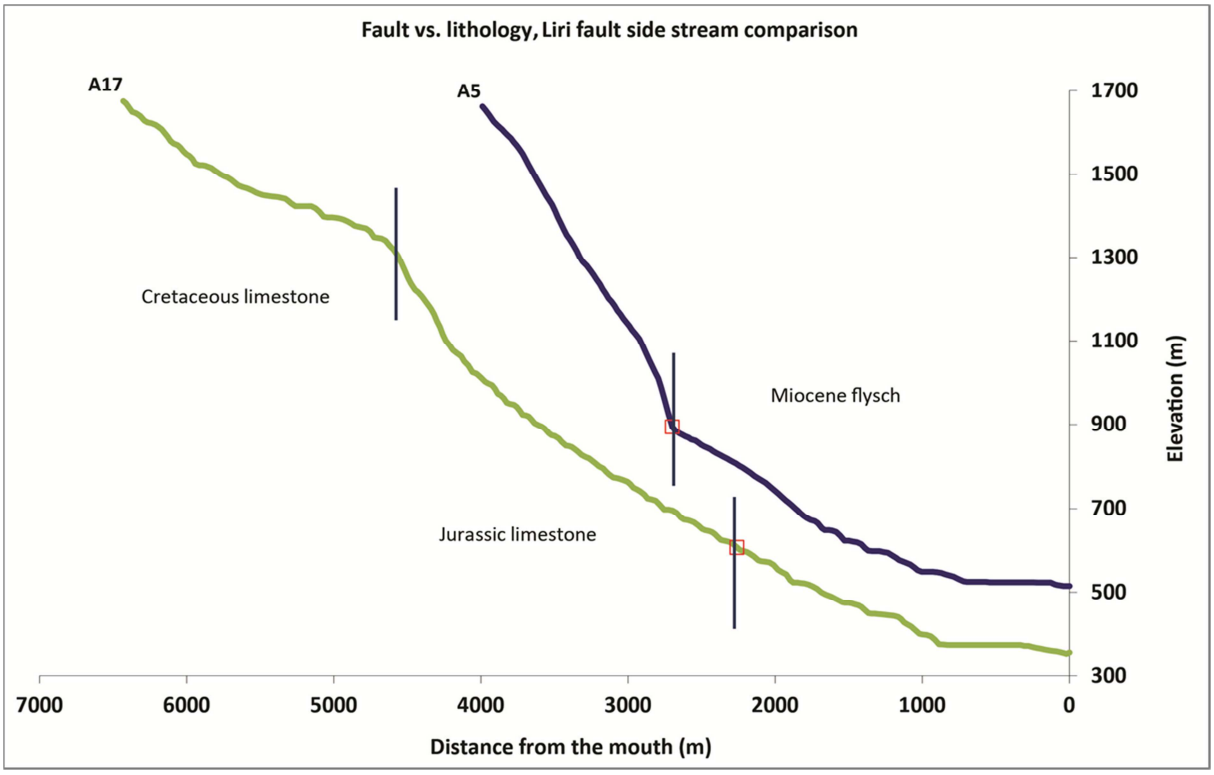

Figure 30. Comparing the streams on active Liri fault side, with A5 representing streams from section 1 and A17 from section 2 from the previous figures. The lithological boundaries are shown in dashed lines, and the fault trace as a red box.

3.5.2 The inactive side

The profiles from the other side of the valley (B-side) show more variation in shapes and sizes. It was not as easy to see trends between different sections, so the division for better visualization was done between large and small catchments, shown in Figure 31 and Figure 32.

All of these streams are either quite linear or have very irregular long profiles. This phenomena does not seem to be connected to the size of the catchment. Many of them also have more than one knickpoint on the profile (e.g. B5, B20), making them quite complex especially when visualised on the log-log plots.

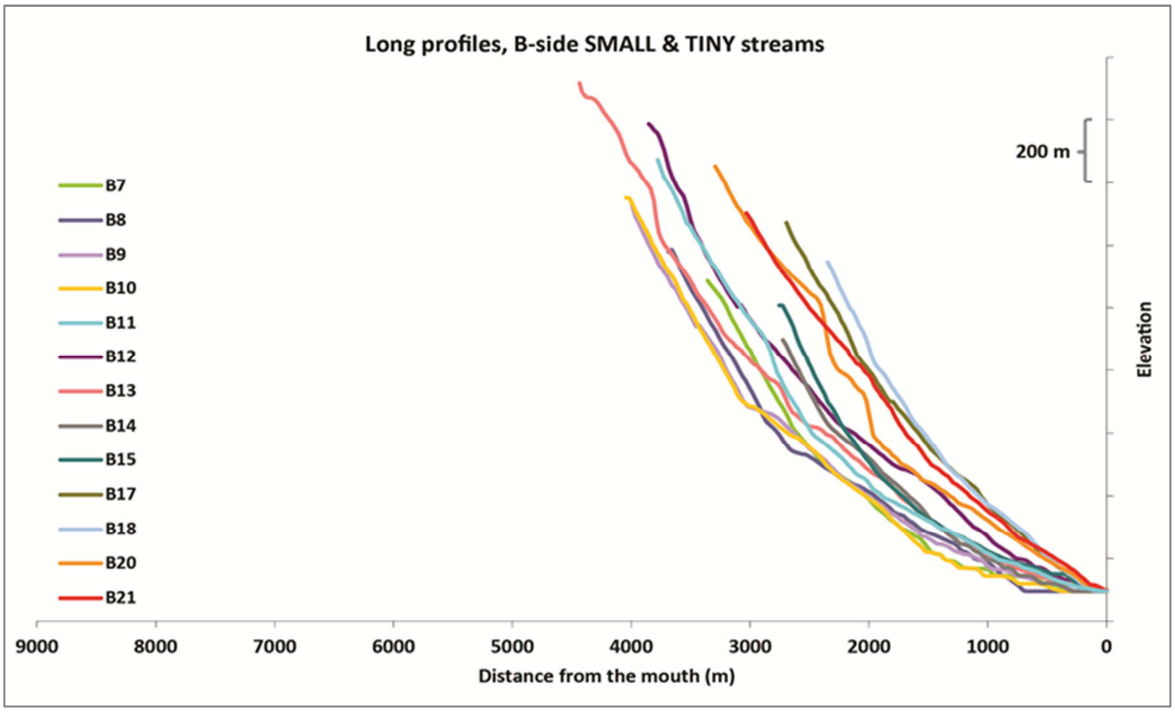

Figure 31. Displaying the small and tiny streams from the whole length of the inactive B-side.

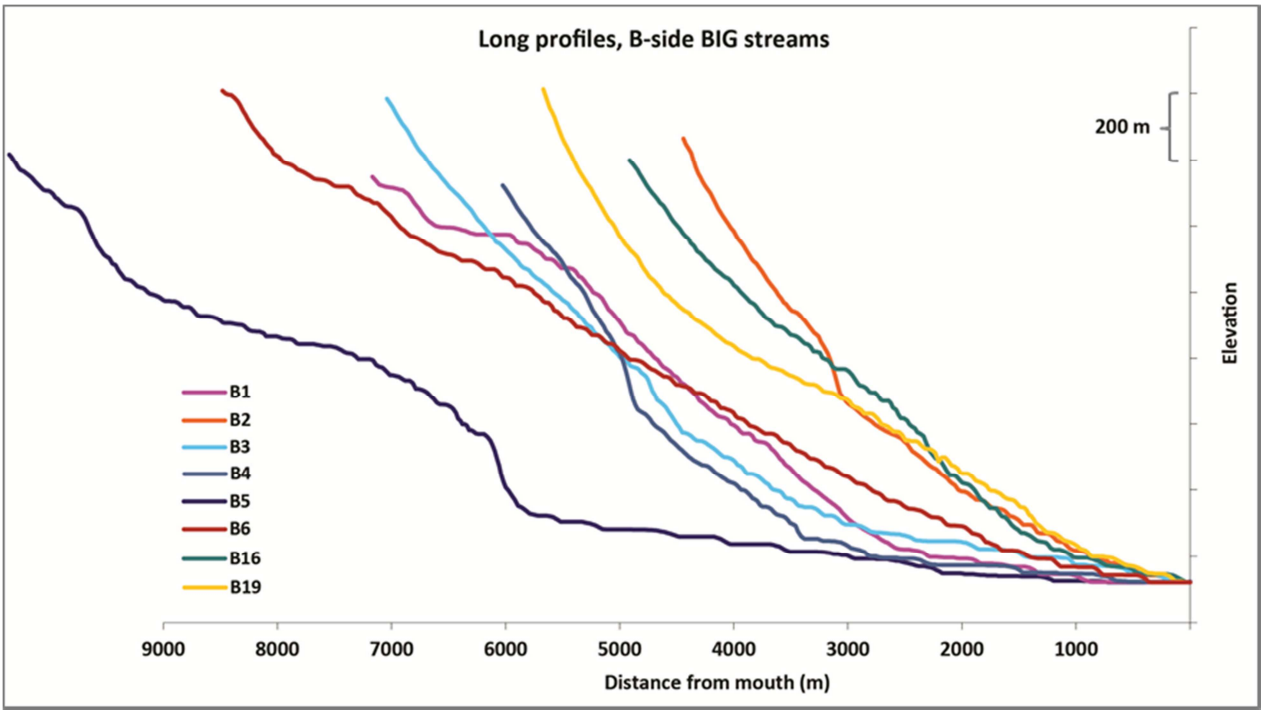

Figure 32. Displaying all the bigger streams on the inactive B-side. Note the great length of B5 in comparison to the other streams, and the variable forms of all the long profiles of these channels.

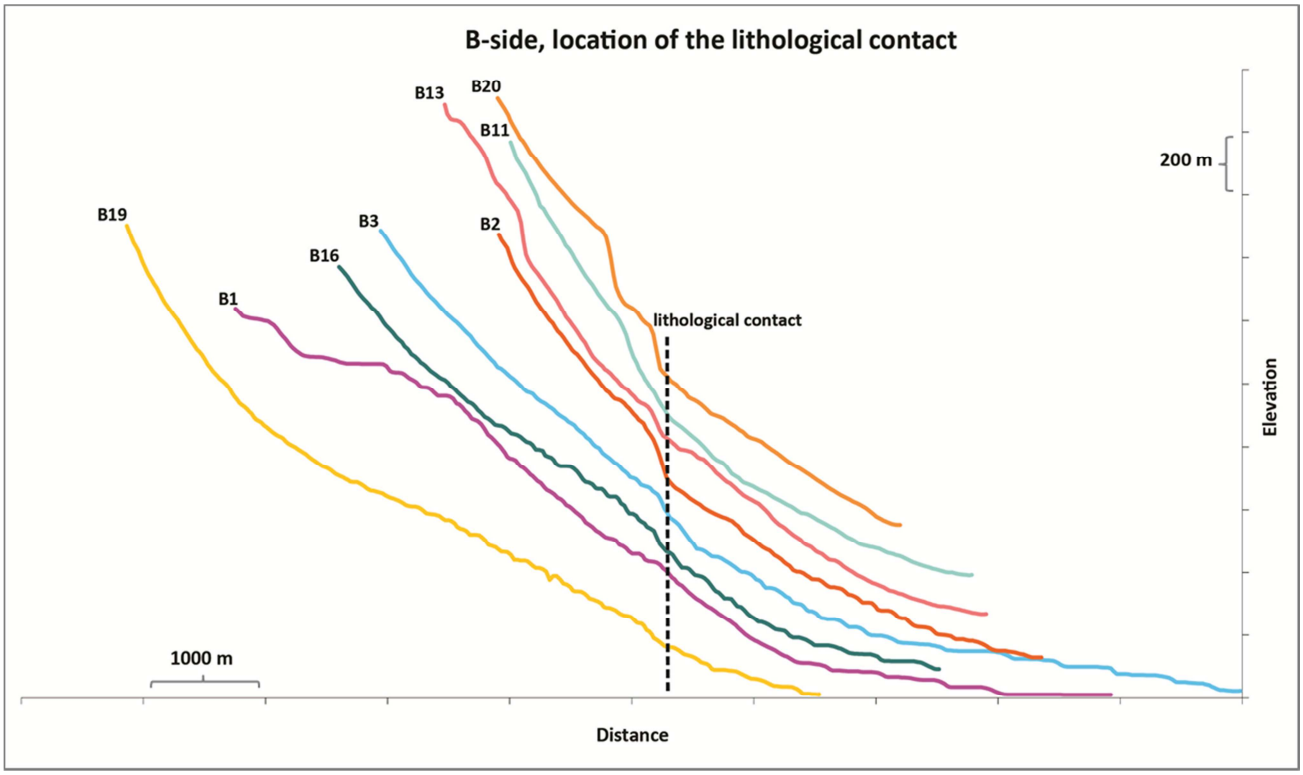

Figure 33. Selected streams from all the different size groups from the inactive B-side, lining up the profiles at the lithological boundary between limeston and flysch (the old thrust fault trace).

The streams on the inactive side clearly show a change in the profile around the lithological contact, as can be seen from Figure 33. If the lithological contact does not coincide exactly on the knickpoint it is most likely due to the unaccuracy of the geological map that was used in this study. As explained earlier (section 3.3), the contact was drawn following the slope gradient change from Figure 25, and this contact line is probably a rather coarse estimate of the actual location pointed out in the 1:100 000 geological map of Vezzani and Ghizetti (1998).

Especially the larger streams on the inactive side show more obvious change in the long profile at the crossing from limestone to flysch than the smaller ones. The tiny channels were often lacking a knickpoint at the inferred location of the lithological contact, but after more close examination of these channels in ArcMap it became clear that most of these channels have a knickpoint a bit further up that matches with the slope change, meaning that might be the actual correct place of the lithological contact instead of the less accurate line drawn based on interpretation of large-scale maps. Some of the streams that did not exhibit knicks at the lithological contact on the inactive side had eroded a deep gully visible in the slope map when zooming closer into these channels.

3.6 Final map with concavities

The map in Figure 34 shows the measured channel concavities in each catchment in relation to the active fault, published fault throw rates and bedrock lithological changes. This summarises the different features from previous maps and plots.

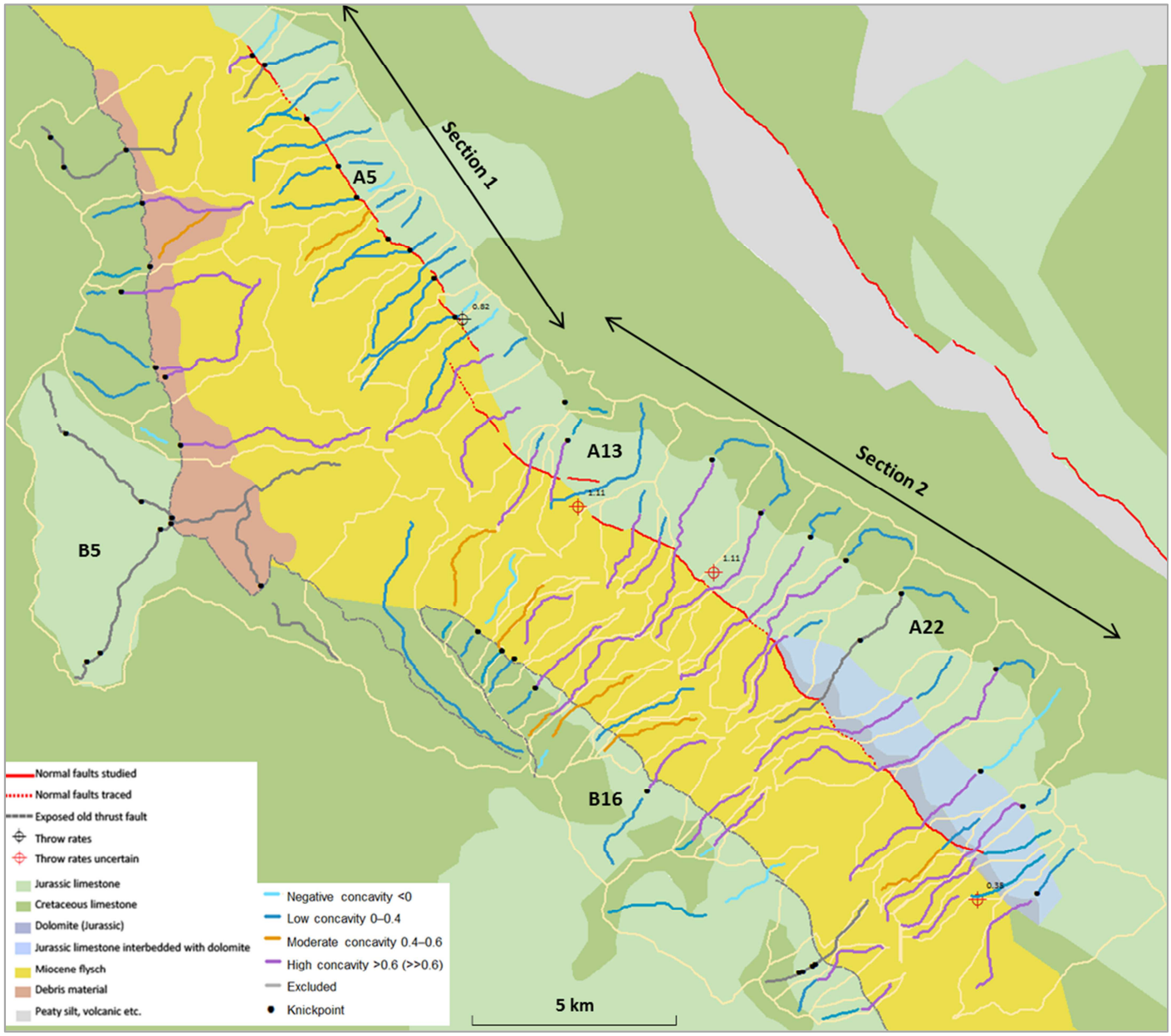

Figure 34. Final map with watersheds and studied streams inside them, compared to the changes in lithology as well as the fault. The grey streams were excluded from the concavity measurements because they were too complicated due to scattered data or with many knickpoints (black dots) on the profile, making the concavity extraction difficult.

The concavities shown as coloured streams are corresponding to the length inside the regression limits used in the concavity estimation for each long profile (see the plots given in Appendix A), and the stream lines may therefore have some gaps depending on the lengths of these chosen regressions. As explained in the methods (section 2.2.1), the regressions were chosen this way because it is not always best to use the simplest and most common approach (e.g. Snyder et al., 2000) of using only one regression from top

of the catchment to the channel mouth, since many channels are segmented due to variations in lithology and/or uplift rate (Kirby and Whipple, 2012). Therefore, it is better to choose the regression limits separately for each segments in the log-log plot that have clearly different concavities.

The values for the derived concavity indices in Figure 34 can change dramatically between different sections of the long profile, sometimes giving negative or extreme (>>1) values. Some channels were left out of the analysis due to the complexity of them or bad data, as was explained in the methods. For easier comparison, the concavities were divided into four groups, indicated by different colours (see Figure 17, that also shows what these different concavity values would look like on a log-log plot). A range between 0.4–0.6 was used to express moderate concavities (indicated by orange colour) because channel concavities in a steady state normally plot somewhere inside this range (e.g. Whipple and Tucker, 1999).

3.6.1 Description of patterns in the final map

A clear change can be seen in the concavity results between the northern and southern ends of the Liri valley, corresponding to Section 1 and Section 2 as described above. When looking at the NE end of the study area, the concavities are low (values < 0.4) on the active fault side, referring to the channels in Section 1 (see the long profile plots in Figure 28). These low concavity values are located where the fault throw rates were double-checked by Papanikolau et al. (2005). Most of the active side streams in this northern (Section 1) part showed a knick at the fault but had still low concavities upstream and downstream from the fault, despite the lithological change. On the other hand, the inactive side streams of the same part of Liri valley also show low concavities on the limestone part of the profiles, but below the knickpoint they are characterised by high concavities where the lithology changes to flysch. Some of these streams on B-side (e.g. catchment B3) are also the ones that show signs of fairly recent debris flow activity in their upper reaches. A key difference between the two sides of the valley here is that they have a different limestone lithology: on the active fault side (A-side) is Jurassic of age, whereas the inactive side is Cretaceous (B-side).

Moving to further to the SE towards the center in the study area (start of the Section 2 in Figure 34), the streams along the A-side begin to show a change: they express high concavities at their lower reaches and there are no knicks on the profiles at the fault trace despite the fact that the lithology changes between limestone and flysch – the profiles are smoothly running over this boundary. If there are knickpoints, they seem to

coincide with the lithological contact between the different limestones instead, a long way upstream from the fault.

The inactive B-side at the center part of the valley is dominated by the large catchment of B5, with a drainage area over 30 km^2, that was left out of the concavity analysis. Another large catchment, B6, with a low concavity along its whole profile, appears to be controlling the morphology of the adjacent channels (up to B12). All of these have a short and relatively steep lower concavity part on the limestone and the concavity increases on the flysch part, except for the B8 that becomes convex towards the end.

It is hard to compare the channels on both sides in the center part of Liri valley because of the different morphologies of the catchments. But on the active Liri fault side this part could be characterised as a transition zone where the channels become less influenced by the mapped fault. This is also a part of the valley where the fault throws are less well constrained. Based on the fault trace along this part, the last catchment (A13) drains through a discontinuity in the mapped trace of the Liri fault, a pattern that could indicate a relay ramp between two fault segments. However, it is difficult to determine whether this pattern is simply a result of poor exposure of the fault in the field.

In the southern part of the A-side, the channels exhibit in general high concavities (> 0.6, up to > 1.0) continuous across the fault trace and the limestone-flysch contact without any change in the long profile. The smaller catchments also imitate this low concavity upper reach and change to a high concavity further down, but none of them seem to have a change in slope coinciding with the fault trace, but rather upstream or downstream from it. As mentioned when discussing the long profile forms, this subtle change could also be at the change between lithologies, that is just not recorded properly when making the geological map that might include errors between the actual lithological boundaries. Any apparent changes in the concavities of the bigger channels, as well as knickpoints, coincide with the Jurassic-Cretaceous limestone contact. These big catchments have well-developed, clear channels, and even though the majority of them are covered in vegetation, the southernmost catchments located on the highly dolomitic limestone exhibit recent debris-flow-style erosion (Figure 35). At the very end of this Section 2, where the mapped fault trace ends, the streams still act the same way with a high concavity in the lower parts (A28-A30 in Figure 34).

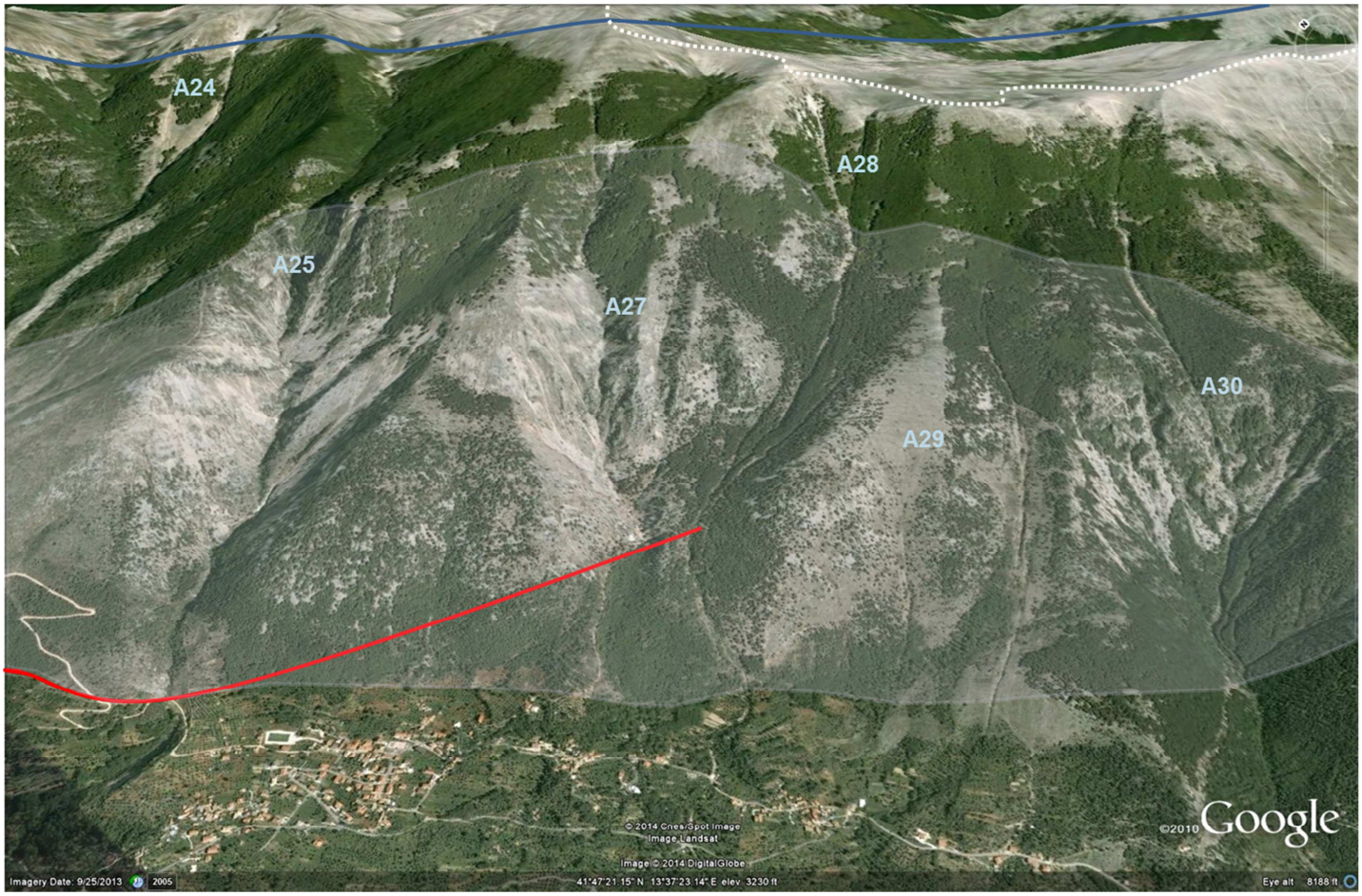

Figure 35. Satellite image from Google Earth of the catchments on the Liri fault side that have indications of recent erosion, marked by non-vegetated regions close to the catchment labels. Note the habitation for scale. The red line indicates where Roberts and Michetti (2004) have traced the fault. The blue line shows the lithological boundary between the two limestones, and the shadowed area where the more the highly dolomitic limestone is. The dashed white line represents the drainage divide.

Along the inactive B-side at this southern of the Liri valley the catchments become more similar to the northern of the B-side, with low concavity upper reach and higher concavity further down. There are differencies though: knickpoints are becoming more an exception than a rule. If there is a knick it is not necessarily as obviously located at the lithological contact, but this could be due to the uncertainty in the position of the lithological boundary inferred in this study, as described earlier when discussing how the geological map was constructed. And if there is a change in concavity, it appears to be more in the upper part of the channel and possibly related to change between Jurassic-Cretaceous limestone rather than limestone-flysch.

3.7 Final map with normalized steepness indices

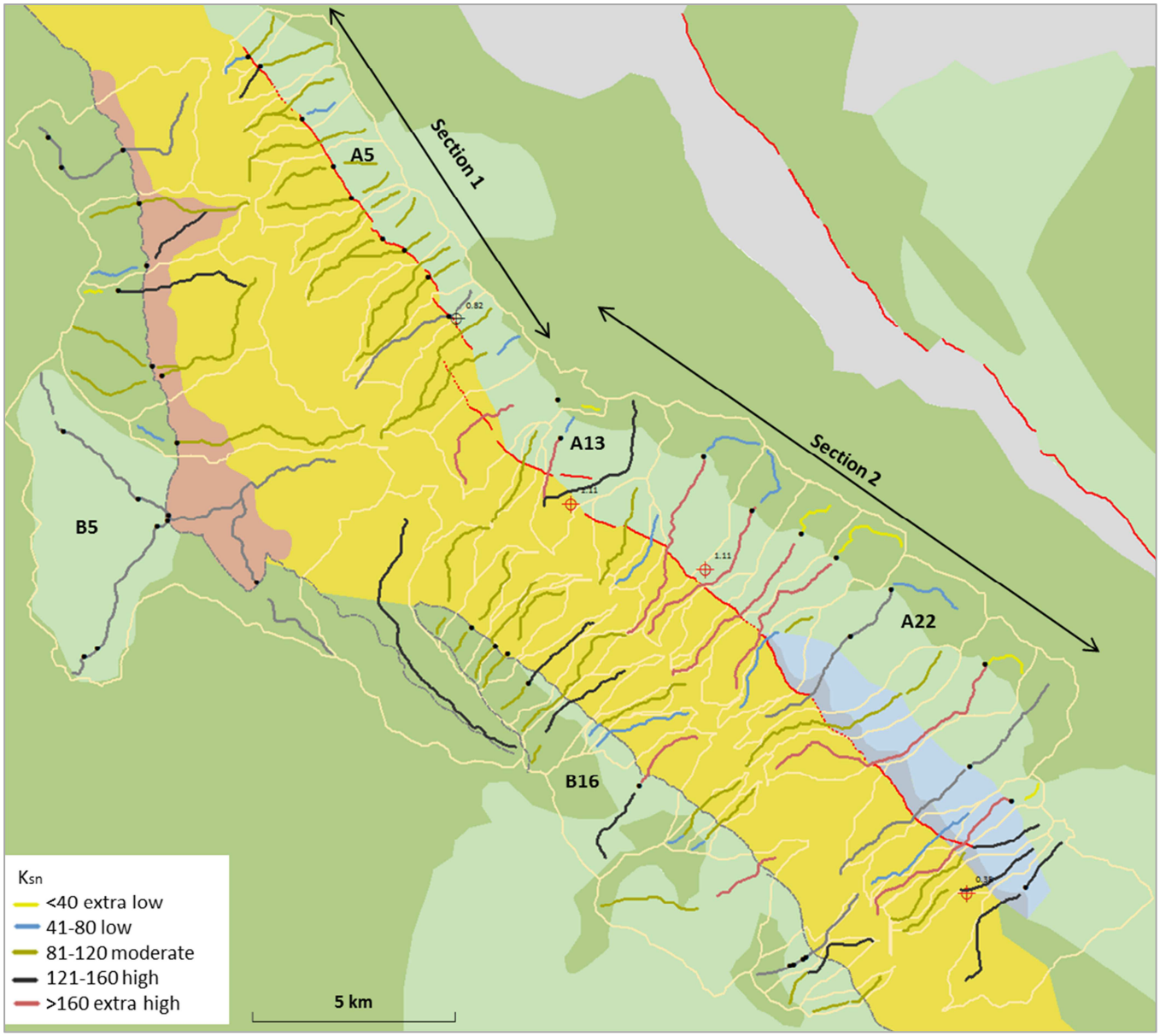

Figure 36. Depicting the normalized steepness indices for the same regression limits as in the concavity map Figure 34. The grey streams are the more complicated ones that were left out of the slope-area analysis. Note that the streams A9 and A25 are also represented in grey because some error in the data prevented the extraction of k_{sn} from them. The geological map is also shown, with the same legend as in Figure 34.

The map presented in Figure 36 plots the normalized steepness indices, which vary from 20 to 250 between the channels in the Liri valley. The grouping shown in the key was chosen based on an analysis of the range and frequency of the k_{sn} values obtained, and was necessary for simplifying and revealing potential trends. Due to the wide range of k_{sn} values, using a smaller range for each grouping would have resulted in a rainbow of colours obscuring any correlation between adjacent streams and between the underlying geology. In the chosen grouping (see key to Figure 36) the channels show some consistency between the different parts of the valley in relation to each other, as in the concavity map (Figure 34). The usefulness of this map will be discussed later.

Channel steepness index is a measure of stream gradient normalized to a specified drainage area (Wobus et al., 2006). Some studies (e.g. Densmore et al., 2007) have calculated the reference concavity separately by first finding the mean concavity from all channels in the area and using that as a reference concavity as a function for the k_{sn}. Duvall et al. (2004) had done an experiment with different reference concavities from 0.2–0.7 and found that the ratio of normalized steepness index between two stream did not change radically (< 2%). Therefore, despite the k_{sn} values being really different when choosing different θ_{ref} , if one reference concavity is consistently used the k_{sn} results are comparable. This study was more interested in comparing the spatial variations in stream characteristics relative to each other, not in trying to specify absolute values for steepness indices. Therefore, the chosen value of 0.45 for reference concavity still shows the relative steepness ratio in the Liri valley, although the θ_{ref} used is not the average concavity of the area.

One problem related to the accuracy of normalized steepness indices is in their sensitivity to how the regression limits are chosen. Even small changes in the chosen regressions led to quite large variations in the resulting k_{sn} values, e.g. from 130 to 153 depending on the regression limits. A reasonably large range inside which the k_{sn} values were given in the final map (Figure 36) was used in order to reduce this effect.

3.8 The Liri river and valley profile analysis

Since the Liri river can be expected to set the overall base-level in the whole valley, including the hillslopes, an analysis was done on the Liri river as well. A raw-elevation long profile was extracted the same way as explained earlier for the other catchments, in the interests of finding out whether there are any apparent knickpoints that might reveal something more about what is happening in the Liri valley on a larger scale.

The Liri river is a meandering, low-gradient perennial river that runs on the footwall side of the Liri fault. Figure 38 shows how the studied catchments of this project are located on a reasonably smooth part of the long profile, downstream from the apparent knickpoint. Locations of Section 1 and Section 2 of the A-side are indicated by yellow and orange colours. Based on the changes in the topography in the valley bottom seen in Google Earth, the river appears to have changed its course in the northern part of the study area, leaving behind small ridges in the middle of the valley bottom flysch.

Previous field work done in the area, as well as Google Earth images and the DEM itself indicate that the Liri river is currently incising. This incision is the result of the regional

uplift of the Italian peninsula with a rate of approximately 1 mm/ year (Mancini et al., 2007). The rate of incision upstream from the coast, i.e. the Liri river must be something < 1 mm/ year. To find out how much incision has occurred, the most prominant cemented Pleistocene alluvial fan (Figure 37) was used to measure this. This particular fan has been abandoned by the stream that fed sediments to it, but later changed course and is now running on the side of the fan (catchment A24). In addition, this fan seems to have been eroded by the Liri river, indicating that the river was located at a higher elevation in the past. It seems likely that much of the incision occurred during the Holocene, although without a precise age for the fan surface it is not possible to place tight constraints on the timing and thus the rate of the incision.

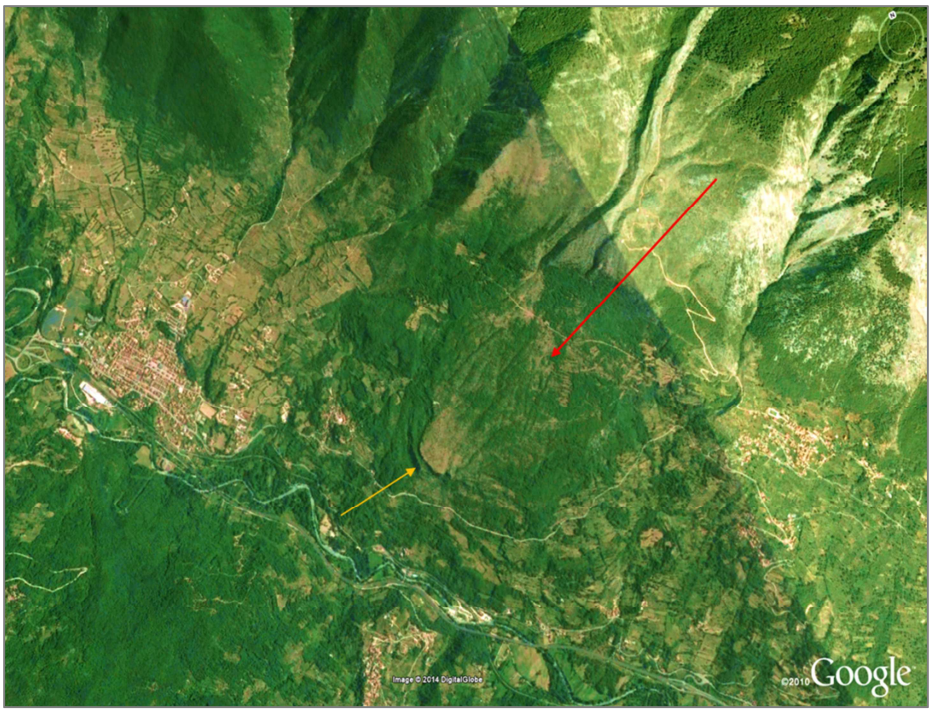

Figure 37. Google Earth image of the cemented Pleistocene fan indicated with the red arrow. The yellow arrow is pointing at the eroded end of the fan. The meandering modern-day Liri river is also visible.

Figure 38 shows the long profile of the Liri river, and visualizes how the incision depth was calculated (see inset to this figure). The location where the valley cross-section was taken is shown in Figure 39. Projecting the top slope of the fan to the center of the valley where the Liri river is located today, is at an elevation of 425 m. This gives a minimum incision depth (h_1) of 100 m as the modern river bed is at an elevation of ~325 m. This minimum estimate implies that the fan was graded all the way down to the Liri river, that the surface slope of the fan is constant and that the position of the river has not shifted laterally. For an upper limit estimate, the top of the fan where the upper eroded edge is located at present (525 m), was used to calculate the maximum depth of incision,

because it is not known where the river was located in the past. This gives an incision depth (h_2) of 200 m.

In order to visualize how far the incision of 100–200 m would approximately have proceeded upstream along the valley, the contour lines for 425 m and 525 m were drawn in ArcMap and shown in Figure 39 with green and purple colours. These indicate roughly where the base-level was before the river incision.

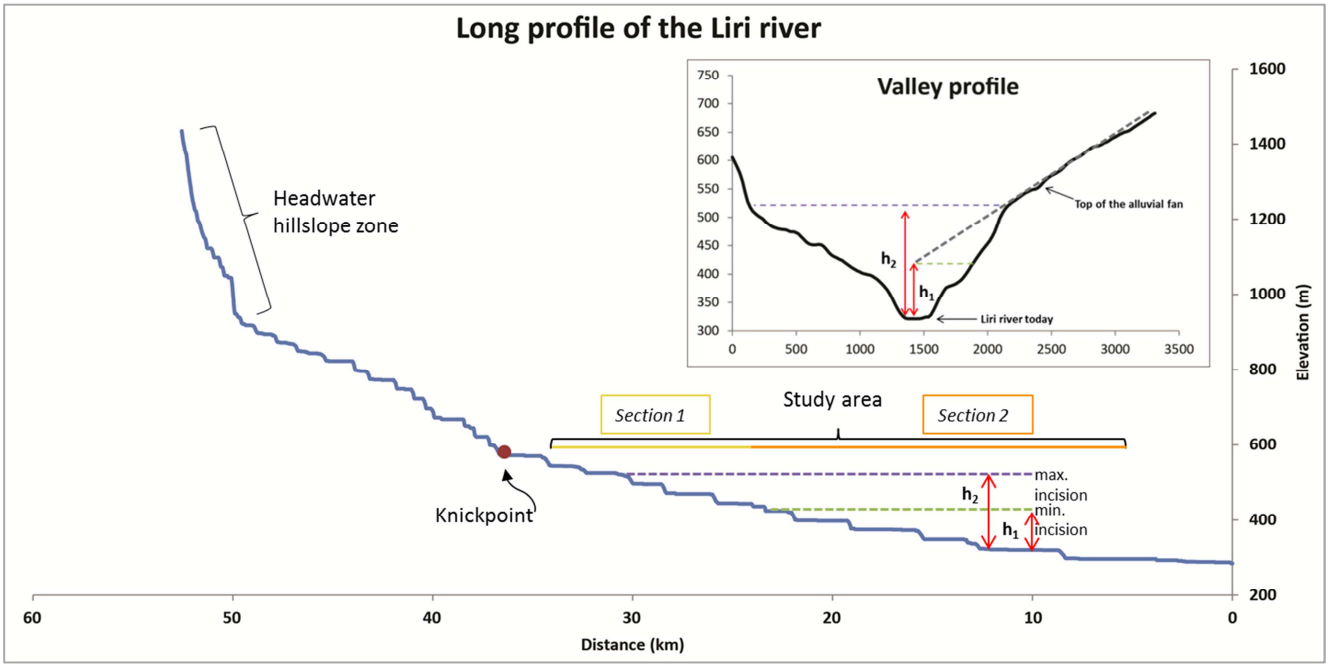

Figure 38. The raw elevation profile along the Liri river, and an explanation of how the incision height was calculated using the fan surface (inset). See Figure 37and Figure 39 for location of the fan. The inset depicts how the minimum and maximum incision depths were measured, starting elevations before the incision shown in purple (h_2) and green lines (h_1) respectively and corresponding to the contour lines marked in the map view shown in Figure 39. These elevations are also plotted next to the long profile in the main part of the figure, to show where they would sit in relation to the current river level and where they intersect the modern river upstream.

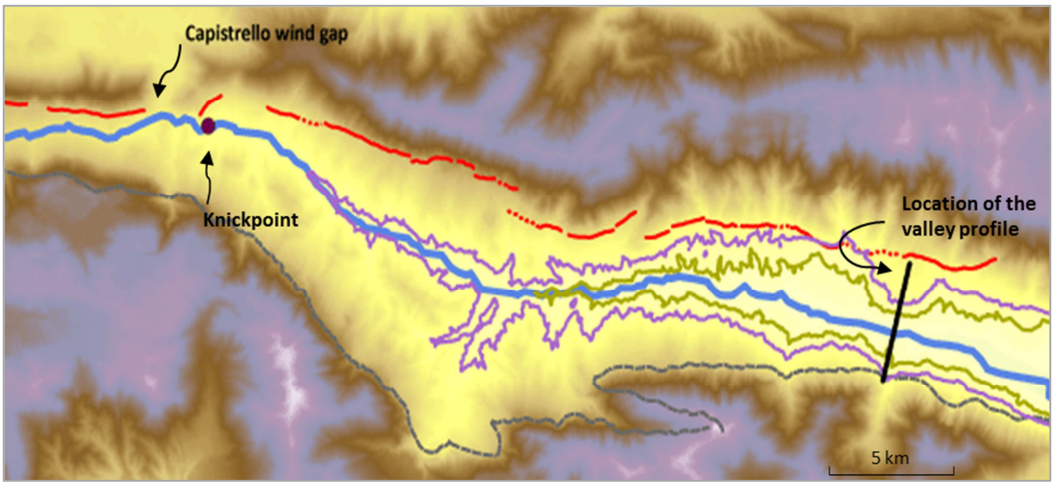

Figure 39. A topographic map of the Liri valley, showing the Liri river in blue with its major knickpoint and the location where the valley profile in Figure 38 was taken. The purple and green colours represent the contour lines at 425 and 525 m in Figure 38, marking the elevation before the incision. Note also the location of the Capistrello wind gap.

Chapter 4 – Discussion

What are different concavities related to, and what can they possibly tell us about erosion or tectonics? This is the main launching point for the discussion about the catchments in the Liri valley, framed by the major change in the climate conditions and the tectonic influence. Some further uncertainties of this analysis, as well as how those uncertainties were treated to minimize their influence are explained. The uncertainty of what is actually recorded when trying to reveal channel morphology based on a digital elevation model is discussed, in addition to facing the question how much of the concavity results of these small catchments, that were expected to be dominated by debris flows, were actually shaped by past flow regimes. Furthermore, the effects of the Liri river incision are considered, and the activity of the Liri fault is debated.

4.1 Data analysis and uncertainties of the method

An effect of the data scatter was that extreme values of concavities sometimes were inferred for some of these channels. This appeared once more to be a problem that occurred when there were too few data points in the log-log plot for it to be able to define the regression profile in a way that would describe both the profile shape and the log-log plot in a rationalistic manner, an example of which is given in Figure 40. In these channels it was hard to make a decision whether to use the concavity value that seemed ridiculously high, based on two data points, even though the computer program shows in the long profile that it supposedly describes that part of the profile very well as the regression blue and original red long profile lines are almost identical (Figure 40). This was one reason why the exact concavity values are not presented or given too much attention in this thesis but rather a range is given, e.g., 0.4–0.6. Showing the exact values on plots (e.g. $\theta = 0.42$) made very little sense. And choosing to take only one regression on that part of the plot that seemed to have the best power-law fit, and letting it to be the only result presented and saying it describes the whole long profile, felt like manipulating the results.

If examining the long profiles' shape only, they were often very smooth and unchanging at first sight especially in the smaller channels, but the log-log plot showed variation that subsequently was also visible on the profile. The method was applied first on the active fault side of the valley (A-side), where all channels were treated carefully, even the smallest ones, and regressions were chosen from a log-log plot following each apparent trend fitting the original long profile more or less. This same procedure was then used

on the other side, where these changes were perhaps not as visible in the log-logs or long profiles (see e.g. catchment B12 in Appendix B, facing the problem whether to choose one or two regressions). In order to be consistent, this method of focusing on the changes in the log-log plot was kept so that both sides were treated equally. The author of this study still admits there are profiles that perhaps should have been treated differently – either a more detailed analysis could have been done, or tried to fit the regression better – but whether this would have changed the overall patterns is still doubtful.

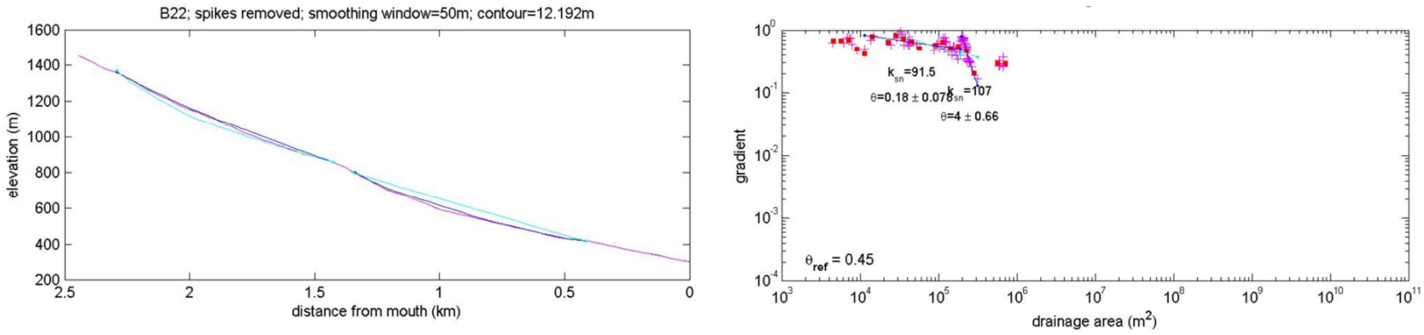

Figure 40. The tiny channel of B22 representing an example of extreme concavities that occurred when extracting the concavities. When the regression (dark blue line) describes nicely the form of the original long profile, on the log-log plot of the same distance is described as θ=4, which is extremely high and hardly close to the truth of how concave that particular profile is. When choosing a more linear line from the log-log plot (including the last two data points, the resulting concavity was low (< 0.4), but the regression did not sit on the long profile.

In the end, these are all problems related to working with log-log plots which record the data over orders of magnitude. Small changes on a log-log plot can reflect vast distances in the actual profile. When adding the scatter of the data to this problem, finding the best fit for the power-law sometimes becomes quite challenging. The log-bin averaging used in the stream profiler tool is helping to reduce the scatter, by gathering together the data points having the same drainage area, but the binned data points can still be scattered in a way that makes power-law extraction difficult.

One way to reduce the scatter effect is to use smoothing of the profile, which can be defined in ArcMap before extracting the profiles. The higher the smoothing value the smoother the long profile will become, which is also apparent in the log-log which shows less scatter. The problem when working with small catchments especially is that when adding too much smoothing the small changes in the long profile will disappear. Thus, a smoothing window of 50 m was used in this study, which was helping to clarify the trends a little bit in the log-log plots while still keeping the original shape of the profile, similar to if working with a raw-data profile without any smoothing.

4.2 Longitudinal profile form & concavities – what is recognized by studying fluvial channels

A typical stream profile is a concave longitudinal curve that captures alterations in the hydraulic factors along the stream from the drainage divide all the way down to the base-level. When there are no sudden changes in the profile, i.e. steep parts or abrupt steps, the streams show usually a gradually concave-up curve that is described by Equation 1 as explained in the introduction.

If the long profile has sudden steep parts, or is deviating from a typical concave curve, it can reflect changes in lithology or rock uplift rate (Snyder et al., 2000; Kirby et al., 2003). Therefore, overlaying the parts of the streams that display different values in steepness or concavity indices with important lithologic contacts is a useful method in determining whether these changes correlate with lithological boundaries instead of a tectonic signal (e.g. Hack, 1957; Kirby et al., 2003). It is still important to remember that lithology is not the same as rock properties: a well-cemented sandstone can behave stronger than weathered granite, and the quality of one unit can vary along strike (Wobus et al., 2006). All in all, if lithological boundaries are detected corresponding with the knickpoints in channel gradient, it can often rule out changes in rock uplift rate as the cause for the sudden steepening.

The concavity index (θ) in steady state bedrock river profiles is constant if rock uplift rate, climate or substrate lithology are uniform along the length of the channel (e.g. Whipple and Tucker, 1999; Kirby and Whipple, 2001; Wobus et al., 2006). If there are any systematic changes downstream in uplift rate or erodibility (e.g. sediment supply and cover), the concavity index might change, for example, if uplift rate is increasing downstream concavities will be lower, and decreasing uplift rate downstream will lead to higher concavities (Whipple and Tucker, 1999; Kirby and Whipple, 2001).

Whipple (2004) has summed up different river profile concavities together with typical perceptions of what they are related to. Referring to different studies listed in more detail by Whipple (2004), the general key conclusions from the identified concavities reflecting different geological conditions are:

- Low concavities (< 0.4) are related to short and steep drainages significantly shaped by debris flows, or downstream increases in either incision rate or rock strength, usually in the presence of knickpoints.
- Moderate concavities (0.4–0.7) can be associated with actively uplifting bedrock channels with invariable substrates going through approximately constant uplift.

- High concavities (> 0.7–1) are observed either when rock uplift rate or rock strength decreases downstream, at a downstream changeover of conditions to fully alluvial, or disequilibrium conditions resulting from a temporal decline in rock uplift rate.
- Extreme concavities (negative or > 1) are associated with steep knickpoints caused either by distinct along-stream changes in substrate properties or by spatial or temporal differences in rock uplift rate, as well as transitions from incisional to depositional conditions.

The interpretation of concavities from debris flow streams are often disregarded with simply stating that fairly linear, low-concavity values in catchments usually imply the dominance of debris flow erosion in that part of the channel (e.g. Montgomery and Foufoula-Georgiou, 1993; Stock and Dietrich, 2003). Most work done on debris flow power-law has mainly been concerned with the scaling-break at the upper end of the log-log plot power-law relation in Equation 1 (e.g. Stock and Dietrich, 2003). It has been suggested channel incision by debris flows produces linear, low-concavity channel profiles (Montgomery and Foufoula-Georgiou, 1993; Howard, 1998; Stock and Dietrich, 2003). Other authors that have used long profiles and log-log plots for studying debris flow dominated channels show their concavity values to fall mostly somewhere between 0.3 to 0.6 (Densmore et al., 2007). Since so little is known about concavities related directly to debris flows along the whole length of a channel, and what they eventually might imply about tectonics, this study will simply compare these in relation to what is known from studying rivers. This does not mean the concavities in this study are necessarily fully explained by this comparison, but at least it can help place it in some kind of context in relation to what the possible controlling factor behind the erosion in them could be, or possible linkage to tectonics.

4.3 Concavity trends in the Liri valley

The smallest catchments not reaching to the drainage divide are left out from the discussion, mainly because they are either expected to be controlled by the adjacent catchments, or are suspected to be artificial catchments created in the extraction process in ArcMap.

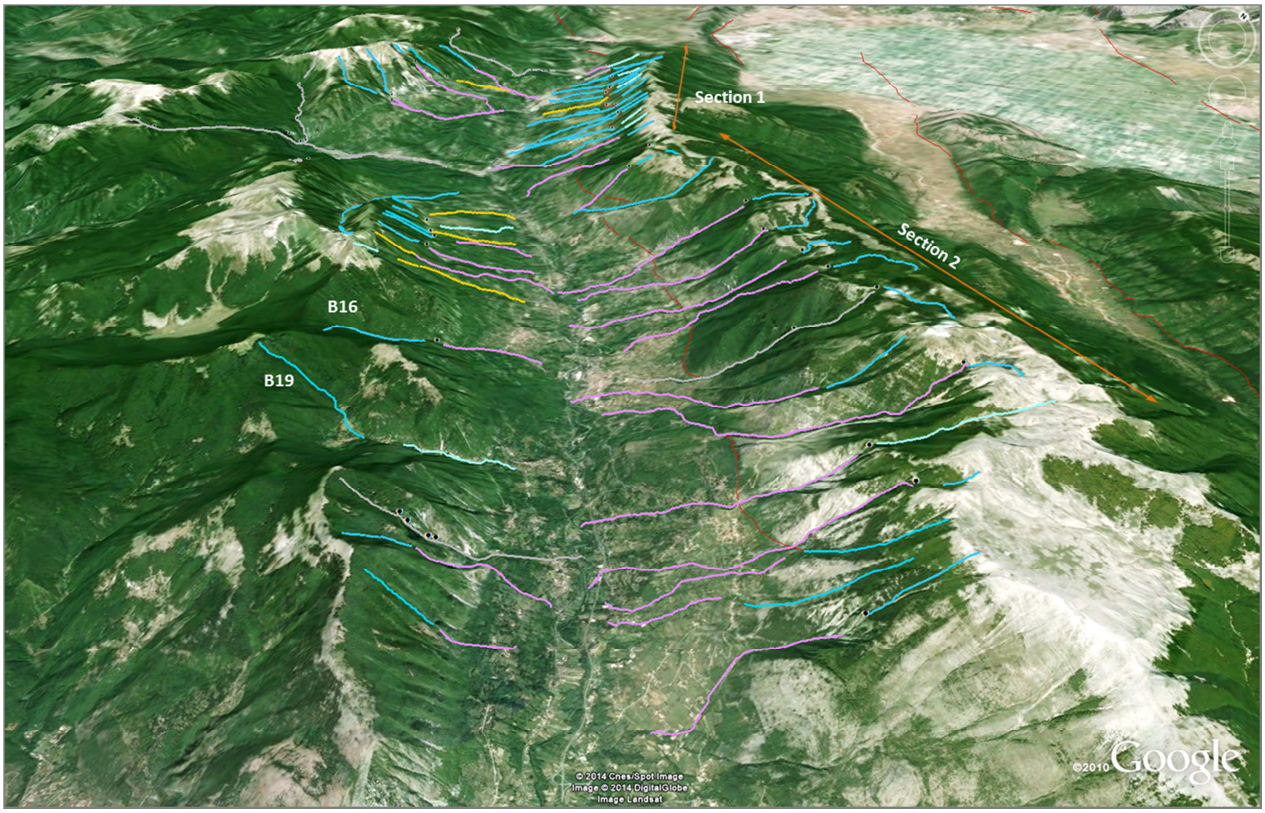

Figure 41. The extracted channel concavities for the Liri valley in Google Earth, showing only the catchments reaching up to drainage divide.

In the result section the extracted channel concavities were presented, and are once more visualized *in situ* in Figure 41 after importing them to Google Earth. The most striking feature of these concavities is that hardly any of them fall into what is expected to be a ”normal” concavity of 0.4–0.6 (represented by orange colour) for streams in erosional steady state. When looking only at the channel reaches on the limestone (i.e. disregarding the valley bottom), the majority of the smaller channels on both A- and B-side exhibit low concavities as could expected of such steep short parts of the drainages mostly dominated by hillslope processes such as debris flows. Most of these same catchments also show a change in concavity to a higher value when moving to the valley bottom flysch, which for some cases is likely to represent the depositional part of the catchments before joining the main Liri river, but in some cases it might simply reflect the change in the erodibility of the bed becoming easier in the flysch.

The second clear feature is the high concavity values of channels that extend far above the fault in the bigger A-side Section 2 catchments. In these catchments, a low concavity part is located at the top close to the drainage divide, separated by an obvious knickpoint where the limestone properties change (Jurassic vs. Cretaceous limestone), and from there on downstream a much higher concavity that does not change when crossing the Liri fault. Double-checking the regression limits for these concavities making them extend only to the fault did not change the results: the concavities were still high (Figure 18).

These two marked differencies on the A-side: low concavities in smaller catchments (meaning all catchments that have not gained much drainage area when meeting the change in lithology from limestone to flysch at the Liri fault) and the higher concavities of the bigger catchments, could be explained by the increase in the drainage area. If drainage area is small, the discharge will also be smaller and therefore erosion is most likely to be connected to hillslope processes, i.e. debris flows characterized by low concavity. As the drainage area grows, the effects of increased discharge can be expected to grow as well, leading to more fluvial dominated processes and in general higher concavities. At greater drainage areas the channels could be expected to have more freedom to adjust channel width and sinuosity, and likewise at smaller drainage areas they could have more variability in the portion of exposed bedrock, hydraulic roughness, and the relative influence of debris flows (Wobus et al., 2006). This could also explain why the smaller catchments (especially Section 1 on the A-side) exhibit a knickpoint in their profiles if hillslope processes at smaller drainage areas can be expected to be more sensitive to lithology changes.

Another feature of Figure 41 is the number of high concavity values, i.e., > 0.6 or >> 1. These are particularly obvious in catchments A11, A17, A20, A23, and A25 (see Appendix A for the extracted plots and exact concavity values). Various authors attribute high concavities to decreases in uplift rate downstream (Kirby and Whipple, 2001; Kirby et al., 2003) or temporal decline in rock uplift rate due to disequilibrium conditions (Whipple, 2004). Schoenbohm et al. (2004) have also recorded extreme (>> 1) concavities similar to those in this study, and link these to be a result of a major drop in base-level or climate triggered incision. These possibilities are thus discussed in the following sections.

The B-side catchments seem to be controlled more directly by lithology alone. Both small and bigger catchments change channel concavity and exhibit knickpoints where

the limestone and valley bottom flysch are in contact, and at least for the streams that were used in the concavity analysis, the larger catchments, too, exhibit a low channel concavity in the limestone part. This is the main difference between the larger catchments on A- and B-side: the A-side big streams have in general higher channel concavity values that extend also above the Liri fault/ lithological contact whereas B-side big streams do not exhibit higher channel concavities upstream from lithological change between limestone and flysch (if at all).

4.4 Steepness indices

The steepness indices have been shown to be directly proportional to rock uplift rates in a variety of landscapes (e.g. Snyder et al., 2000; Lague and Davy, 2003; Duvall et al., 2004). However, as the slopes are dependent on basin shape, small changes in the concavity index can cause great changes in steepness index (k_s), a normalized steepness index (k_{sn}) fixed to a certain reference concavity (Equation 3) is often used, allowing the comparison of the values. Knickpoint migration and subsequent changes in normalized steepness indices are widely used to interpret tectonics from river profiles, a short and consistent summary of how this is done, both the implications as well as the challenges, are presented e.g. by Whittaker (2012). However, studies made on transient landscapes show how interpreting these k_{sn} values as in steady state can easily lead to wrong conclusions that are inconsistent with the real tectonic situation, as e.g. Whittaker et al. (2008) have demonstrated in the central Apennines. This is particularly true if there is a small range of values of drainage area being considered, as is the case in this study.

In addition to differencies in rock uplift rate, the steepness indices can reflect other effects as well. These complexities include nonlinearities in the incision process, climatic erosivity, channel bed resistance, width scaling and basin hydrology, sediment flux, and critically if the channel is in changing or steady state (e.g. Sklar and Dietrich, 1998; Snyder et al., 2000; Whipple and Tucker, 2002; Whipple, 2004; Wobus et al., 2006). For instance, strong lithological contrasts have been noted to create differencies in steepness index that are comparable to ones associated with large gradients in rock uplift rate (e.g. Snyder et al., 2000; Duvall et al., 2004). Due to the possible influence of these complexities, the connection between steepness index and uplift rate can be expected to change depending on the geological setting (Wobus et al., 2006).

When extracting tectonic information from long profiles, the results from concavity and steepness indices will often give similar information, i.e. downstream transitions betweeen distinct steepness values will commonly show up also in different concavity

values (Wobus et al., 2006). Any change in the controls of k_s can also cause variations in the measured channel concavity (e.g. Wobus et al., 2006). However, the concavity data are often more useful for rough description of zones where uplift rates might be systematically changing along a profile (e.g. Kirby and Whipple, 2001; Kirby et al., 2003).

Considering the uncertainties involved with the normalized steepness indices, this study chose to present k_{sn} data, but not to use it any further. K_{sn} is shown here for completeness, since it is present in Equation 1. The k_{sn} results show that it is very sensitive to small variations (due to the logarithmic scale) in the selection of regression limits, therefore great significance is not placed on specific k_{sn} values. In addition, it is not possible to make direct comparisons with other studies without additional constraints available for this area needed for calibration. Because significant variations in measured channel concavities are present, using a fixed reference concavity to show variations in steepness becomes meaningless.

4.5 Uncertainty of what actually was recorded

The difficulty of really pointing a finger on what erosional process is the dominant one (e.g. debris flow or fluvial incision) in specific catchments was faced in this study, and has also been recognized by others (e.g. Lague and Davy, 2003). A typical change in power-law slope (Figure 4) is inferred to occur over a range of critical drainage threshold (A_{crit}) that typically varies between 0.1–5 km^2 and marks a transition from fluvial dominated processes to hillslopes where colluvial channels are regarded to be carved mostly by processes like debris flows (e.g. Montgomery and Foufoula-Georgiou, 1993; Sklar and Dietrich, 1998). In this study, over 50% the concavities that were included in the analysis on the Liri fault side and over 70% of the inactive side came from catchment drainage areas with data plotting totally inside or very close to 0.1–1 km^2. Majority of the profiles also show a change in the power-law slope trend inside this drainage area. If considering catchments with drainage areas < 5 km^2, the answer is 70% for both sides. Stock and Dietrich (2003) remark that debris flows may play a significant role in shaping the channel profile even in far larger drainage areas ($A \leq 10$ km^2) and lower gradients ($S \geq 0.03$–0.10) than the apparent change at ~1 km^2 in the slope-area plot normally suggests. On the Liri fault side all of the catchments lie under 10 km^2, and of the remaining 30% of the inactive side catchments included in the concavity analysis plotting above 5 km^2 only two catchments, B3 and B6, have total drainage areas > 10 km^2. As most of the catchments in this study have a drainage area below 10 km^2, and

show indications of debris flow type activity, it is at least very likely that in these channels erosion is happening through debris flow processes at present.

A study based on digital elevation models only without field observations inescapably leads to uncertainties that might affect the results. This study started out with an assumption that the catchments in Liri valley are debris flows, as they could be defined based on the drainage areas of the catchments alone (see section 1.3 in the introduction). Since there is no data from any of the catchments of the last time a flow event happened, vegetation is covering most of the channels obscuring clear debris flow channels if there even are some, and the morphology of the hillside itself does not confirm any channels or active fans in its vicinity, it is impossible to determine for sure that all of the catchments are debris flows.

Some of them could be just irregular hillslopes that are defined as ”catchments” in the watershed extraction process in ArcMap simply because the model assumes the water will drain this way due to the elevation grid. This might be the case in reality as well, that water flows in this pattern over that area, but it does not necessarily make it a debris flow – past or present. This kind of uncertainty is highlighted considering the smallest catchments on both sides of the Liri valley, especially those ones that do not reach to the drainage divide and have a small drainage area before reaching the valley bottom flysch.

Due to the fact that the area has gone through a major climate change (e.g. Zolitschka and Negendank, 1996; Allen et al., 1999 and 2000) at the end of the Pleistocene, not so long ago in the past on a geological time-scale, it is likely that some of the bigger catchments may have been influenced by fluvial processes, and that these later became less fluvially active when runoff decreased during interglacial periods when hillslope vegetation was re-established. Some of the largest catchments on the B-side (e.g. B5, B6, B16, B19), as well as on the A-side of the valley (e.g. A16, A17, A19, A20, A22) could be examples that have gone through this kind of evolution.

Also the catchments that were noticed to have on-going hillslope processes from the satellite pictures (Figure 35) cannot be completely ruled out from being partly fluvial. Although these ones can be defined as debris flow channels with most certainty compared to all the examined channels, it cannot be totally ruled out that they exhibited fluvial activity during the last glacial period, and only later started to show signs of debris flow activity. The geological maps referred to in the previous sections show

cemented alluvial fans and debris cones of Pleistocene age and these clearly indicate that there was a downstream transition to deposition in some of these catchments. However, a closer look at the satellite pictures indicate these fans have not been very active lately based on the vegetation cover and the present day channel drains around the edge of the fan directly into the Liri river. Without any well-constrained ages of the deposition of these fans it is hard to say when exactly they were abandoned.

As there are uncertainties in the dominant erosion process, using fluvial process rules in order to understand the response of channel long profiles at drainage areas less than ~10 km^2 should be carried out with caution, because so little is still known about debris flows and how this style of erosion affects the measured slopes (Whipple, 2004). Whipple (2004) warns that especially the transitional part from debris flows to fluvial channels might have different way of responding to uplift, climate and lithology. According to Whipple (2004) it could be expected that systematical changes exist in channel concavity with these variables in a way that has not yet been documented.

Despite the uncertainty of the original creation process of the channels in Figure 35, many of these have a drainage area higher than the typical A_{crit} 0.1–5 km^2 and in some cases there is clear debris flow erosion at present (see Figure 35), which supports the observations of debris flow erosion happening in larger drainages than A_{crit}. Another way of approachig this would be that the results of this study indicate A_{crit} simply being different for catchments that have gone through a major climate change: catchments that have been fluvial in the past, might become debris flow dominated after the climate change.

4.6 The Liri river incision

As the adjacent slopes are influenced by what is going on in the main river in the valley, involving the Liri river in the analysis was thought to be appropriate. The results of the long profile analysis along the Liri river show a knickpoint higher up from the area where this study was concentrating (see Figure 38). Back in time, the Fucino basin used to be a lake that may have been draining out through the Capistrello wind gap (see Figure 39). The lake has later been artificially drained, but the effects of the previous adding to drainage area could be one reason why the knickpoint is located in the vicinity of where the Liri river was joined by drainage out of the Fucino basin.

The other explanation is that this knickpoint represents the upstream limit of incision driven by base-level changes where the Liri river emerges at the coastline. The change in

base-level at the coast is the result of regional uplift of the Italian peninsula that has been ongoing for at least the last 1 Ma (Mancini et al., 2007; Serpelloni et al., 2013).

The long profile of the main Liri river downstream from that major knickpoint, i.e. at the length of the study area, shows no prominent knickpoints or change in slope. Nevertheless, the elevation changes in the DEM indicate that the river has started to incise, confirmed by erosion marks along the edge of the cemented Pleistocene fan and the pattern of elevation contours plotted in Figure 42. In order to examine whether the incision is visible in other parts of the valley, a set of similar profiles were taken towards both north and south from the studied fan, locations given in Figure 42 and cross-cuts shown in Figure 43.

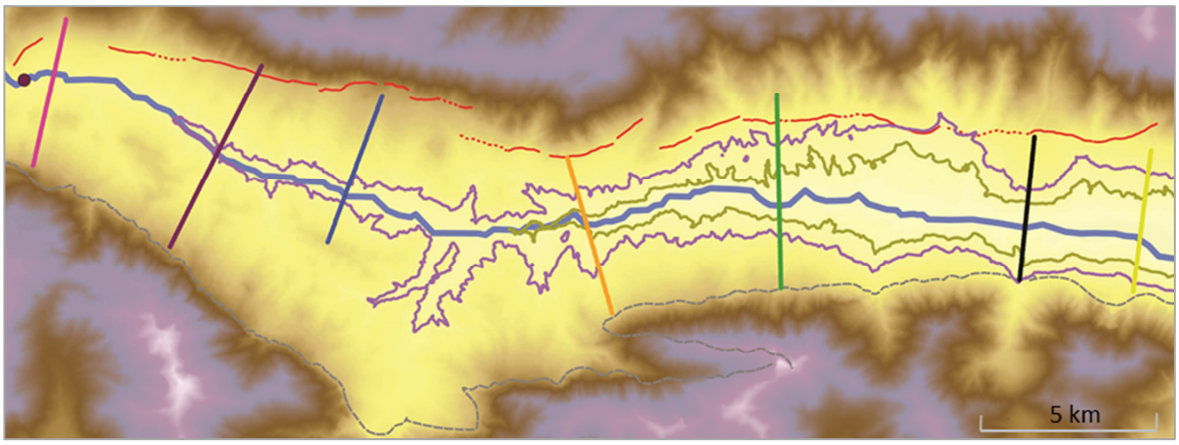

Figure 42. Location and length of the valley cross-cuts along the Liri river, also showing the contour lines for the estimated minimum and maximum incision. The purple dot represents the knickpoint on the long profile given in Figure 38.

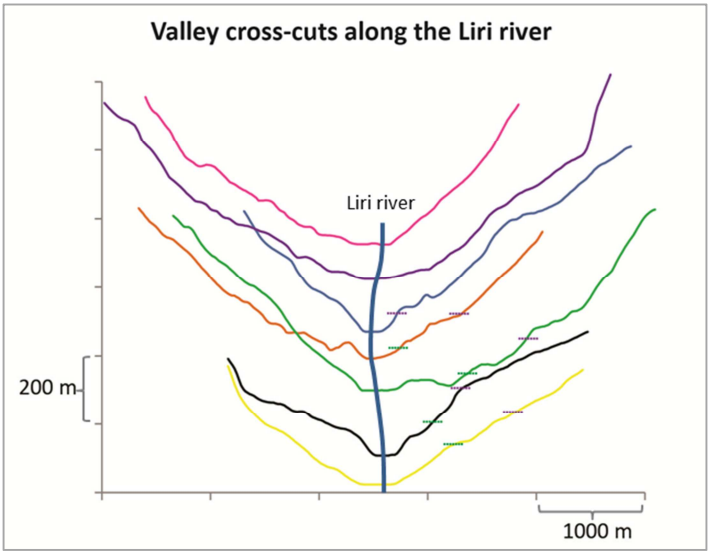

Figure 43. Illustrating the different profiles lined along the Liri river from north to south, colours indicating the location in the map above. The black one is the originally studied fan-profile. The green and purple dashed lines mark the elevation of the estimated minimum and maximum incision contours on the profiles.

Finding similar well-preserved fans was difficult, since they are not as prominant or have been altered by human activity (infrastructure, agriculture). The preservation of

any signs of the assumed Liri river incision is also dependent on whether the old river banks are preserved, e.g. have not been eroded away by streams coming from the hillsides or removed by other factors. The green profile in Figure 43 is an example where the uneveness due to humans and not only the Liri river activity is definitely recorded in the lowermost parts (below the green minimum incision contour). Nevertheless, it is interesting how these profiles also exhibit very irregular slopes below these old base-levels, the effect disappearing further north which lies above the extent of the estimated incision.

These results imply that the Liri river is going through a base-level fall that has probably generated a wave of incision migrating upstream, thus affecting the southern part of the valley more than the northern part. The rate of incision at the coast is approximately < 1 mm/ year (Mancini et al., 2007) driven by the uplift of the entire Italian peninsula, thus upstream along the Liri river the rate of incision may be less than this, decreasing to zero near the northern end of the study area.

4.7 Incision in the catchments and the transient effect

Based on the above analysis of incision in the Liri river itself, the current erosion rate in the catchments that are tributaries to the Liri river must be << 1 mm/ year. The main conclusion from this is that these catchments are at the moment incising very slowly. This is supporting the idea that the catchment morphologies may have been carved when the weathering and erosion rates were higher, most likely in a period of high precipitation and runoff during the Pleistocene.

Zolitschka and Negendank (1996) made sedimentological and microstratigraphical analysis of lake sediments in Lago Grande di Monticchio, southern Italy, and interpreted the paleoclimate based on dry density records, that are known to correlate with magnetic susceptibility as well as $\delta^{18}O$ records from Greenland ice cores, and negatively correlate with organic carbon content. The glacial record of the lake sediments was characterized by higher dry density values with two distinct peaks around ca. 30 ka and 60 ka, which Zolitschka and Negendank (1996) relate to lower temperature conditions during the glacial period. Although this is disagreeing with Allen et al. (2000) paper saying ~30 ka ago it was either warmer and less dry or cold and dry (depending what age of the pollens you look at, in their Table 2.), they do not really specify what is “warm” and what “dry” means in terms of changes in annual precipitation. Zolitschka and Negendank (1996) also marked the presence of dominating clastic varves and increased tree pollen coinciding with high dry density and magnetic susceptibility at

~30 ka ago, which they link to indicate a closed plant cover and high runoff. Zolitschka and Negendank (1996) suggest this to be a result of high precipitation favouring tree expansion as well as soil erosion and runoff processes. However, a less dense vegetation cover in the drainage basin would also make clastic material more available to erosional processes. Allen et al. (2000) made pollen analysis for sediment samples from the same lake, and their results indicate dry conditions with steppe dominated vegetation. Considering the results of Tucker et al. (2011) which indicated higher erosion rates during the last glaciation, the high clastic sediment records of Zolitschka and Negendank (1996), despite what the vegetation cover has been, would favour the interpretation of the studied catchments' morphology in the Liri valley being mostly carved during a time of higher erosion rates. If the interpretations of Zolitschka and Negendank (1996) are to be considered valid enough for a rough estimate of when these kind of high erosion conditions prevailed, then a minimum age of ~30 ka is inferred for the big cemented alluvial fans.

According to the geological maps of the area (Carta Geologica d'Italia, 1967, 152; Vezzani and Ghisetti, 1998) the southern part of the Liri fault side exhibits more old alluvial fans around the most prominent one (see Figure 44). Because the modern-day channel in this particular catchment 24 that used to feed into the most prominent fan has later changed its course, now running at the side of the fan, it can be estimated that the maximum incision in the channel since the fan was abandoned is around 100 to 200 m (Figure 45). This is assuming that the fan extended all the way to the Liri river, and the 3D shape of the fan was something similar to the cartoon in Figure 45. Averaging the 100–200 m of incision over the time span since 30 ka ago, it would give an upper estimate of the average annual erosion rate of approximately 3–6 mm/ year (100 or 200 m divided by 30 ka) since the abandoning of the fan. If the fan is older (e.g. 200 ka), then this rate is lower and more consistent with the rate of base-level fall in the Liri river (< 1 mm/ year) discussed above. An older age might reflect an additional period of high erosion rate not recorded by previous authors.

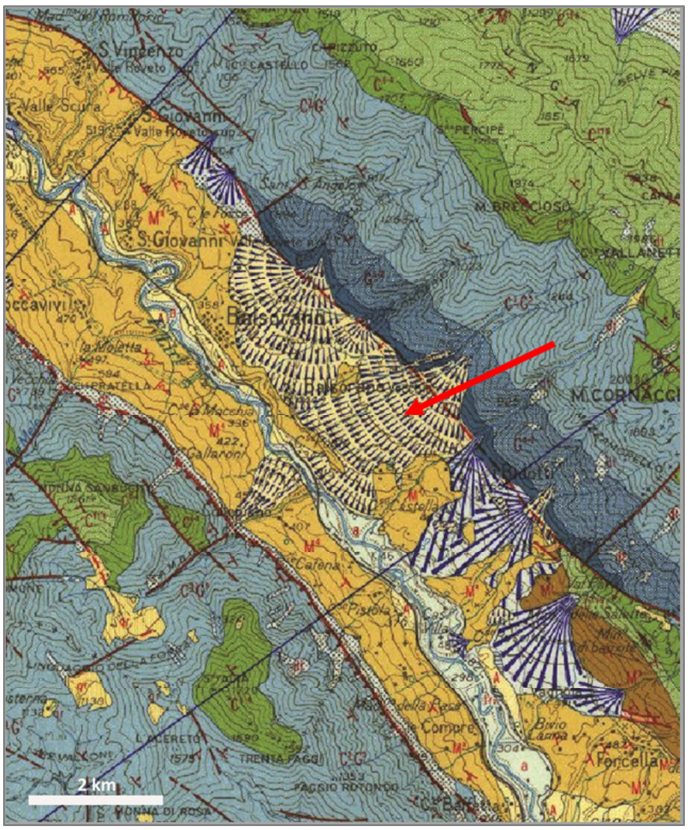

Figure 44. Close-up picture from Carta Geologica d'Italia (1967, 152) showing the fan used in the measurements, and the neighbouring fans. Notice also the modern Liri river flood plain.

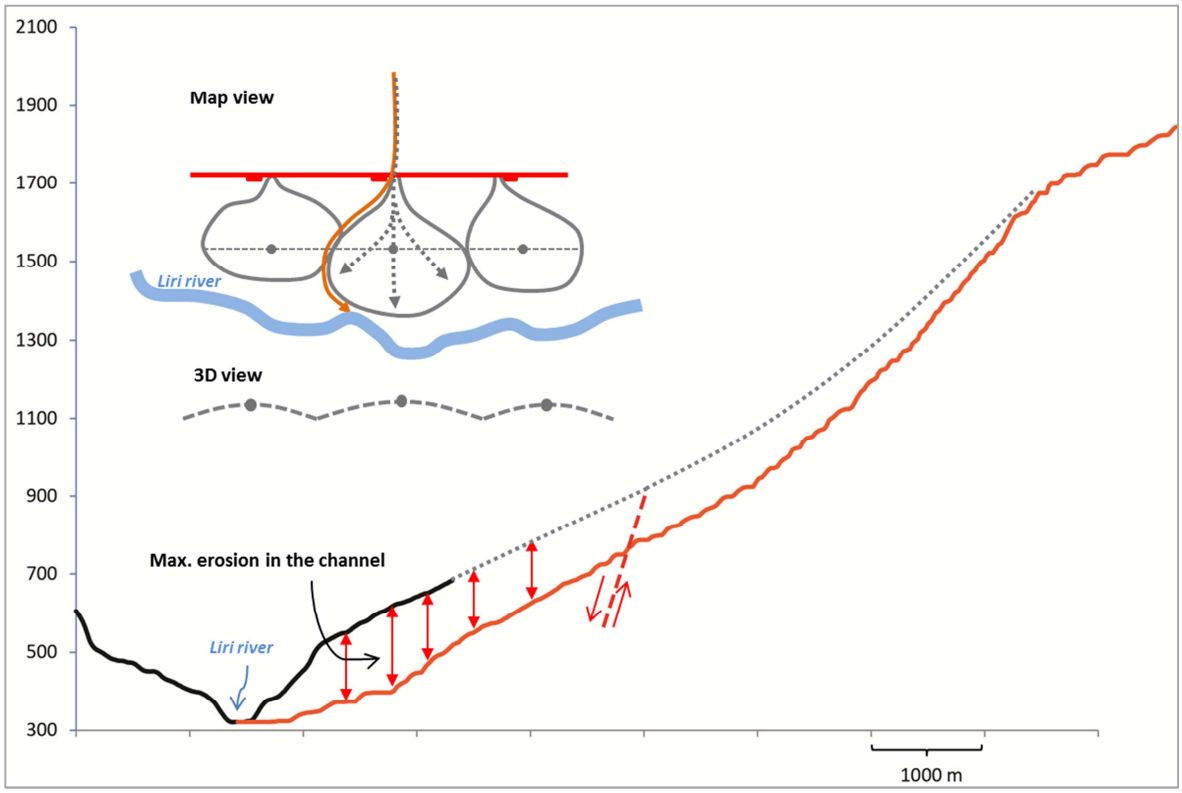

Figure 45. Examining erosion in the A-side catchment A24 by overlapping the big fan and the stream that fed into it before changing its course.

4.8 Is the Liri fault an active fault?

The high channel concavities of the southern Section 2 streams of the Liri fault side (A-side) give a reason to question the throw rates of 1.1 mm/ year measured by Roberts and Michetti (2004). The following observations have led to this conclusion:

1. The concavities in this part of the valley are either high (> 0.6) or extreme (> 1) at the crossing of the fault. These kind of values are normally related to declining rock uplift rate (e.g. Whipple, 2004). Moreover, Pleistocene fans that were developed downstream of the Liri fault are no longer active, i.e., there is no longer a downstream transition from incision to deposition.
2. The channels do not exhibit any sudden change in slope in the vicinity of the mapped fault trace. They are smoothly running across the fault, with clear channel forms even on the hangingwall side of the fault. The fact that the channels have not reacted to the supposed continuing faulting, and since the erosion is unlikely to be as efficient as in the past (during the Pleistocene), would speak for very little or no tectonic activity at this part of the Liri fault.
3. The larger drainage area of these catchments compared to Section 1 further north in the valley could suggest that the erosion in them is efficient enough for masking the slip rate as well as change in the substrate properties, but would depend on them incising at at least 1.1 mm/ year (to keep pace with the fault), and the field evidence for little active erosion in these channels suggests that this is highly unlikely.
4. The cemented Pleistocene alluvial fans and their top depositional surfaces show no evidence of faulting offsets.

These conclusions suggest that activity at least in the southern part of the Liri fault has ceased or been strongly reduced since the late Pleistocene. Taking into account the possibility of these channels experiencing a greater fluvial influence in the past, it is most likely that the morphology of these bigger channels has been defined when they were still acting mainly fluvial. This would also allow the explanation of the high concavities and the lack of knickpoints at the fault in these channels being a result of fluvial response to decrease in the fault slip rate. Figure 46 illustrates how the increase or decrease in slip rate has been observed to affect fluvial channels, as explained e.g. in Whipple and Tucker (1999), Whipple (2004), Kirby and Whipple (2012). An increase in slip rate would lead to a situation where the channels need to adjust to the new slope created by the accelerated faulting. The stream profile concavity would diminish and a

knickpoint would mark this adjusting process along the channel. If slip rate has decreased, the channel does not need to erode as fast to keep pace with the faulting. In this case the profile would become unaffected by the fault with time, and the shape would gradually also become more concave.

The scenario II in Figure 46 is one possible explanation to the high concavities in the Liri fault side Section 2 streams. It is consistent with the observations of high concavities in channels that are located where there has been a decrease in rock uplift rate (Whipple, 2004). Therefore, the high concavities of these channels also create the strongest counter argument to the > 1 mm/ year Holocene throw rate suggested by Roberts and Michetti (2004).

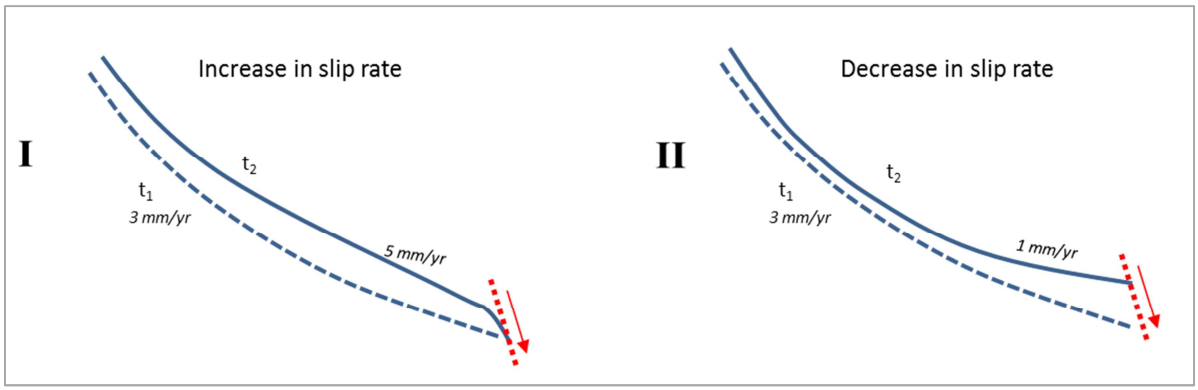

Figure 46. Two scenarios explaining different profile shapes. The dashed blue line represents a moderate concavity stream in a steady-state crossing a fault with a constant slip rate of 3 mm/ year. The upper blue lines are depicting what can be expected to happen to that stream if the slip rate increases or decreases in time.

The northern part of the Liri fault is known to have experienced earthquakes at least in the early 1900's, but these are poorly recorded in publications. This is nevertheless supporting Roberts and Michetti (2004) and Papanikolau et al.'s (2005) interpretation of the fault activity in the northern part. Whether this activity reaches the southern end is challenged by the findings of this study. Highlighting the fact that the Liri fault is segmented, it could be that the southern segment has become less active (i.e. << 1.1mm/ year) or even inactive. The changing characteristics of the studied catchments SE of catchment A10, as well as other factors listed above, together suggest that to the SE of the last well-constrained throw rate of Papanikolau et al. (2005), the rest of the Liri fault segments are most likely significantly less active during the Holocene than Roberts and Michetti (2004) suggested (Figure 47).

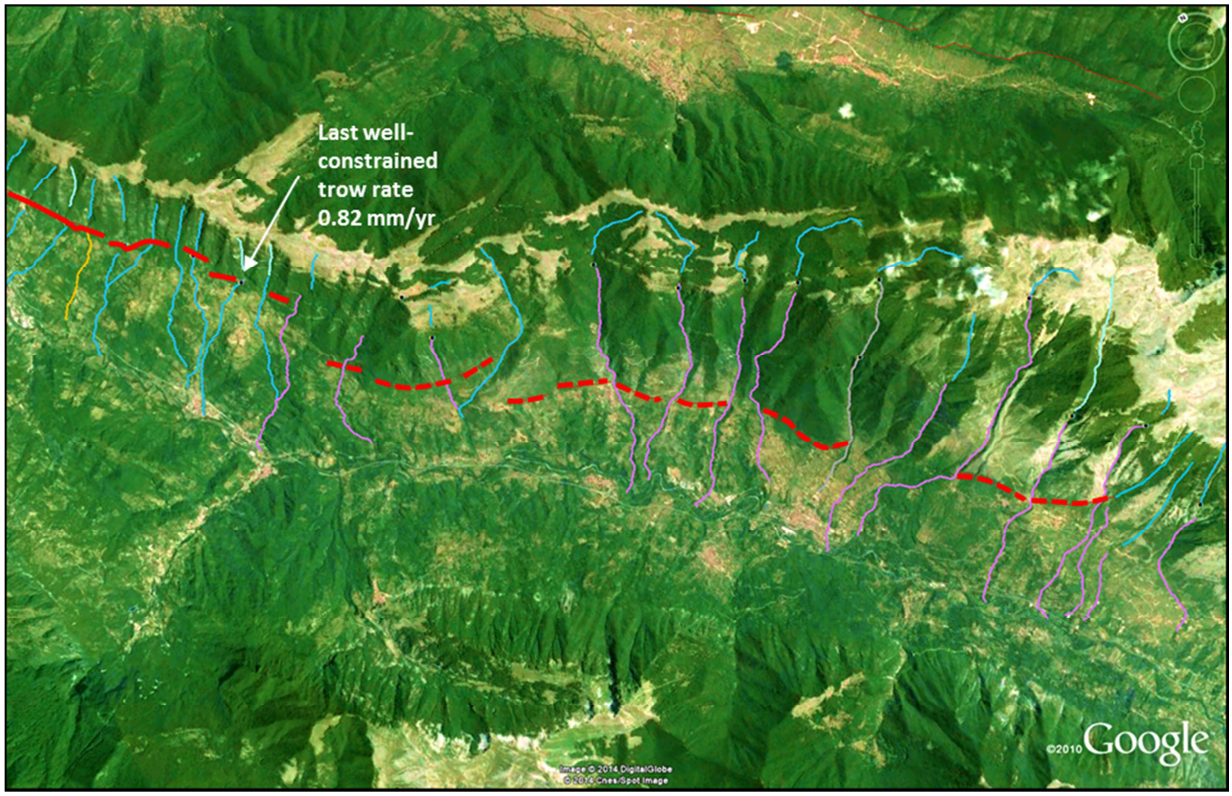

Figure 47. Google Earth photo showing the part of the Liri fault that is suggested to become either inactive or decreased in slip rate during the Holocene (dashed lines).

4.9 Comparing the two sides of the valley

The most intriguing question is why the catchments on the two sides of the valley behave so differently. The inactive B-side is dominated by a few major catchments with complicated long profiles that are thought to reflect mainly changes in the substrate properties and lithology. The channel concavities in these big catchments are in general low in the upper reaches and higher once entering the valley bottom. On the contrary, the bigger catchments on the A-side reach are characterized by higher concavity reaches that extend much further upstream into the limestone, above the valley bottom flysch.

In order to compare the two sides more closely, and consider the major differencies in these catchments that have gone through same climatic history and experienced the same base-level fall introduced by the Liri river, two samples from both sides from the southern end of Liri valley are taken into closer comparison. The main differencies between the these are depicted in Figure 48.

From this figure it is apparent how the long profiles differ remarkably, even though the drainage area is similar in all of them, so the discharge could be assumed to be very similar. The A-side profiles exhibit low or negative concavities in the upper reaches before the lithological contact betwen the Cretaceous and Jurassic limestones, and become highly concave further downstream. The B-side profiles are more linear with

low concavities in the upper reaches, but then have knickpoints where they enter the valley bottom flysch and become more concave. This is typical for rivers crossing major lithological contacts (Whipple, 2004). The reason to why the A-side profiles are not exhibiting similar reaction to the change in lithology, and are missing Holocene offset of the Liri fault, is suspected to be a result of the erosion both upstream and downstream from the fault caused by the Liri river incision, concealing any movement of the fault if it is happening at the same rate or slower than the erosion in these catchments. Schoenbohm et al. (2004) suggest that such high concavity values may be the transient response to a major, rapid base-level fall. However, the required amount of incision that this mechanism implies (over 1000 m for this area) is much greater than the 100 to 200 m observed along the Liri river. In addition, this kind of rapid base-level fall would be expected to affect both sides of the valley to the same degree, which is not what is observed in the Liri valley (see asymmetry in Figure 48).

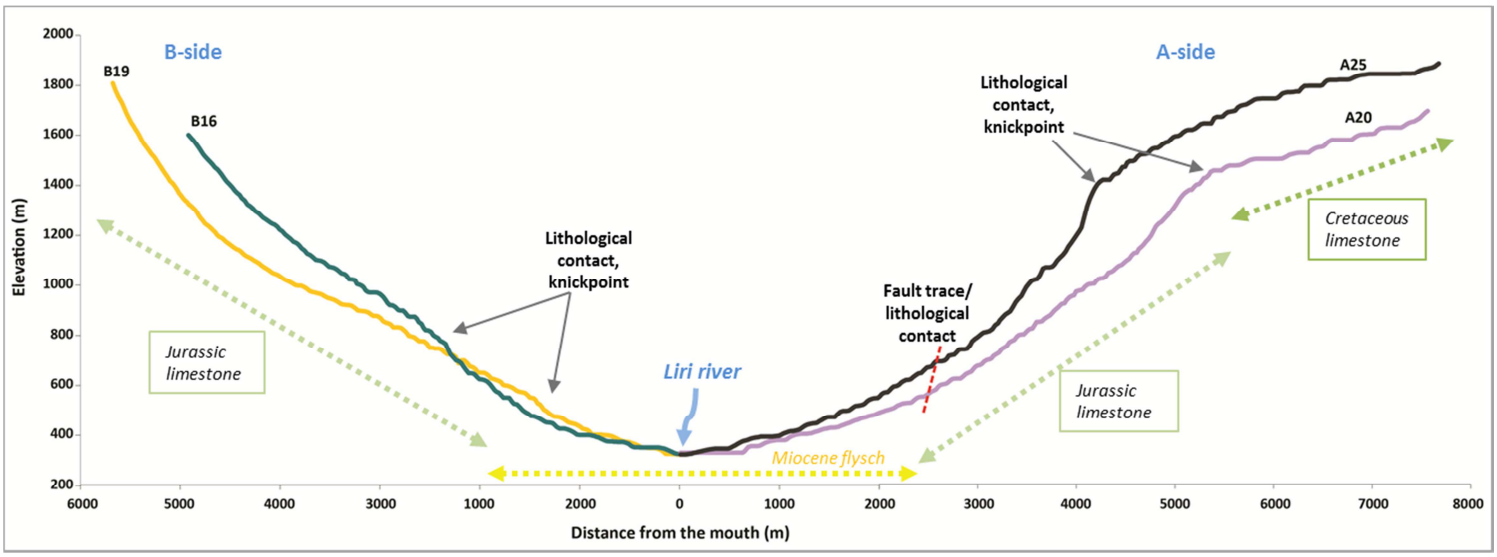

Figure 48. Comparing streams from the different sides of the valley (southern part, more or less opposite streams that can be expected to have gone through same climatic history and base-level fall), marking the lithological contacts as well as the Liri fault.

Therefore, it remains a question why the B-side streams appear to be more sensitive to lithology and less sensitive to the Liri river incision, assuming the previously discussed erosion in these catchments caused by base-level fall is valid, since the catchments on both sides could be expected to react similarly to the incision of the Liri river.

Conclusions

In this study the geomorphology of the Liri valley in the tectonically active central Apennines of Italy was examined using a 20-m DEM, comparing the two sides of the valley with similar lithologies but one side bounded by an active normal fault.

The slope-drainage area analysis, used here, is widely used in steady state fluvial landscape to estimate values for channel concavity and normalized steepness index. Here it was applied to a non-steady state case where the landscape is responding to active tectonics, climate change and changes in base-level driven by regional uplift of the Italian peninsula. It was found that these parameters are strongly dependent on how the regression limits are chosen, and the accuracy depends on how many data points are used to construct the power-law regression. After careful checking of the regression for each channel spatial variations of these parameters were interpreted to be reflecting spatially or temporally varying relative rock uplift rates, temporally varying climatic conditions, or spatially varying rock mass strength. The steepness index is more sensitive to complexities in the data, whereas the concavity is easier to compare with previous studies and was therefore mainly used for interpreting the geomorphic and tectonic history.

The results show that the long profiles clearly differ between the two sides of the valley. The inactive B-side streams are controlled mainly by lithology, showing low channel concavities (< 0.4) on the hillslopes and changing to a higher concavity where the streams reach the valley bottom sediments, and also exhibit knickpoints at the lithological boundaries. The active Liri fault side streams (A-side) seem to be more controlled by catchment size: the small catchments exhibit knickpoints at the fault/ lithological boundary between limestone and flysch and have in general lower concavities, whereas the larger catchments are nonchalant to this contact and exhibit high concavities ($>> 0.6$). These very high values may be explained if the southern part of the Liri fault is not active at present or that the slip rate is much lower than previous authors have suggested.

References

Allen, J. R., Brandt, U., Brauer, A., Hubberten, H. W., Huntley, B., Keller, J., J., Kraml, M., Mackensen, A., Mingram, J., Negendank, J., Nowaczyk, N., Oberhansli, H., Watts, W., Wulf, S., & Zolitschka, B., 1999. Rapid environmental changes in southern Europe during the last glacial period. *Nature*, *400*(6746), 740-743.

Allen, J. R., Watts, W. A., & Huntley, B., 2000. Weichselian palynostratigraphy, palaeovegetation and palaeoenvironment; the record from Lago Grande di Monticchio, southern Italy. *Quaternary International*, *73*, 91-110.

Burbank, D. W., Leland, J., Fielding, E., Anderson, R. S., Brozovic, N., Reid, M. R., & Duncan, C., 1996. Bedrock incision, rock uplift and threshold hillslopes in the northwestern Himalayas. Nature, 379(6565), 505-510.

Carrara, C., Frezzotti, M., & Giraudi, C., 1995. Stratigrafia plio-quaternaria. In: *Lazio Meridionale, Sintesi delle ricerche geologiche multidisciplinari. ENEA*, 62-85.

Carta Geologica d'Italia, 1967. 1:100000, 151, Alatri. Servizio Geologico d'Italia.

Carta Geologica d'Italia, 1967. 1:100000, 152, Sora. Servizio Geologico d'Italia.

Cavinato, G. P., & De Celles, P. G., 1999. Extensional basins in the tectonically bimodal central Apennines fold-thrust belt, Italy: response to corner flow above a subducting slab in retrograde motion. *Geology*, *27*(10), 955-958.

Cavinato, G. P., Carusi, C., Dall'Asta, M., Miccadei, E., & Piacentini, T., 2002. Sedimentary and tectonic evolution of Plio–Pleistocene alluvial and lacustrine deposits of Fucino Basin (central Italy). *Sedimentary Geology*, *148*(1), 29-59.

Centamore, E., & Nisio, S., 2003. Effects of uplift and tilting in the Central-Northern Apennines (Italy). *Quaternary international*, *101*, 93-101.

D'Agostino, N., & McKenzie, D., 1999. Convective support of long-wavelength topography in the Apennines (Italy). *Terra Nova, 11, 234-238*.

D'Agostino, N., Jackson, J. A., Dramis, F., & Funiciello, R., 2001a. Interactions between mantle upwelling, drainage evolution and active normal faulting: an example from the central Apennines (Italy). *Geophysical Journal International*, *147*(2), 475-497.

D'Agostino, N., Giuliani, R., Mattone, M., Bonci, L., 2001b. Active crustal extension in the central Apennines (Italy) inferred from GPS measurements in the interval 1994-1999. *Geophysical Research Letters 28*, 2121-2124.

Davy, P., & Crave, A., 2000. Upscaling local-scale transport processes in large-scale relief dynamics. *Physics and Chemistry of the Earth, Part A: Solid Earth and Geodesy, 25*(6), 533-541.

Densmore, A. L., Gupta, S., Allen, P. A., & Dawers, N. H., 2007. Transient landscapes at fault tips. *Journal of Geophysical Research: Earth Surface (2003–2012)*, *112*(F3).

Doglioni, C., 1995. Geological remarks on the relationships between extension and convergent geodynamic settings. *Tectonophysics* 252.1: 253-267.

Doglioni, C., Mongelli, F., & Pialli, G., 1998. Boudinage of the Alpine belt in the Apenninic back-arc. *Mem. Soc. Geol. It*, *52*, 457-468.

Duvall, A., Kirby, E., & Burbank, D., 2004. Tectonic and lithologic controls on bedrock channel profiles and processes in coastal California. Journal of Geophysical Research: Earth Surface (2003–2012), 109(F3).

Flint, J. J., 1974. Stream gradient as a function of order, magnitude, and discharge. *Water Resources Research*, *10*(5), 969-973.

Frepoli, A., & Amato, A., 1997. Contemporaneous extension and compression in the northern Apennines from earthquake fault-plane solutions. *Geophysical Journal International*, *129*(2), 368-388.

Galadini, F., 1999. Pleistocene changes in the central Apennine fault kinematics: a key to decipher active tectonics in central Italy. *Tectonics*, *18*(5), 877-894.

Galadini, F., & Galli, P., 2000. Active tectonics in the Central Apennines (Italy) — input data for seismic hazard Assessment. *Natural Hazards 22*, 225–270.

Giraudi, C., & Frezzotti, M., 1997. Late Pleistocene glacial events in the central Apennines, Italy. *Quaternary Research*, *48*(3), 280-290.

Gliozzi, E., & Mazzini, I., 1998. Palaeoenvironmental analysis of Early Pleistocene brackish marshes in the Rieti and Tiberino intrapenninic basins (Latium and Umbria, Italy) using ostracods (Crustacea). *Palaeogeography, Palaeoclimatology, Palaeoecology*, *140*(1), 325-333.

Gueguen, E., Doglioni, C., & Fernandez, M., 1998. On the post-25 Ma geodynamic evolution of the western Mediterranean. *Tectonophysics*, *298*(1), 259-269.

Hack, J.T., 1957. Studies of Longitudinal Stream Profiles in Virginia and Maryland. *U.S. Geological Survey Professional Paper 294-B*, 45-97.

Hobley, D. E., Sinclair, H. D., & Cowie, P. A., 2010. Processes, rates, and time scales of fluvial response in an ancient postglacial landscape of the northwest Indian Himalaya. *Geological Society of America Bulletin*, *122*(9-10), 1569-1584.

Howard, A. D., 1994. A detachment-limited model of drainage basin evolution. *Water resources research*, *30*(7), 2261-2285.

Howard, A. D., 1998. Long profile development of bedrock channels: Interaction of weathering, mass wasting, bed erosion, and sediment transport. *Geophysical Monograph Series, 107*, 297-319.

Kirby, E., & Whipple, K., 2001. Quantifying differential rock-uplift rates via stream profile analysis. *Geology*, *29*(5), 415-418.

Kirby, E., & Whipple, K. X., 2012. Expression of active tectonics in erosional landscapes. *Journal of Structural Geology*, *44*, 54-75.

Kirby, E., Whipple, K. X., Tang, W., & Chen, Z., 2003. Distribution of active rock uplift along the eastern margin of the Tibetan Plateau: Inferences from bedrock channel longitudinal profiles. *Journal of Geophysical Research*, *108*(B4), 2217.

Lague, D., & Davy, P., 2003. Constraints on the long-term colluvial erosion law by analyzing slope-area relationships at various tectonic uplift rates in the Siwaliks Hills (Nepal). *Journal of Geophysical Research: Solid Earth (1978–2012)*, 108(B2).

Lancaster, S. T., 2008. Evolution of sediment accommodation space in steady state bedrock-incising valleys subject to episodic aggradation. *Journal of Geophysical Research: Earth Surface (2003–2012)*, *113*(F4).

Lavecchia, G., Brozzetti, F., Barchi, M., Menichetti, M., & Keller, J. V., 1994. Seismotectonic zoning in east-central Italy deduced from an analysis of the Neogene to present deformations and related stress fields. *Geological Society of America Bulletin*, *106*(9), 1107-1120.

Malinverno, A., & Ryan, W. B., 1986. Extension in the Tyrrhenian Sea and shortening in the Apennines as result of arc migration driven by sinking of the lithosphere. *Tectonics*, *5*(2), 227-245.

Mancini, M., D'Anastasio, E., Barbieri, M., & De Martini, P. M., 2007. Geomorphological, paleontological and $^{87}Sr/^{86}Sr$ isotope analyses of early Pleistocene paleoshorelines to define the uplift of Central Apennines (Italy). *Quaternary Research*, *67*(3), 487-501.

Montgomery, D. R., & Buffington, J. M., 1997. Channel-reach morphology in mountain drainage basins. *Geological Society of America Bulletin*, 109(5), 596-611.

Montgomery, D. R., & Foufoula-Georgiou, E., 1993. Channel network source representation using digital elevation models. *Water Resources Research*, *29*(12), 3925-3934.

Papanikolaou, I. D., Roberts, G. P., & Michetti, A. M., 2005. Fault scarps and deformation rates in Lazio–Abruzzo, Central Italy: Comparison between geological fault slip-rate and GPS data. *Tectonophysics*, *408*(1), 147-176.

Patacca, E., Sartori, R., & Scandone, P., 1990. Tyrrhenian basin and Apenninic arcs: kinematic relations since late Tortonian times. *Mem. Soc. Geol. It*, *45*(1), 425-451.

Piccardi, L., Gaudemer, Y., Tapponnier, P., & Boccaletti, M., 1999. Active oblique extension in the central Apennines (Italy): evidence from the Fucino region. *Geophysical Journal International*, 139: 499-530.

Roberts, G. P., & Michetti, A. M., 2004. Spatial and temporal variations in growth rates along active normal fault systems: an example from The Lazio–Abruzzo Apennines, central Italy. *Journal of Structural Geology*, *26*(2), 339-376.

Schoenbohm, L. M., Whipple, K. X., Burchfiel, B. C., & Chen, L., 2004. Geomorphic constraints on surface uplift, exhumation, and plateau growth in the Red River region, Yunnan Province, China. *Geological Society of America Bulletin*, 116(7-8), 895-909.

Serafini, S., & Vittori, E., 1995. Analisi di mesostrutture tettoniche di tipo fragile nella Val Roveto, nella Pina di Sora e in Val di Comino. In: *Lazio Meridionale, Sintesi delle Ricerche Geologiche Multidisciplinari. ENEA Dipartimento Ambiente, Roma*, 93-107.

Serpelloni, E., Faccenna, C., Spada, G., Dong, D., & Williams, S. D., 2013. Vertical GPS ground motion rates in the Euro-Mediterranean region: New evidence of velocity gradients at different spatial scales along the Nubia-Eurasia plate boundary. *Journal of Geophysical Research: Solid Earth*, *118*(11), 6003-6024.

Sklar, L., & Dietrich, W. E., 1998. River longitudinal profiles and bedrock incision models: Stream power and the influence of sediment supply. *Rivers over rock: fluvial processes in bedrock channels*, 237-260.

Snyder, N. P., Whipple, K. X., Tucker, G. E., & Merritts, D. J., 2000. Landscape response to tectonic forcing: Digital elevation model analysis of stream profiles in the Mendocino triple junction region, northern California. *Geological Society of America Bulletin*, *112*(8), 1250-1263.

Stock, J., & Dietrich, W. E., 2003. Valley incision by debris flows: Evidence of a topographic signature. *Water Resources Research*, *39*(4).

Stock, J. D., & Dietrich, W. E., 2006. Erosion of steepland valleys by debris flows. Geological Society of America Bulletin, 118(9-10), 1125-1148.

Stock, J. D., Montgomery, D. R., Collins, B. D., Dietrich, W. E., & Sklar, L., 2005. Field measurements of incision rates following bedrock exposure: Implications for process controls on the long profiles of valleys cut by rivers and debris flows. *Geological Society of America Bulletin, 117*(1-2), 174-194.

Strahler, A. N., 1957. Quantitative analysis of watershed geomorphology. *Civ. Eng*, *101*, 1258-1262.

Tucker, G. E., McCoy, S. W., Whittaker, A. C., Roberts, G. P., Lancaster, S. T., & Phillips, R., 2011. Geomorphic significance of postglacial bedrock scarps on normal-fault footwalls. *Journal of Geophysical Research: Earth Surface (2003–2012)*, *116*(F1).

Vezzani, L., Ghisetti, F., 1998. Carta Geologica Dell'Abruzzo, SELCA, Via R. Giuliani, 153, Firenze, 1:100,000.

Whipple, K. X., & Tucker, G. E., 1999. Dynamics of the stream-power river incision model: Implications for height limits of mountain ranges, landscape response timescales, and research needs. *Journal of Geophysical Research*, *104*(B8), 17661-17.

Whipple, K. X., & Tucker, G. E., 2002. Implications of sediment-flux-dependent river incision models for landscape evolution. Journal of Geophysical Research: Solid Earth (1978–2012), 107(B2), ETG-3.

Whipple, K. X., 2004. Bedrock rivers and the geomorphology of active orogens. *Annual Review of Earth and Planetary Sciences*, *32*, 151-185.

Whittaker, A. C., Cowie, P. A., Attal, M., Tucker, G. E., & Roberts, G. P., 2007a. Bedrock channel adjustment to tectonic forcing: Implications for predicting river incision rates. *Geology*, *35*(2), 103-106.

Whittaker, A. C., Cowie, P. A., Attal, M., Tucker, G. E., & Roberts, G. P., 2007b. Contrasting transient and steady-state rivers crossing active normal faults: New field observations from the Central Apennines, Italy. *Basin Research*, *19*(4), 529-556.

Whittaker, A. C., Attal, M., Cowie, P. A., Tucker, G. E., & Roberts, G., 2008. Decoding temporal and spatial patterns of fault uplift using transient river long profiles. *Geomorphology*, *100*(3), 506-526.

Whittaker, A. C., 2012. How do landscapes record tectonics and climate? *Lithosphere*, *4*(2), 160-164.

Wobus, C., Whipple, K. X., Kirby, E., Snyder, N., Johnson, J., Spyropolou, K., Crosby, B., & Sheehan, D., 2006. Tectonics from topography: Procedures, promise, and pitfalls. In: Willett, S.D., Hovitus, N., Brandon, M.T., Fischer, D.M. (Eds.) *Geological Society of America Special Paper*, *398*, 55-74.

Zolitschka, B., & Negendank, J. F., 1996. Sedimentology, dating and palaeoclimatic interpretation of a 76.3 ka record from Lago Grande di Monticchio, southern Italy. *Quaternary Science Reviews*, *15*(2), 101-112.

Appendix A. Longitudinal profiles of analyzed streams

A-side:

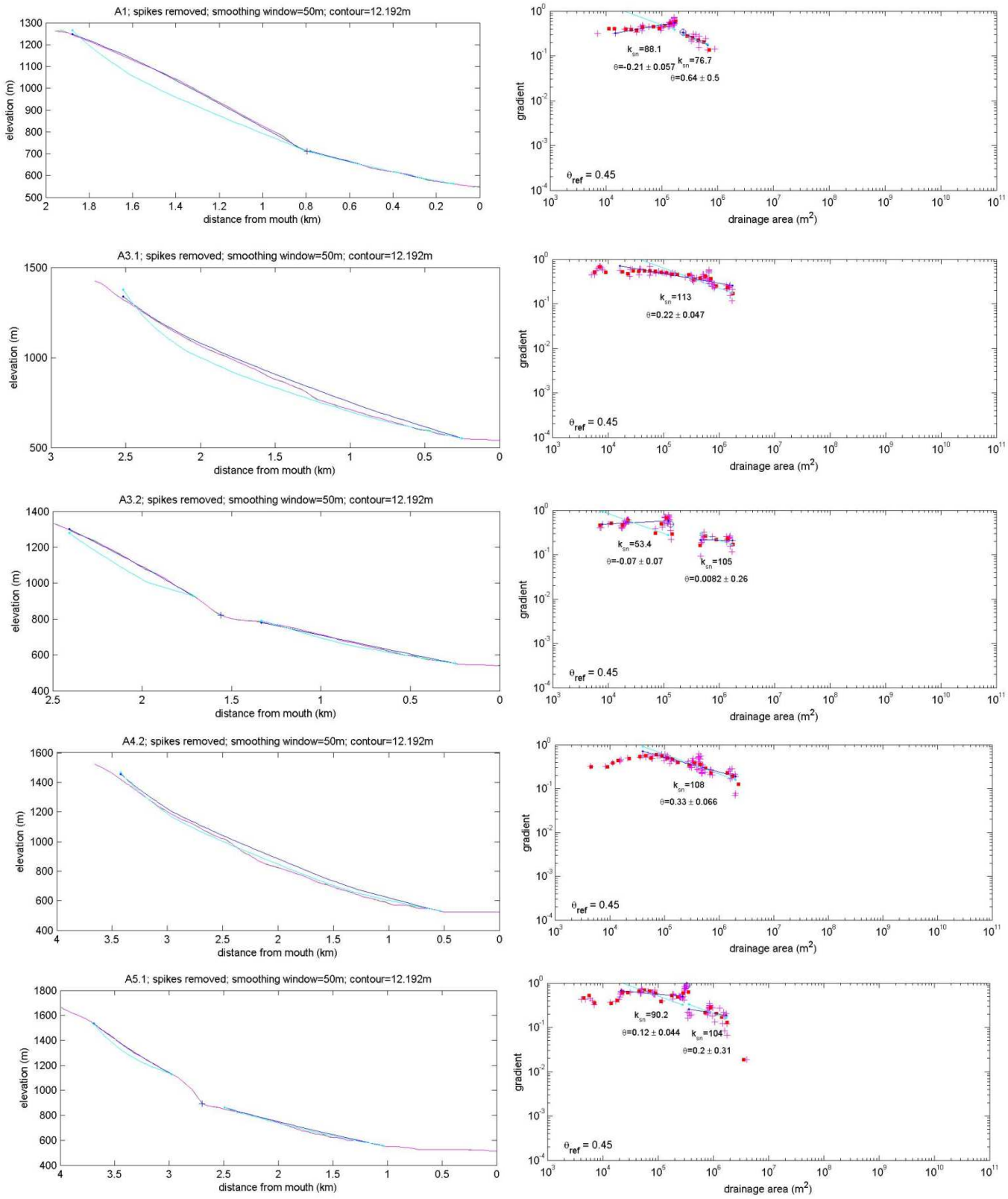

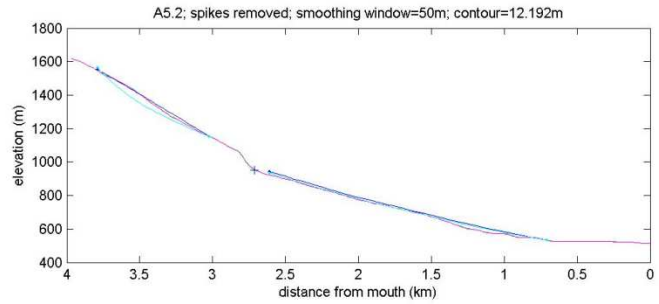
A5.2; spikes removed; smoothing window=50m; contour=12.192m
elevation (m)
distance from mouth (km)

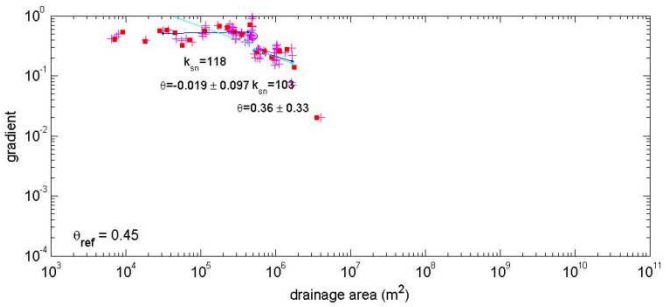
k_sn=118
θ=-0.019 ± 0.097
k_sn=103
θ=0.36 ± 0.33
θ_ref = 0.45
gradient
drainage area (m²)

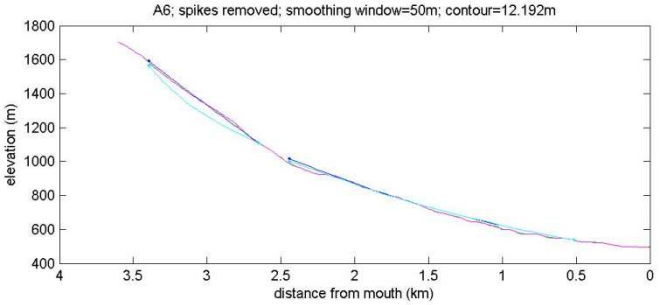
A6; spikes removed; smoothing window=50m; contour=12.192m
elevation (m)
distance from mouth (km)

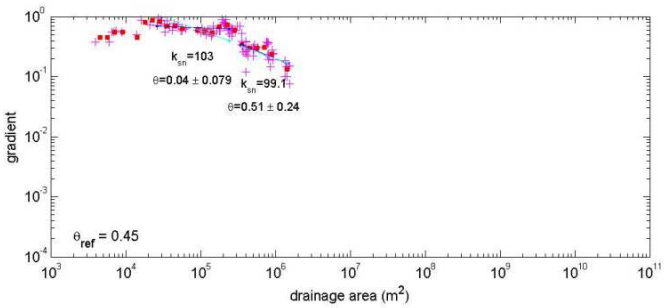
k_sn=103
θ=0.04 ± 0.079
k_sn=99.1
θ=0.51 ± 0.24
θ_ref = 0.45
gradient
drainage area (m²)

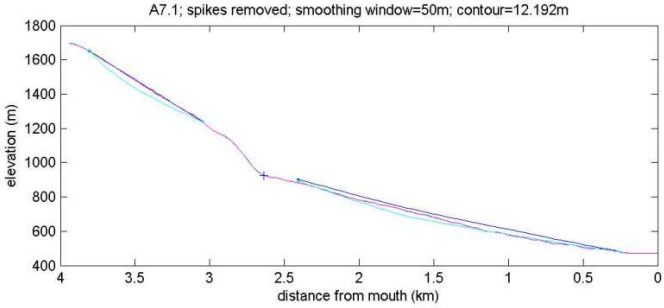
A7.1; spikes removed; smoothing window=50m; contour=12.192m
elevation (m)
distance from mouth (km)

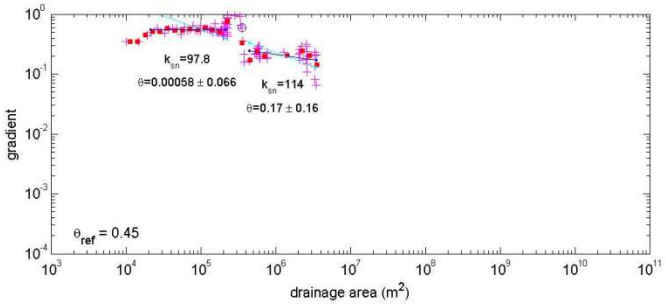
k_sn=97.8
θ=0.00058 ± 0.066
k_sn=114
θ=0.17 ± 0.16
θ_ref = 0.45
gradient
drainage area (m²)

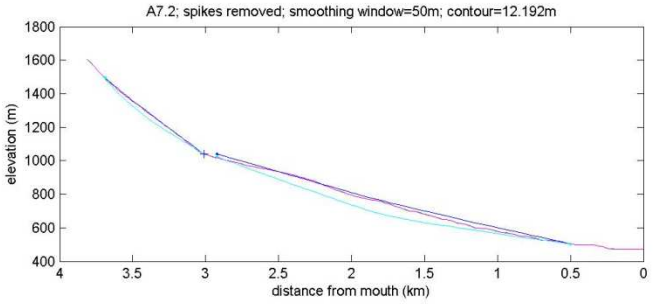
A7.2; spikes removed; smoothing window=50m; contour=12.192m
elevation (m)
distance from mouth (km)

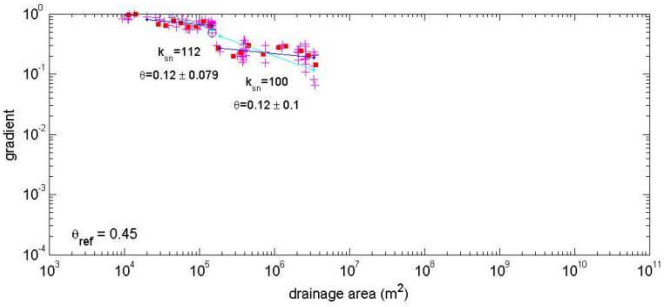
k_sn=112
θ=0.12 ± 0.079
k_sn=100
θ=0.12 ± 0.1
θ_ref = 0.45
gradient
drainage area (m²)

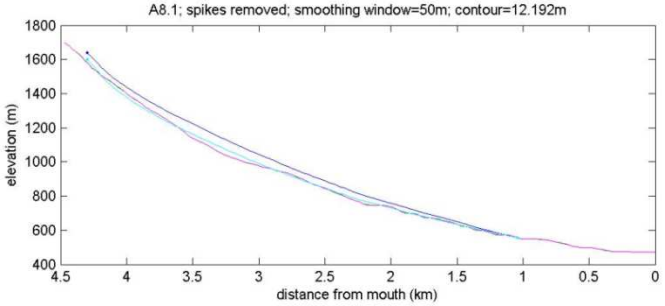
A8.1; spikes removed; smoothing window=50m; contour=12.192m
elevation (m)
distance from mouth (km)

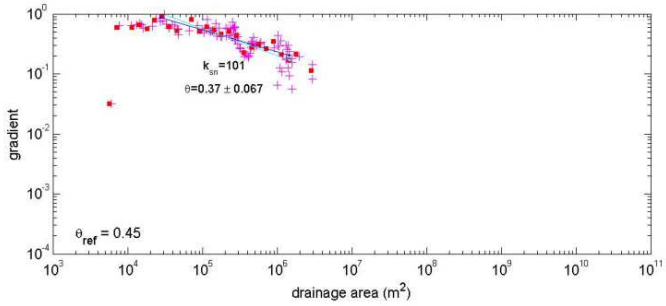
k_sn=101
θ=0.37 ± 0.067
θ_ref = 0.45
gradient
drainage area (m²)

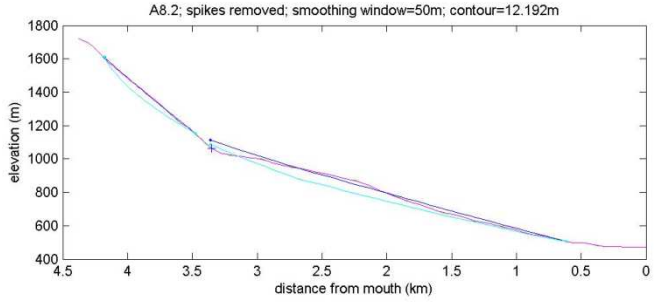
A8.2; spikes removed; smoothing window=50m; contour=12.192m
elevation (m)
distance from mouth (km)

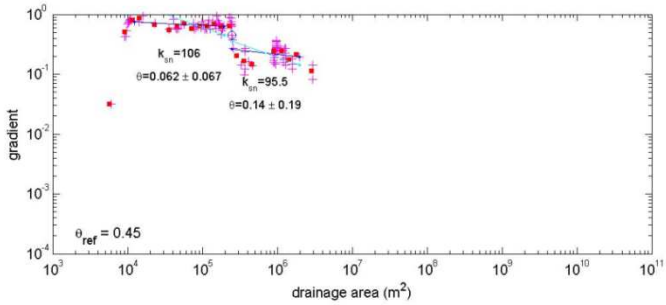
k_sn=106
θ=0.062 ± 0.067
k_sn=95.5
θ=0.14 ± 0.19
θ_ref = 0.45
gradient
drainage area (m²)

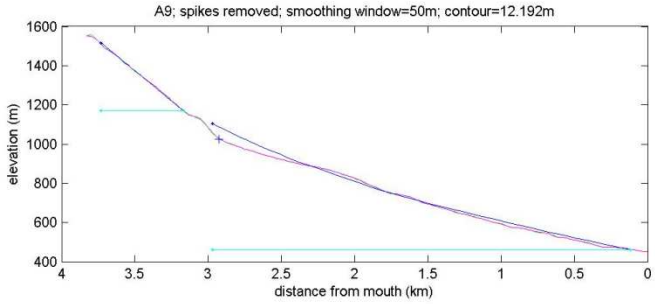
A9; spikes removed; smoothing window=50m; contour=12.192m
elevation (m)
distance from mouth (km)

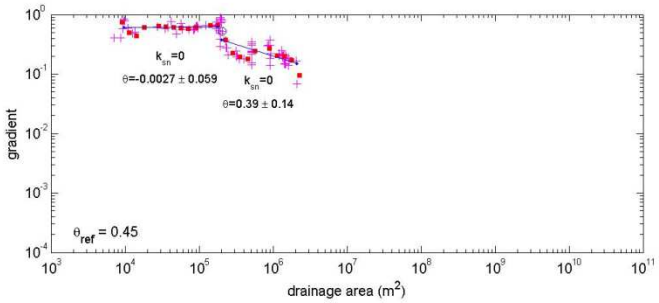
k_sn=0
θ=-0.0027 ± 0.059
k_sn=0
θ=0.39 ± 0.14
θ_ref = 0.45
gradient
drainage area (m²)

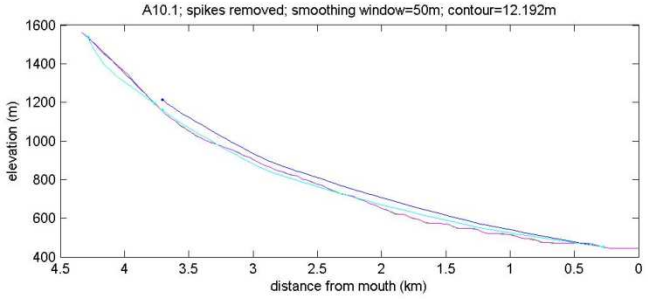
A10.1; spikes removed; smoothing window=50m; contour=12.192m
elevation (m)
distance from mouth (km)

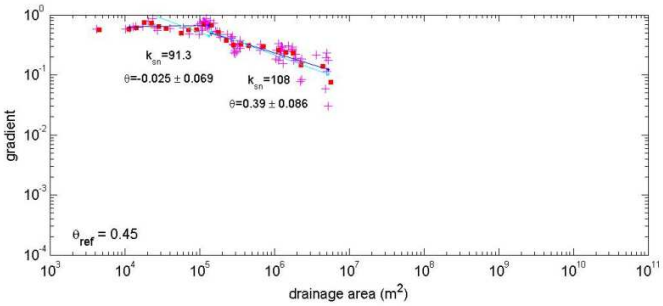
k_sn=91.3
θ=-0.025 ± 0.069
k_sn=108
θ=0.39 ± 0.086
θ_ref = 0.45
gradient
drainage area (m²)

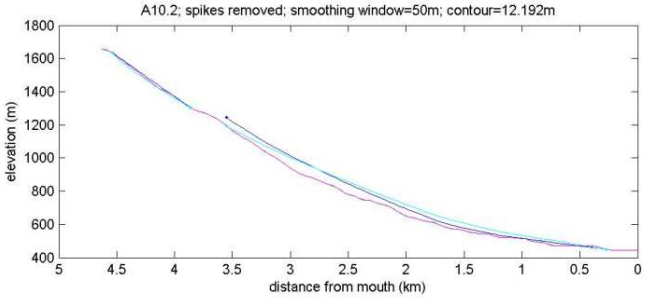
A10.2; spikes removed; smoothing window=50m; contour=12.192m
elevation (m)
distance from mouth (km)

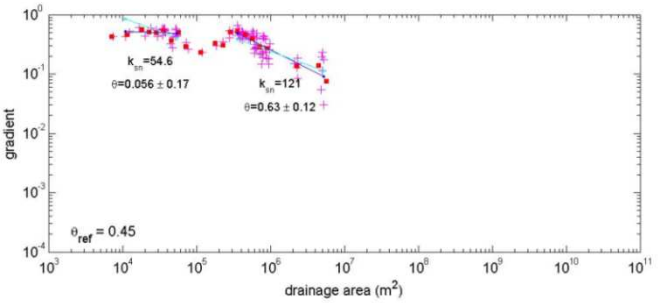
k_sn=54.6
θ=0.056 ± 0.17
k_sn=121
θ=0.63 ± 0.12
θ_ref = 0.45
gradient
drainage area (m²)

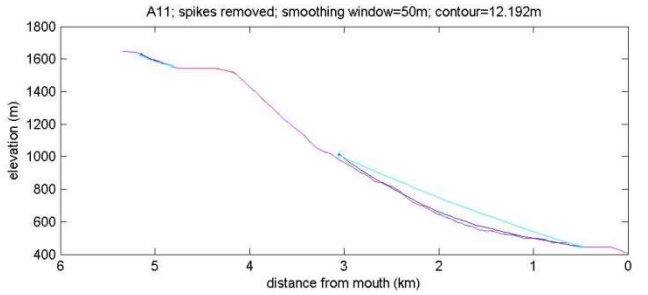
A11; spikes removed; smoothing window=50m; contour=12.192m
elevation (m)
distance from mouth (km)

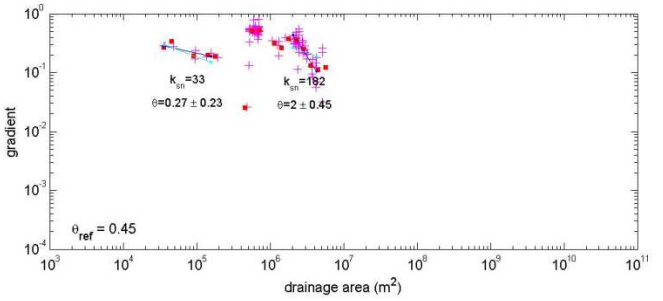
k_sn=33
θ=0.27 ± 0.23
k_sn=182
θ=2 ± 0.45
θ_ref = 0.45
gradient
drainage area (m²)

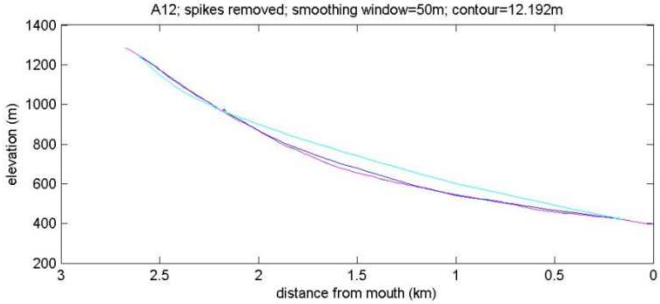
A12; spikes removed; smoothing window=50m; contour=12.192m
elevation (m)
distance from mouth (km)

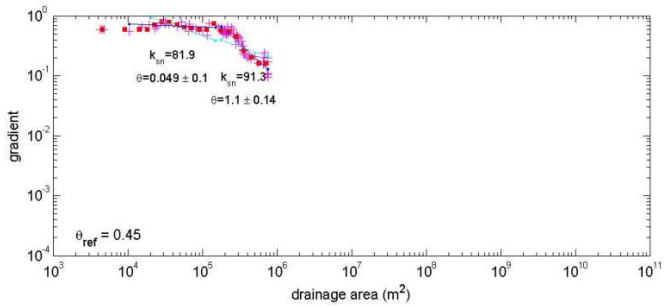
k_sn=81.9
θ=0.049 ± 0.1
k_sn=91.3
θ=1.1 ± 0.14
θ_ref = 0.45
gradient
drainage area (m²)

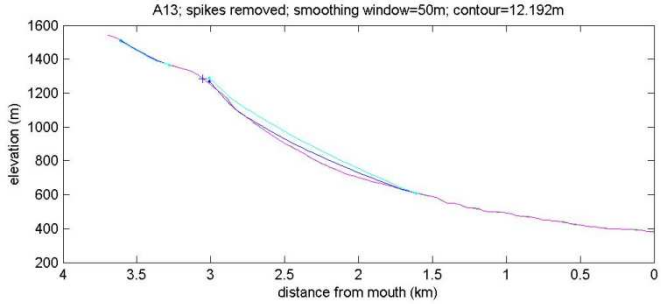
A13; spikes removed; smoothing window=50m; contour=12.192m
elevation (m)
distance from mouth (km)

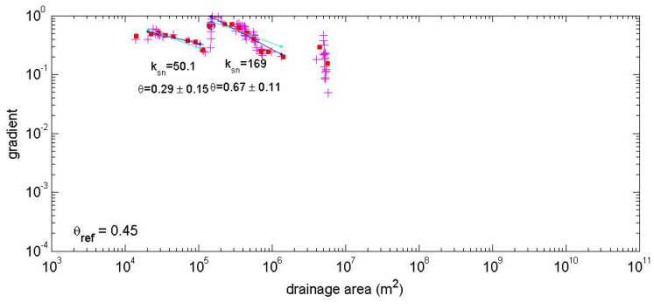
k_sn=50.1
θ=0.29 ± 0.15
k_sn=169
θ=0.67 ± 0.11
θ_ref = 0.45
gradient
drainage area (m²)

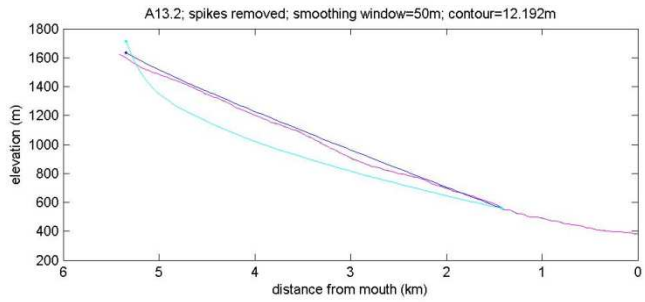
A13.2; spikes removed; smoothing window=50m; contour=12.192m
elevation (m)
distance from mouth (km)

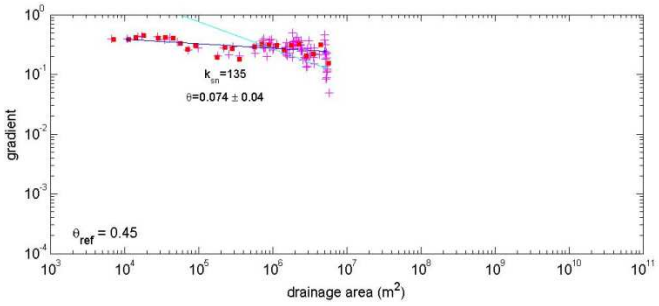
k_sn=135
θ=0.074 ± 0.04
θ_ref = 0.45
gradient
drainage area (m^2)

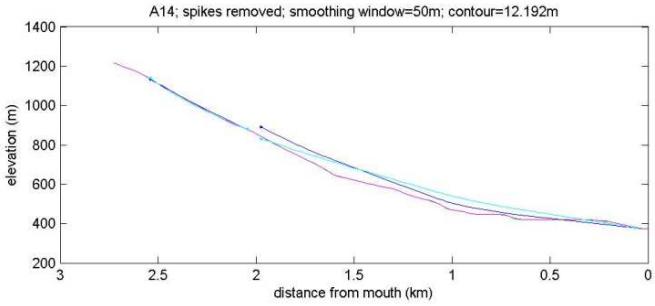
A14; spikes removed; smoothing window=50m; contour=12.192m
elevation (m)
distance from mouth (km)

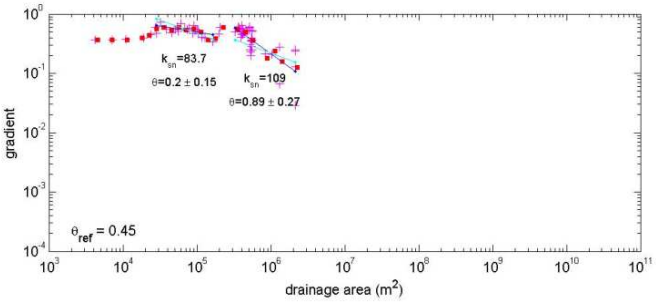
k_sn=83.7
θ=0.2 ± 0.15
k_sn=109
θ=0.89 ± 0.27
θ_ref = 0.45
gradient
drainage area (m^2)

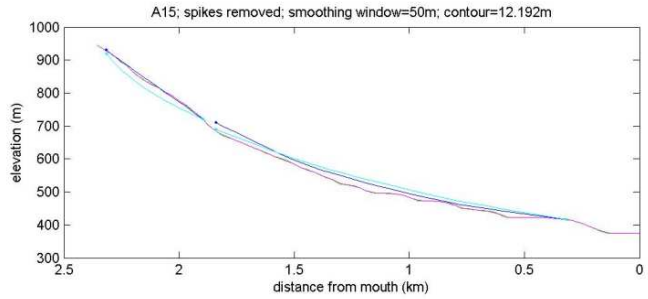
A15; spikes removed; smoothing window=50m; contour=12.192m
elevation (m)
distance from mouth (km)

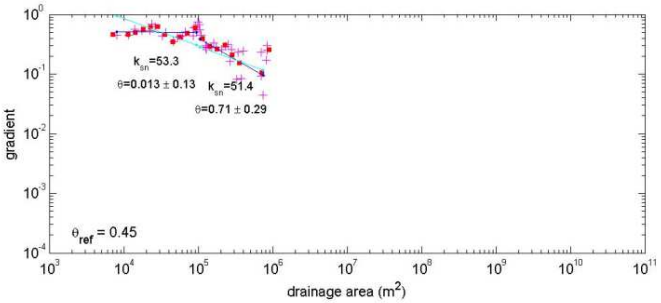
k_sn=53.3
θ=0.013 ± 0.13
k_sn=51.4
θ=0.71 ± 0.29
θ_ref = 0.45
gradient
drainage area (m^2)

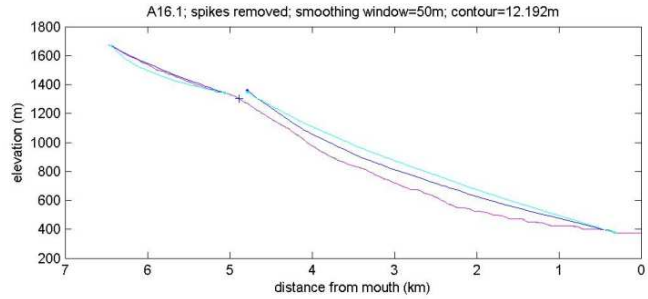
A16.1; spikes removed; smoothing window=50m; contour=12.192m
elevation (m)
distance from mouth (km)

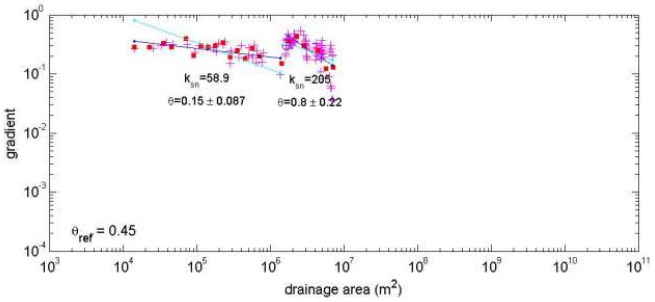
k_sn=58.9
θ=0.15 ± 0.087
k_sn=205
θ=0.8 ± 0.22
θ_ref = 0.45
gradient
drainage area (m^2)

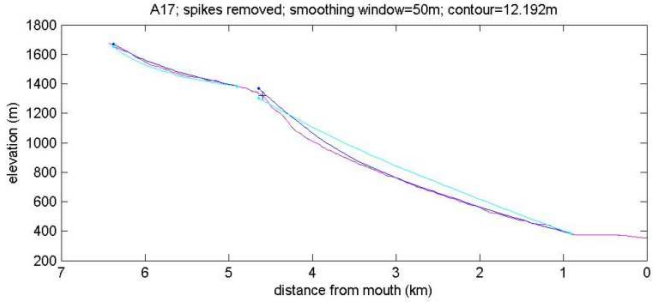
A17; spikes removed; smoothing window=50m; contour=12.192m
elevation (m)
distance from mouth (km)

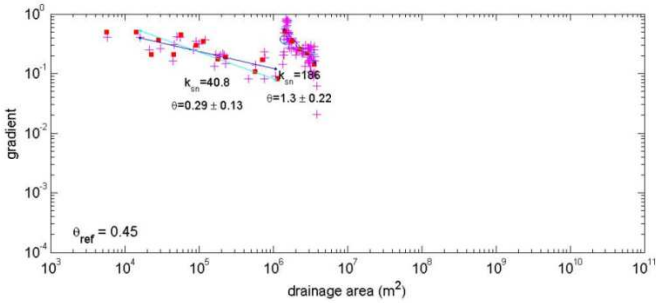
k_sn=40.8
θ=0.29 ± 0.13
k_sn=186
θ=1.3 ± 0.22
θ_ref = 0.45
gradient
drainage area (m^2)

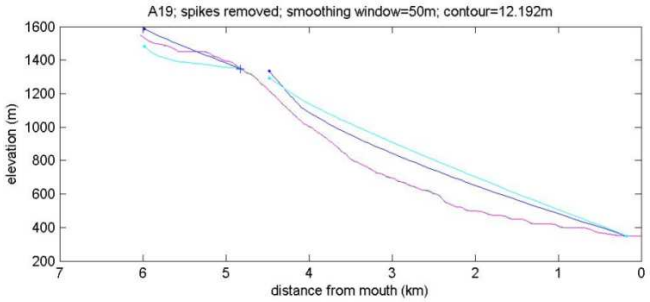
A19; spikes removed; smoothing window=50m; contour=12.192m
elevation (m)
distance from mouth (km)

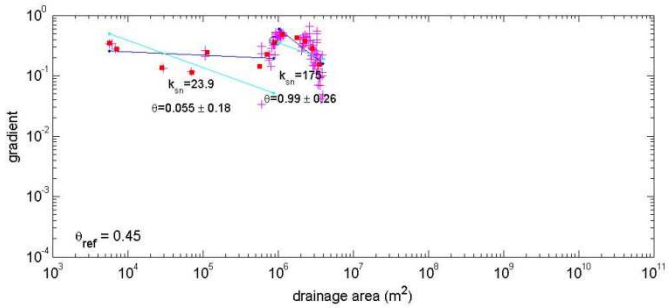
k_sn=23.9
θ=0.055 ± 0.18
k_sn=175
θ=0.99 ± 0.26
θ_ref = 0.45
gradient
drainage area (m^2)

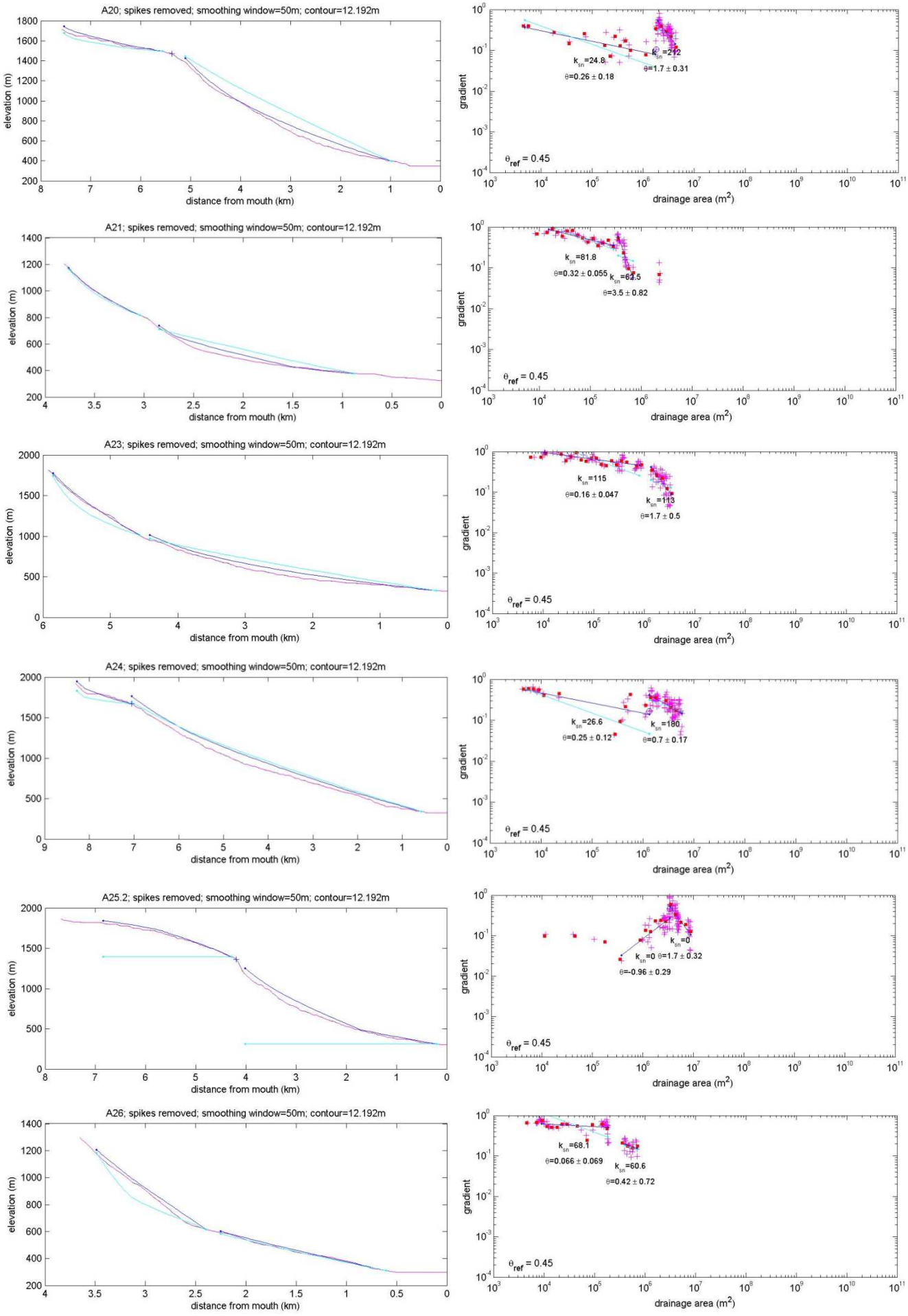
A20; spikes removed; smoothing window=50m; contour=12.192m
elevation (m)
distance from mouth (km)
gradient
drainage area (m2)
ksn=24.8
θ=0.26 ± 0.18
ksn=212
θ=1.7 ± 0.31
θref = 0.45
A21; spikes removed; smoothing window=50m; contour=12.192m
ksn=81.8
θ=0.32 ± 0.055
ksn=62.5
θ=3.5 ± 0.82
A23; spikes removed; smoothing window=50m; contour=12.192m
ksn=115
θ=0.16 ± 0.047
ksn=113
θ=1.7 ± 0.5
A24; spikes removed; smoothing window=50m; contour=12.192m
ksn=26.6
θ=0.25 ± 0.12
ksn=180
θ=0.7 ± 0.17
A25.2; spikes removed; smoothing window=50m; contour=12.192m
ksn=0
ksn=0 θ=1.7 ± 0.32
θ=-0.96 ± 0.29
A26; spikes removed; smoothing window=50m; contour=12.192m
ksn=68.1
θ=0.066 ± 0.069
ksn=60.6
θ=0.42 ± 0.72

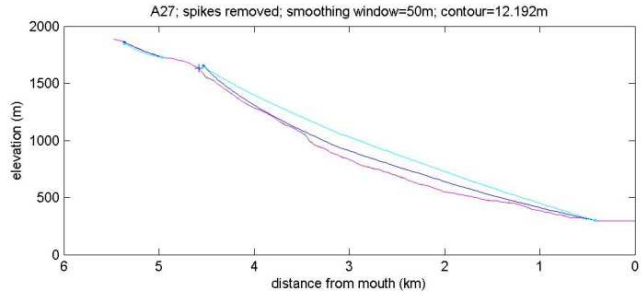
A27; spikes removed; smoothing window=50m; contour=12.192m
elevation (m)
distance from mouth (km)

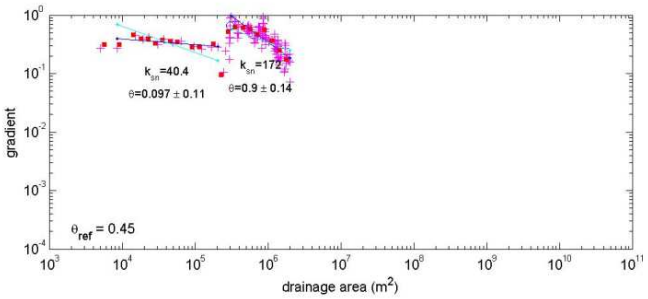
k_sn=40.4
θ=0.097 ± 0.11
k_sn=172
θ=0.9 ± 0.14
θ_ref = 0.45
gradient
drainage area (m²)

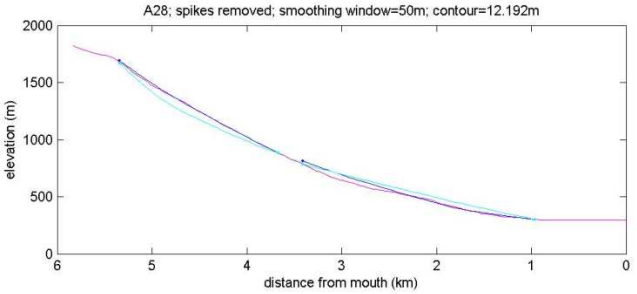
A28; spikes removed; smoothing window=50m; contour=12.192m
elevation (m)
distance from mouth (km)

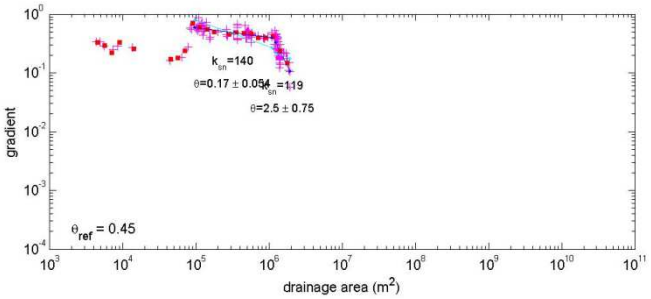
k_sn=140
θ=0.17 ± 0.054
k_sn=119
θ=2.5 ± 0.75
θ_ref = 0.45
gradient
drainage area (m²)

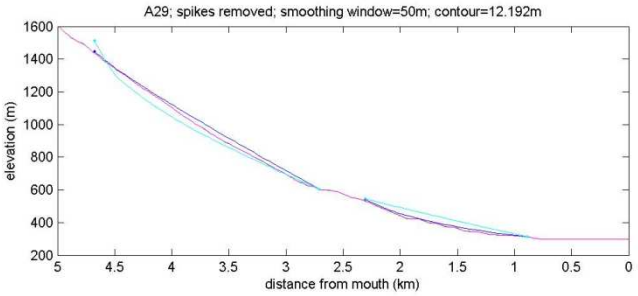
A29; spikes removed; smoothing window=50m; contour=12.192m
elevation (m)
distance from mouth (km)

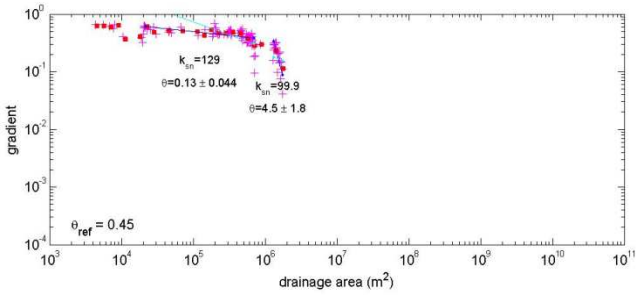
k_sn=129
θ=0.13 ± 0.044
k_sn=99.9
θ=4.5 ± 1.8
θ_ref = 0.45
gradient
drainage area (m²)

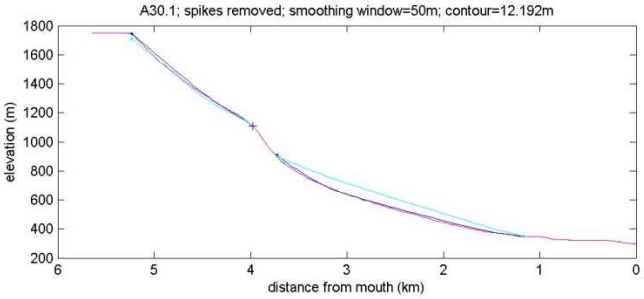
A30.1; spikes removed; smoothing window=50m; contour=12.192m
elevation (m)
distance from mouth (km)

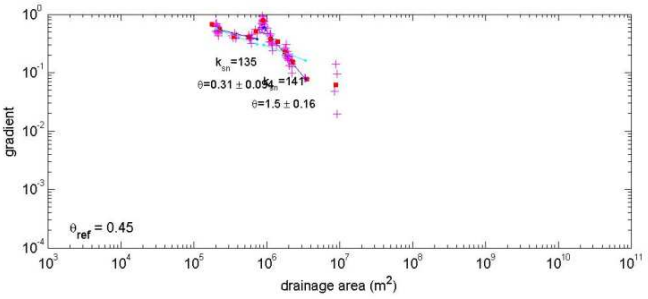
k_sn=135
θ=0.31 ± 0.054
k_sn=141
θ=1.5 ± 0.16
θ_ref = 0.45
gradient
drainage area (m²)

B-side:

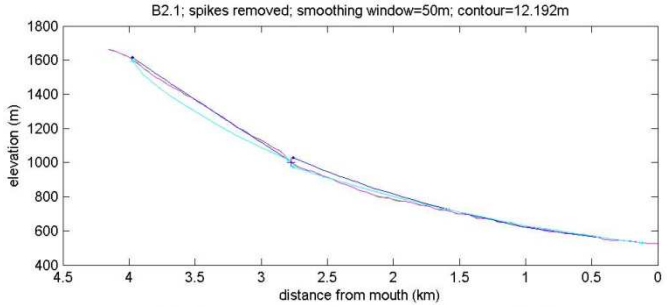
B2.1; spikes removed; smoothing window=50m; contour=12.192m
elevation (m)
distance from mouth (km)

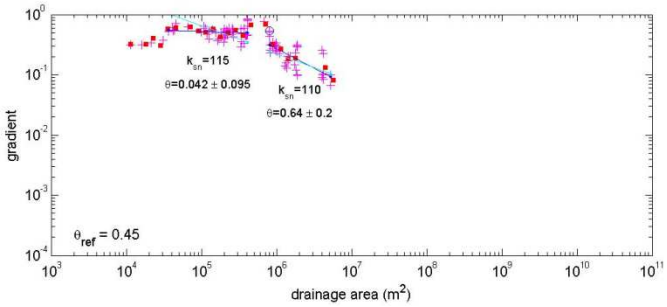
k_sn=115
θ=0.042 ± 0.095
k_sn=110
θ=0.64 ± 0.2
θ_ref = 0.45
gradient
drainage area (m²)

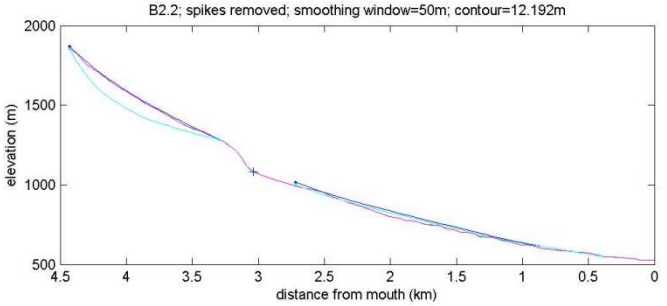
B2.2; spikes removed; smoothing window=50m; contour=12.192m
elevation (m)
distance from mouth (km)

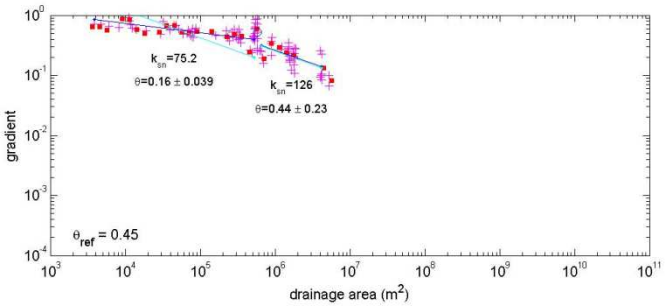
k_sn=75.2
θ=0.16 ± 0.039
k_sn=126
θ=0.44 ± 0.23
θ_ref = 0.45
gradient
drainage area (m²)

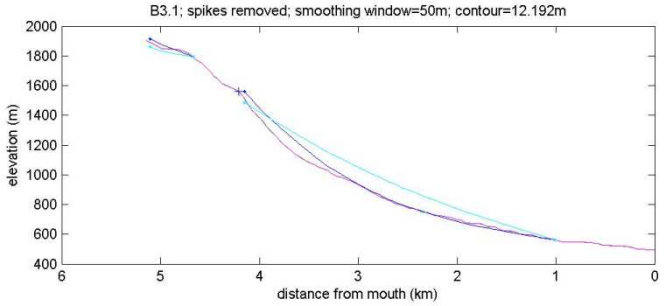
B3.1; spikes removed; smoothing window=50m; contour=12.192m
elevation (m)
distance from mouth (km)

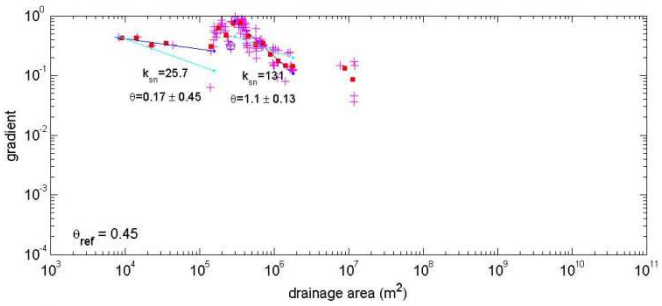
gradient
drainage area (m2)
ksn=25.7
θ=0.17 ± 0.45
ksn=131
θ=1.1 ± 0.13
θref = 0.45

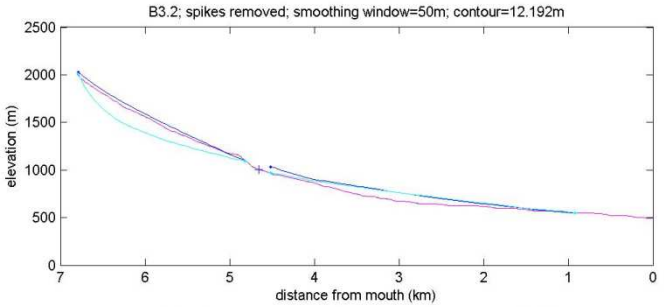
B3.2; spikes removed; smoothing window=50m; contour=12.192m
elevation (m)
distance from mouth (km)

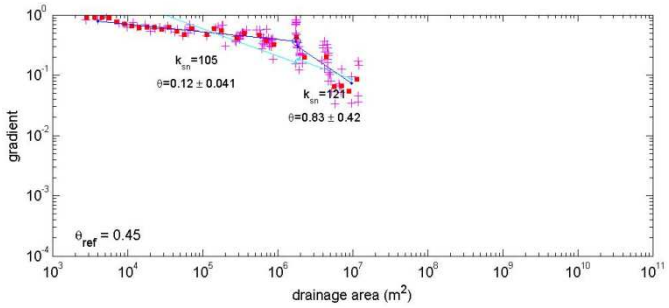
gradient
drainage area (m2)
ksn=105
θ=0.12 ± 0.041
ksn=121
θ=0.83 ± 0.42
θref = 0.45

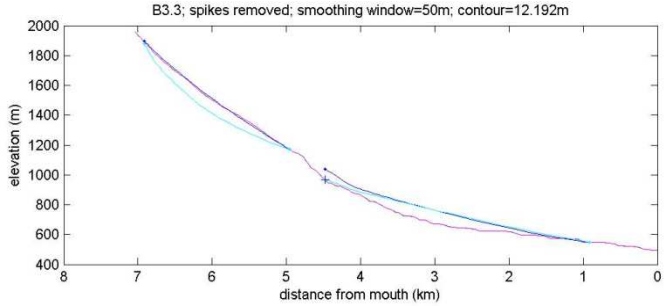
B3.3; spikes removed; smoothing window=50m; contour=12.192m
elevation (m)
distance from mouth (km)

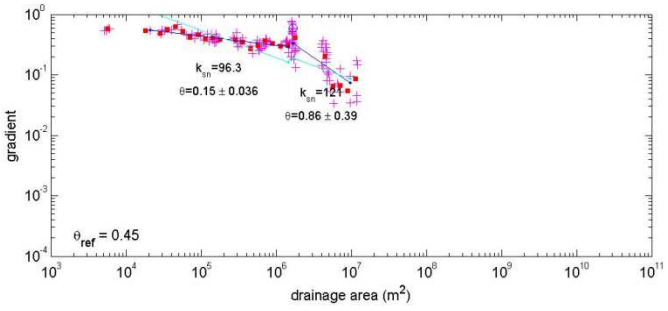
gradient
drainage area (m2)
ksn=96.3
θ=0.15 ± 0.036
ksn=121
θ=0.86 ± 0.39
θref = 0.45

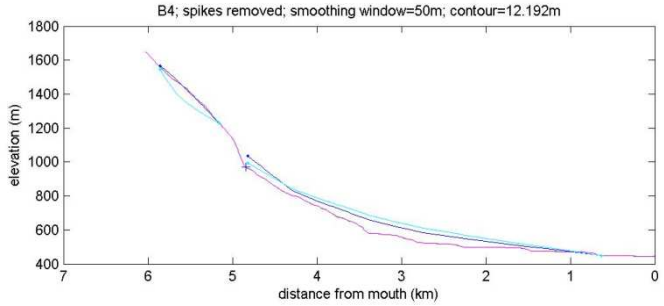
B4; spikes removed; smoothing window=50m; contour=12.192m
elevation (m)
distance from mouth (km)

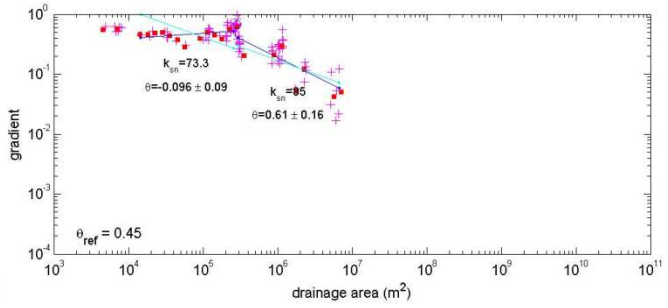
gradient
drainage area (m2)
ksn=73.3
θ=-0.096 ± 0.09
ksn=85
θ=0.61 ± 0.16
θref = 0.45

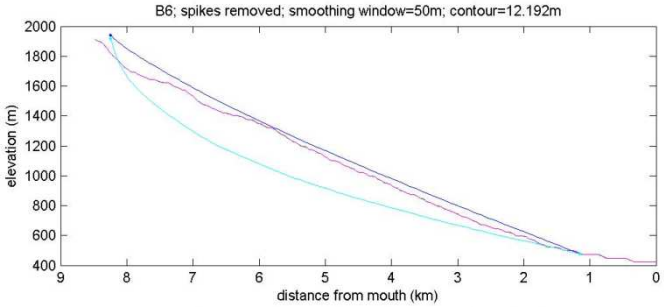
B6; spikes removed; smoothing window=50m; contour=12.192m
elevation (m)
distance from mouth (km)

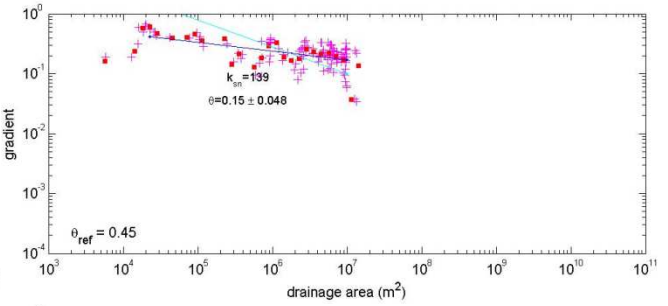
gradient
drainage area (m2)
ksn=139
θ=0.15 ± 0.048
θref = 0.45

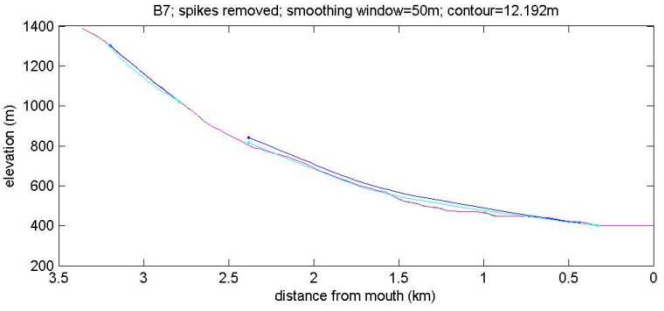
B7; spikes removed; smoothing window=50m; contour=12.192m
elevation (m)
distance from mouth (km)

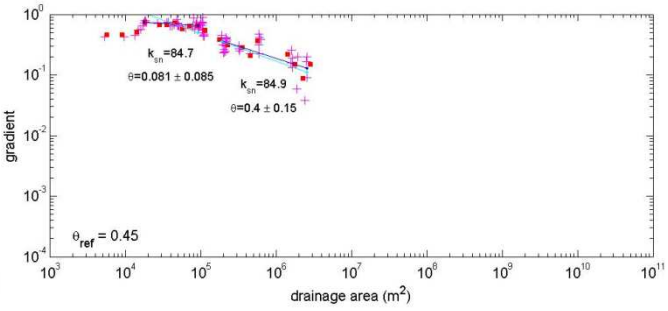
gradient
drainage area (m2)
ksn=84.7
θ=0.081 ± 0.085
ksn=84.9
θ=0.4 ± 0.15
θref = 0.45

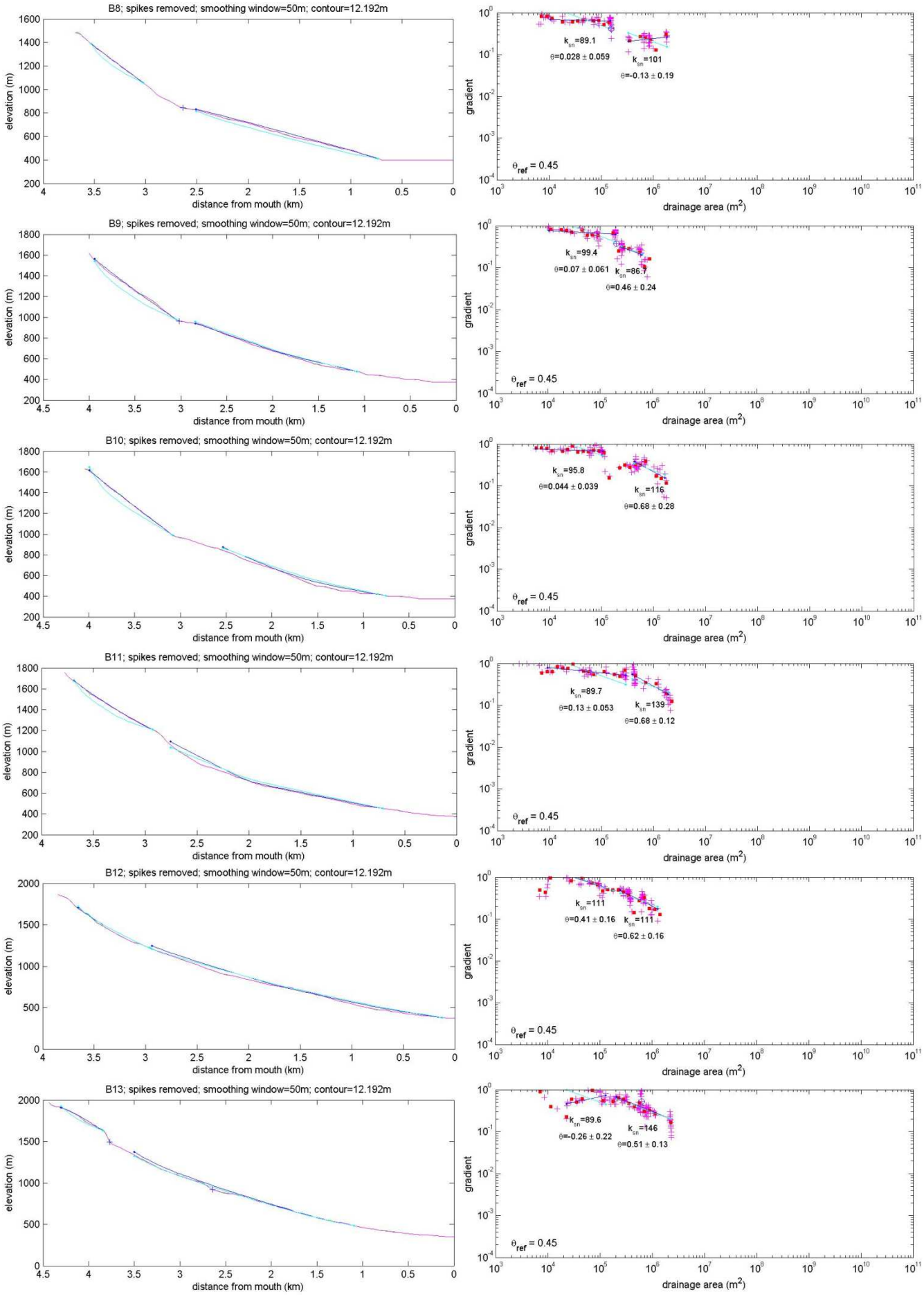
B8; spikes removed; smoothing window=50m; contour=12.192m
elevation (m)
distance from mouth (km)
gradient
drainage area (m2)
ksn=89.1
θ=0.028 ± 0.059
ksn=101
θ=-0.13 ± 0.19
θref = 0.45
B9; spikes removed; smoothing window=50m; contour=12.192m
ksn=99.4
θ=0.07 ± 0.061
ksn=86.7
θ=0.46 ± 0.24
B10; spikes removed; smoothing window=50m; contour=12.192m
ksn=95.8
θ=0.044 ± 0.039
ksn=116
θ=0.68 ± 0.28
B11; spikes removed; smoothing window=50m; contour=12.192m
ksn=89.7
θ=0.13 ± 0.053
ksn=139
θ=0.68 ± 0.12
B12; spikes removed; smoothing window=50m; contour=12.192m
ksn=111
θ=0.41 ± 0.16
ksn=111
θ=0.62 ± 0.16
B13; spikes removed; smoothing window=50m; contour=12.192m
ksn=89.6
θ=-0.26 ± 0.22
ksn=146
θ=0.51 ± 0.13

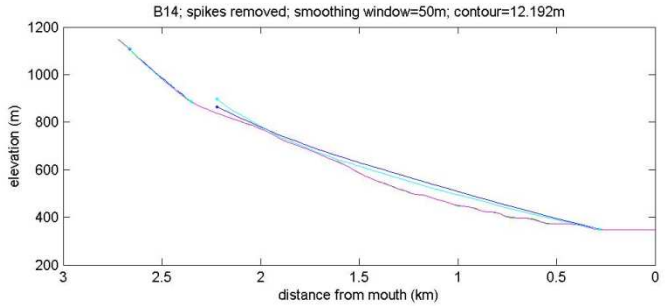
B14; spikes removed; smoothing window=50m; contour=12.192m
elevation (m)
distance from mouth (km)

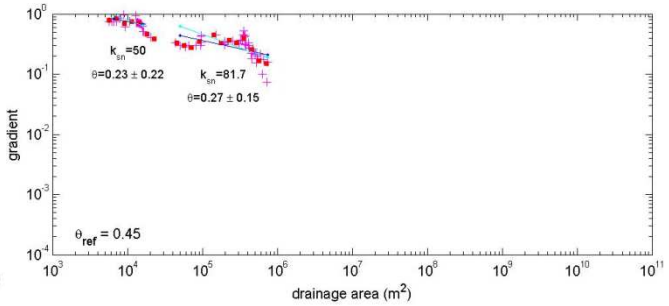
k_sn=50
θ=0.23 ± 0.22
k_sn=81.7
θ=0.27 ± 0.15
θ_ref = 0.45
gradient
drainage area (m^2)

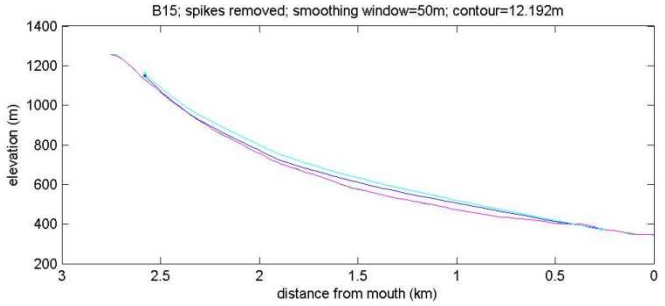
B15; spikes removed; smoothing window=50m; contour=12.192m
elevation (m)
distance from mouth (km)

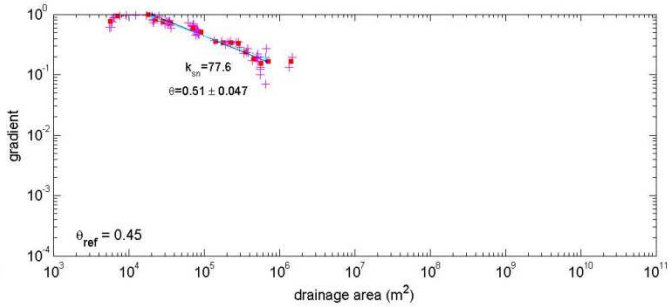
k_sn=77.6
θ=0.51 ± 0.047
θ_ref = 0.45
gradient
drainage area (m^2)

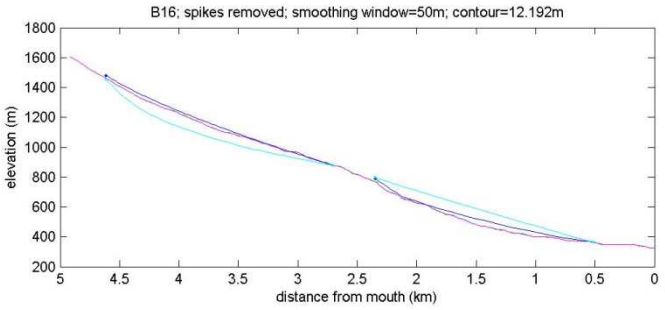
B16; spikes removed; smoothing window=50m; contour=12.192m
elevation (m)
distance from mouth (km)

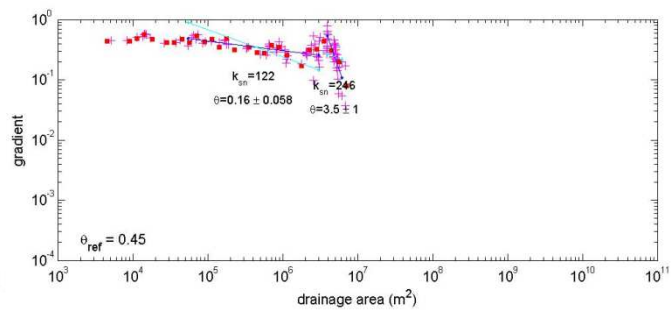
k_sn=122
θ=0.16 ± 0.058
k_sn=246
θ=3.5 ± 1
θ_ref = 0.45
gradient
drainage area (m^2)

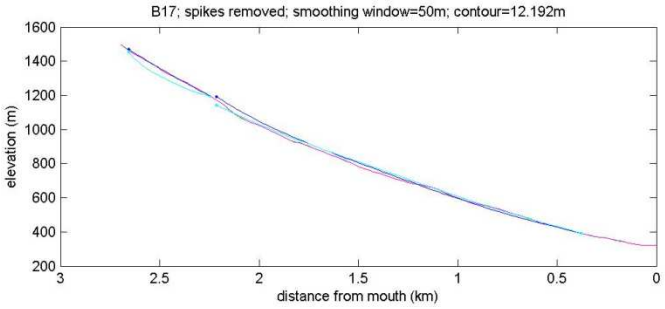
B17; spikes removed; smoothing window=50m; contour=12.192m
elevation (m)
distance from mouth (km)

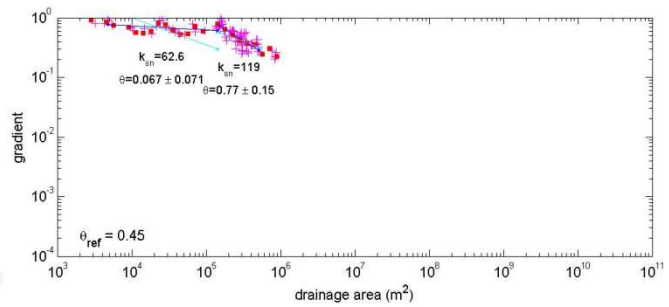
k_sn=62.6
θ=0.067 ± 0.071
k_sn=119
θ=0.77 ± 0.15
θ_ref = 0.45
gradient
drainage area (m^2)

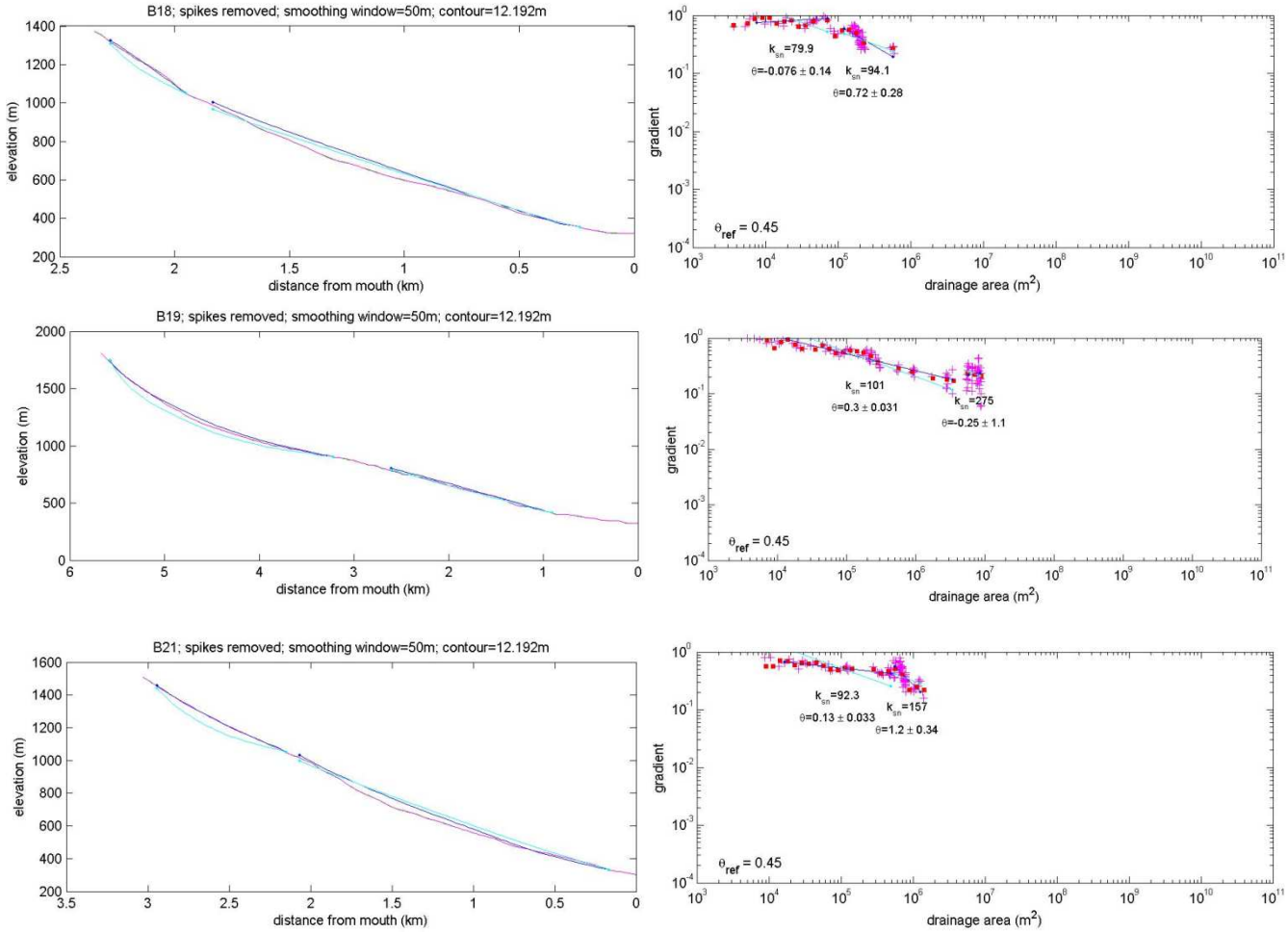

Appendix B. Streams or parts of them left out of the concavity analysis

A-side:

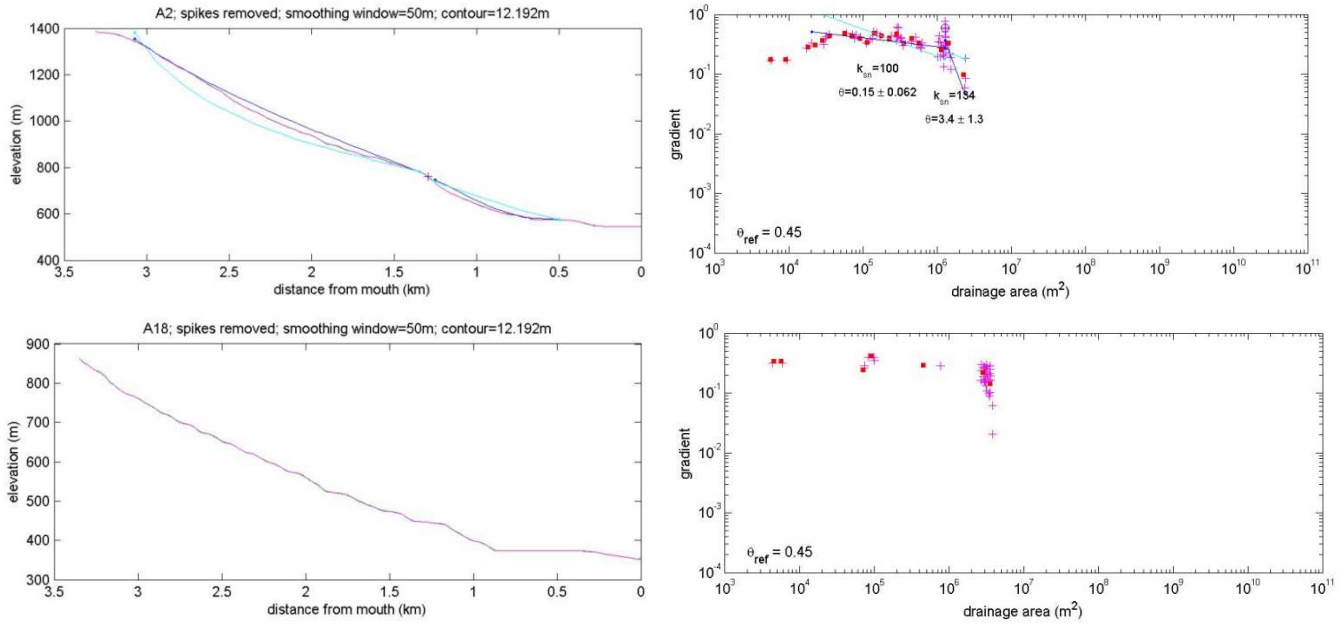

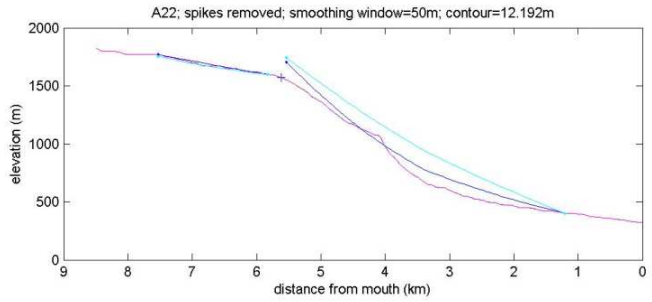
A22; spikes removed; smoothing window=50m; contour=12.192m
elevation (m)
distance from mouth (km)

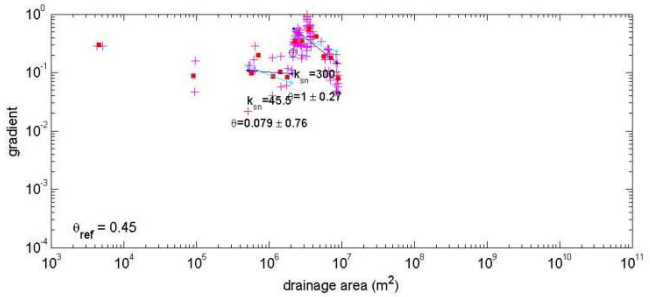
gradient
drainage area (m2)
θref = 0.45
ksn=300
ksn=45.5
θ=1 ± 0.27
θ=0.079 ± 0.76

B-side:

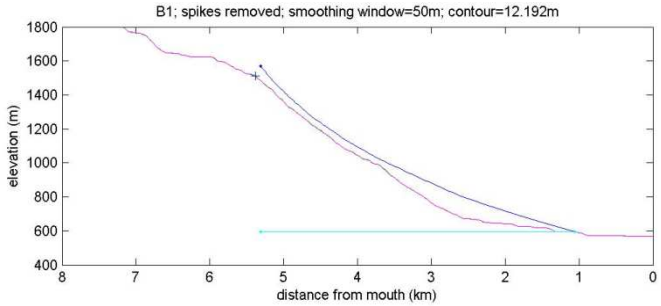
B1; spikes removed; smoothing window=50m; contour=12.192m
elevation (m)
distance from mouth (km)

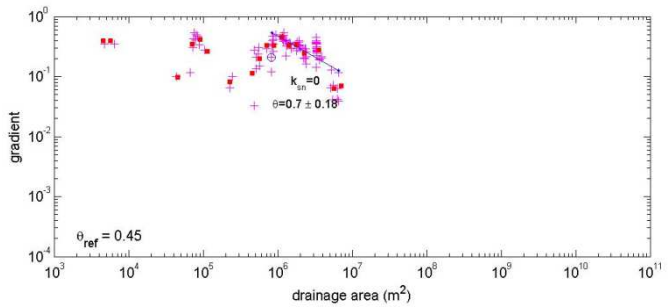
gradient
drainage area (m2)
θref = 0.45
ksn=0
θ=0.7 ± 0.18

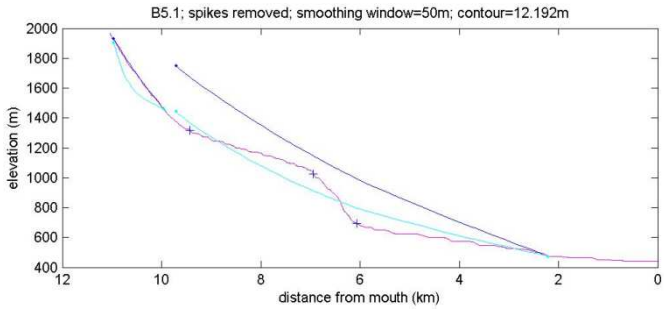
B5.1; spikes removed; smoothing window=50m; contour=12.192m
elevation (m)
distance from mouth (km)

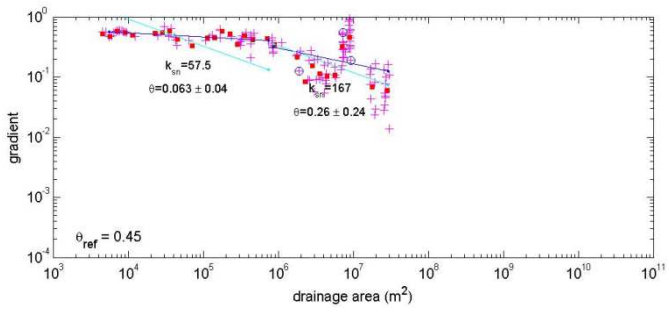
gradient
drainage area (m2)
θref = 0.45
ksn=57.5
θ=0.063 ± 0.04
ksn=167
θ=0.26 ± 0.24

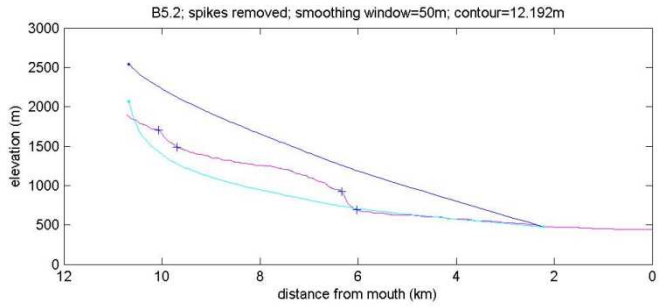
B5.2; spikes removed; smoothing window=50m; contour=12.192m
elevation (m)
distance from mouth (km)

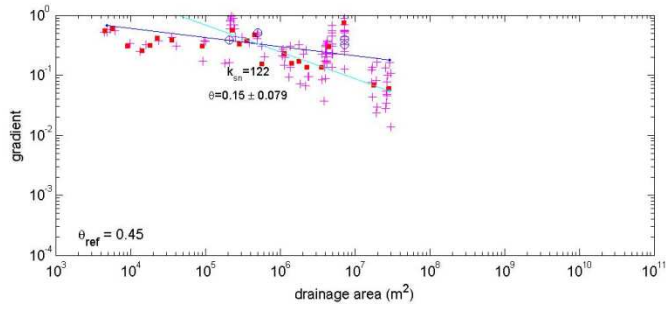
gradient
drainage area (m2)
θref = 0.45
ksn=122
θ=0.15 ± 0.079

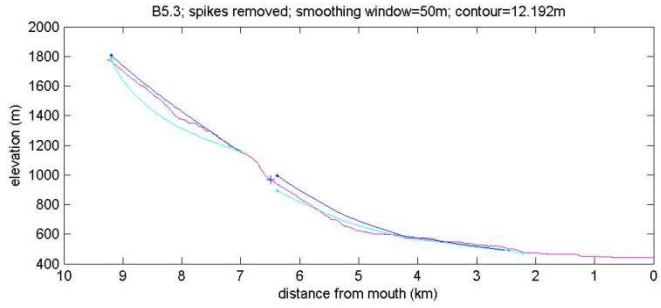
B5.3; spikes removed; smoothing window=50m; contour=12.192m
elevation (m)
distance from mouth (km)

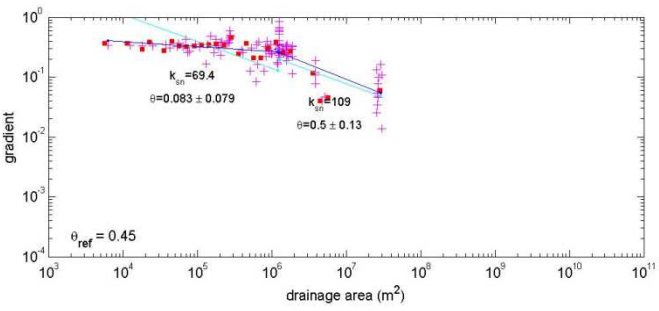
gradient
drainage area (m2)
θref = 0.45
ksn=69.4
θ=0.083 ± 0.079
ksn=109
θ=0.5 ± 0.13

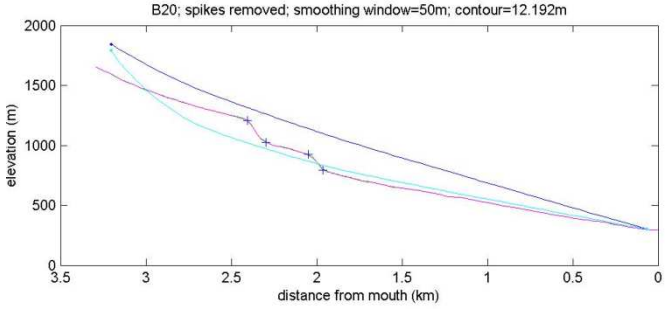
B20; spikes removed; smoothing window=50m; contour=12.192m
elevation (m)
distance from mouth (km)

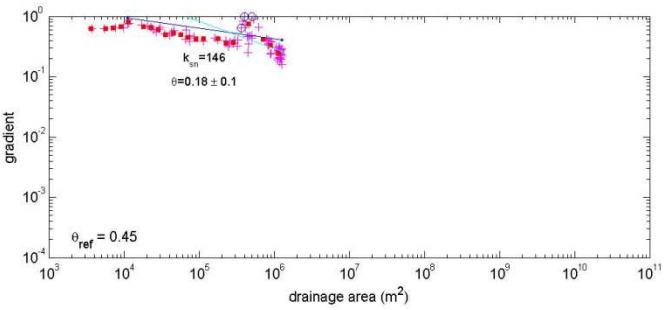
gradient
drainage area (m2)
θref = 0.45
ksn=146
θ=0.18 ± 0.1